Andreas Janz

Thermodynamics and constitution of quaternary Mg-Al-Ca-Sr alloys and the extension to the quinary Mg-Al-Ca-Sr-Mn system

Dissertation
TU Clausthal, 2008

Thermodynamics and constitution of quaternary Mg-Al-Ca-Sr alloys and the extension to the quinary Mg-Al-Ca-Sr-Mn system

Doctoral Thesis
(Dissertation)
to be awarded the degree of
Doctor of Engineering (Dr.-Ing)

submitted by
Dipl.-Ing. Andreas Janz
from Clausthal-Zellerfeld

approved by the
Faculty of Natural and Materials Science,
Clausthal University of Technology

Date of oral examination
28 March 2008

Chairperson of the Board of Examiners
Prof. Dr. rer. nat. habil. Wolfgang Schade

Chief Reviewer
Prof. Dr.-Ing. habil. Rainer Schmid-Fetzer

Reviewer
Prof. Dr.-Ing. habil. Karl Ulrich Kainer

This work has been conducted at the Institute of Metallurgy of the Clausthal University of Technology.

'Winnie-the-Pooh wasn't quite sure,' said Christopher Robin.
'Now I am,' said a growly voice.
'Then I will go on,' said I.

A. A. Milne

Contents

Chapter 1

Introduction

Magnesium is one of the lightest construction metals. It outperforms the classic metals for lightweight constructions, aluminum and titanium, with its low density of 1.7 g/cm^3. A short comparison of these metals is given in Table 1.1 . In the earth's crust Mg participates at about 2 wt.% being no. 8 in the list of the most common elements. Like all alkaline earth metals Magnesium is very reactive and thus can only be found in compounds. The major resources are Mg-salts (solute in seawater or bulk in salt cavities), Mg-silicates (e.g. olivine, asbestos) and Mg-carbonates (magnesite, dolomite).

Table 1.1: Selected elements' appearance and properties. Sources: [1992Ger, 1995Pre]

Element	Mg	Al	Ti	Fe
occurence in the earth crust [wt.%]	2.1	8.1	0.4	4.7
ranking position	8	3	9	4
atomic number	12	13	22	26
density [g/cm^3]	1.74	2.70	4.51	7.87

Today's common processing routes to produce primary Magnesium are the Pidgeon process[1] and the fusion electrolysis invented at Dow Chemical (Midland, MI, USA). The latter is often installed as a seawater extracted magnesium chloride electrolysis and was the dominating production route up to the mid 1990s, mainly being implemented in the USA. China has now become the world's major supplier for Magnesium using almost exclusively the thermal reduction route with the Pidgeon process. This is separated into two batch processes: (if necessary) the silicothermic reduction to produce $MgCO_3$ from MgO, followed by a distillation/vapor-deposition in stainless steel retorts.
According to the statistics of the International Magnesium Association [IMA], the China Magnesium Association reported an annual production of 526,000 tons in 2006 which is

---

[1] named after the inventor, Dr. Lloyd Montgomery Pidgeon of the Canadian National Research Council (NRC)

nearly $\frac{3}{4}$ of the world's annual production of 726,000 tons. Going back ten years to 1996 the USA and Canada produced $\frac{3}{4}$ of the 248,300 tons in that year.
The production of Magnesium in the world has been growing at an average rate of 7% annually since 2000. This growth is focused on China (and marginally on Israel) while elsewhere e.g. in the USA, France and Norway plants have been closed down.

The first applications of Mg alloy components go back to the 1930s-1940s (Volkswagen (Wolfsburg, Germany) producing parts for automotive applications and generally during World War II magnesium was used for aircraft components). While the use at Volkswagen reached a peak in the 1970s for the *Beetle*, Mg had since been forgotten as a structural material. Meanwhile the common use was for desoxidation and alloying applications in e.g. the steel and aluminum industry. With the trend of fuel saving and lightweight construction, the use of Mg alloys has increased drastically during the last years and new specialized alloys are frequently developed.
Typical Mg-alloy parts processed by die-casting are for lightweight cases, e.g. for cell phones, mobile computers etc.. Also in all other situations where a low weight is beneficial, Mg alloys are utilized. Especially for the transportation sector, parts have been developed for housings, rims, seats, steering wheels and dashboards in order to reduce the weight and therewith the fuel demand.

Magnesium has to face, again and again, two common prejudices: it *burns* and it *corrodes*.
Many investigations have shown these generalizations to be false - of course it is not wise to extinguish burning magnesium with water as it is the same with aluminum. If treated with the proper equipment, the risk of burning Mg is small. Also the corrosion properties of today's Mg-alloys are quite satisfying, especially in seawater due to the high concentration of solute Mg-Salts there. A passive layer of $Mg(OH)_2$ is generally formed on the surface during contact with the atmosphere or other media and is mostly only destroyed by acids.

Commercial Mg alloys are divided into two main groups: wrought & cast alloys, depending on the processing route for which they are designed. Furthermore the alloys are classified based on their major alloying elements since as for nearly all materials, the properties of Mg are adjusted by the alloying of other elements. To each element a specific character has been assigned by the American Society for Testing and Materials (ASTM)(see Table 1.2). Typical alloy groups are AZ, AM, AX, AJ, AE, QE, WE, ZE, ZK, ... Together with the numbers representing the nominal amount in wt.% for the given elements, this description enables the quick allocation of the rough chemical composition of a specific alloy. For example an AZ31-Mg-alloy contains beside the major element Mg about 3 wt.% Al and 1 wt.% Zn.

The commercial use of magnesium alloys is currently focused on the Mg-Al based ones, especially on the AZ and AM series. These alloys combine good room-temperature

Table 1.2: Selected alloying elements

Alloying element	Al	Zn	Mn	Ca	Sr	Si	Cer-MM	Zr	Y	Ag
ASTM-Code	A	Z	M	X	J	S	E	K	W	Q

strength and ductility with satisfying salt-spray corrosion resistance and excellent castability. Special automotive applications, such as powertrain components or engine blocks, require sufficient creep resistance at elevated temperatures. For these elevated temperature applications new alloys have been developed using additions of rare earth (RE) elements or Ca and Sr. The potential of these alloys was discussed by Luo [2004Luo]. He demonstrated promising results on the high temperature strength for Mg-based alloys with Sr and Ca, but emphasized the need for careful process controlling to avoid castability problems like sticking and cracking.
A recent example for the application of Mg-Al-(Mn)-Ca/-Sr based alloys is the use of AJ62 (the alloy was developed and applied in the same time frame as the work for this thesis) for the 3.0 L straight 6 cyl. engine block build by BMW (Munich, Germany). They applied a composite magnesium/aluminum crankcase as shown in Fig. 1.1 . The bond between the alloys AJ62 and A390 is clearly visible in the magnified top left inset.

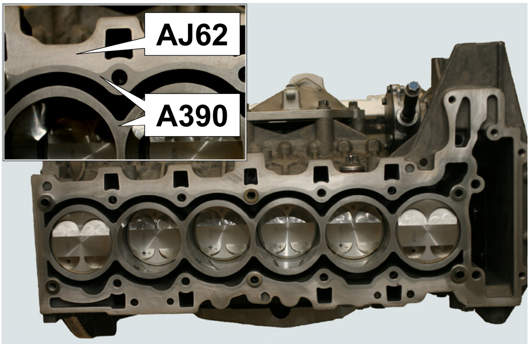

Fig. 1.1: Composite AJ62+A390 engine block developed by BMW.

Additions of RE elements show similar advantages, but should be minimized considering their high cost. In spite of this these alloys are used e.g. for the engine cradle of the Chevrolet C6 Z06 Corvette (General Motors, Detroit, MI, USA) presented in late 2005. This application of AE44 alloy was promoted as the world's first magnesium chassis component and provides a 35% weight saving versus the original aluminum design.

The development of alloys has been predominantly based on empirical methods. Within this environment, phase diagrams (normally binary ones) play an important role, since they "'*[...] are visual representations of the state of a material as a function of temperature, pressure and concentrations of the constituent components [...]*' [1997Kat].

The limited information from the binary phase diagrams on phases and solubilities is used as blueprints or roadmaps for the design and development of new alloys as well as for their processing. Certain component-equivalents have been established to reduce the complexity for the estimation of phase equilibria and their demonstration in 2D-diagrams.

Using appropriate software packages and thoroughly developed multicomponent databases for the calculation of phase diagrams enables in contrast purposive results for specific demands. The term *computational thermodynamics* replaces increasingly *calculation of phase diagrams* which was the origin for the CALPHAD approach detailed later. This reflects the fact that the information, which can be gained from these calculations, goes far beyond the classical *phase diagram*. Phase diagrams (here quantitative multi-component ones) are still important since they are principally known by the target audience. Calculating the solidification of specific alloys under different cooling conditions will give information which is much more precise and relevant for the application of these alloys. Generating data for a series of compositions will help to identify trends which can be then used for an even more focused development.

The work presented in this thesis will give an example for a scientific approach of a systematic and focused alloy development, combining experimental work and computational thermodynamics.

The purpose of this work was to develop a consistent thermodynamic description for the Mg-Al-Ca-Sr-Mn system which is the backbone for understanding the phase equilibria and solidification in the commercial AM, AX, AJ and AXJ alloy groups. The emphasis is on the of the phase equilibria of the quaternary Mg-Al-Ca-Sr system which is then extended to the quinary Mg-Al-Ca-Sr-Mn system.

It was necessary to

- generate reliable thermodynamic descriptions for the pertinent ternary subsystems
- validate the results of multicomponent calculations through selected key experiments
- develop a quantitative criterion for the selection of the most important experimental conditions

During the thorough investigation of the ternary phase equilibria, particular attention was paid to ternary solubilities of binary solid phases, and true ternary compounds were identified.

The validation of multicomponent calculations was performed with key experiments identified by a newly developed algorithm for both the Mg-Al-Ca-Sr system and later the Mg-Al-Ca-Sr-Mn system.

This study was realized using the following tools in combination:

- Calphad Assessment
- Computational Thermodynamics
- Differential Scanning Calorimetry and Differential Thermal Analysis
- Scanning Electron Microscopy and Electron Probe X-Ray Microanalysis

This work was supported within the framework of the Priority Programme SPP1168 *Extending the Range of Applications of Magnesium Alloys 'InnoMagTec'* of the German Research Foundation (DFG).

Chapter 2

Methodology

This chapter is intended to demonstrate the methodology behind this thesis' work. An approach has been selected combining thermodynamic calculations with own experimental work as well as data from the literature.
It will be shown that the *iterative* combination of these tools is the most goal-oriented procedure available.
A brief introduction into the different tools used will be given in the following sections - special topics will also be discussed.

2.1 The Calphad approach

CALPHAD is the acronym for **CAL**culation of **PHA**se **D**iagrams. The Calphad approach (or Calphad method) follows the aim to describe the thermodynamic properties of each phase consistently with the adjustable parameters of a mathematical model of the Gibbs energy of each phase.

A collection of the mathematical models with their optimized parameters for each possible phase forms the data set for a particular alloy system.

The fundamental correlation between thermodynamics and phase equilibria was established by J. W. Gibbs in the 19^{th} century: That phase ϕ (or combination thereof), which has the lowest integral Gibbs energy G^{ϕ} at given temperature, pressure and composition is the stable one.

All available thermochemical, thermophysical and thermodynamic information is critically assessed at the beginning of the optimization process for a dataset to identify inconsistencies and to see where information is missing. The model parameters are then fitted to these properties to give a reliable representation of the known data.

The beauty of the Calphad method is the consistency of the thermodynamic description. Since it is only based on the fundamental set of equations for the Gibbs energy of each phase, this method is self-consistent. All multicomponent multiphase equilibria with all the thermochemical properties like e.g. enthalpies of formation or mixing are derived from only one single dataset.

With this single dataset not only equilibrium calculations within the assessed range but also extrapolations to regions without experimental data are then possible as well as the calculation of metastable states and e.g. non-equilibrium solidification under Scheil conditions [1942Sch].

The increasing amount of available computing power has speeded up the use of this method developed in the 1960's allowing calculations in multicomponent multiphase systems. Standard commercial software products are FactSage[1], MT-Data[2], PANDAT[3] and Thermo-Calc[4].

Fig. 2.1 shows the flow sheet of the modelling process as summarized by Lukas et al. in [2007Luk]. Thermodynamic Databases are always based on the description of the unary compounds. A multicomponent database will be constructed by consecutive additions of first the excess Gibbs energy terms for binary interactions ${}^{E}G^{bin}$ for solutions phases as well as Gibbs energy models for new binary phases which have to be gained from a thorough assessment. Subsequently ternary excess interactions ${}^{E}G^{ter}$ and ternary phases

---

[1] www.factsage.com

[2] www.npl.co.uk/mtdata

[3] www.computherm.com

[4] www.thermocalc.com

are added and so on for quaternary and quinary systems. During the assessment key experiments can be selected and performed to produce the necessary information.
Kattner states in [1997Kat] that true new phases appear in metallic systems with four or more components very rarely. Therefore the *'assessment of most of the ternary constituent systems is often sufficient to describe a n-component system'*.

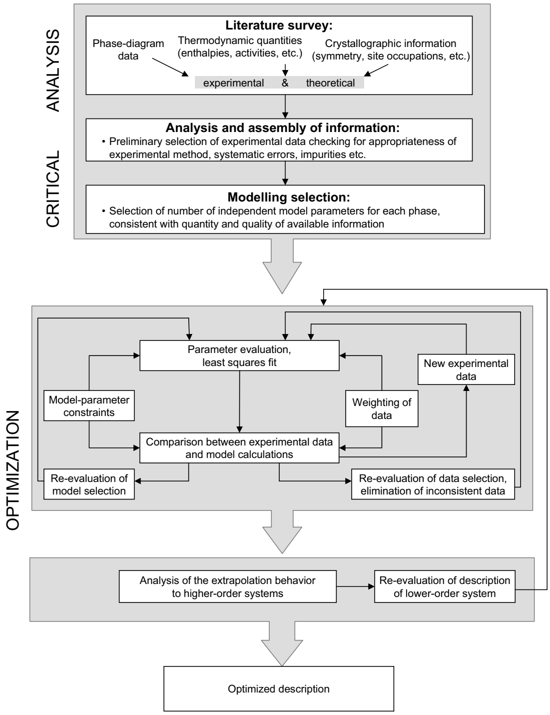

Fig. 2.1: The CALPHAD methodology. [2007Luk]

For a comprehensive presentation of this issue the recent book of Lukas et. al. 'Computational Thermodynamics: The Calphad Method' [2007Luk] is recommended. Furthermore the paper Kattner published in 1997 deals with the special requirements for multicomponent multiphase calculations [1997Kat]. And the most recent 'Ringberg'-report [2007Sch] on assessment techniques and database design might be very helpful for an access to the Calphad method.

The software package Pandat [2001Che, 2002Che] has been used for all thermodynamic calculations in this work.

2.2 Thermodynamic models

As stated in the previous section, the Gibbs energy of each phase is described by the parameters of a mathematical model.

The basic principle to find the equilibrium state of a multicomponent alloy (or system) is to minimize its total Gibbs energy, G, at constant temperature T, pressure P, and overall composition:

$$G = \sum_{\phi} n^{\phi} G^{\phi} = min \tag{2.1}$$

where G^{ϕ} is the molar Gibbs energy of any possible phase ϕ in the system and n^{ϕ} is its amount in mol of atoms. Minimization is done by distributing the given amount of alloy components onto the various available phases, subject to the overall material balance. The stable equilibrium is described by a phase assembly of all phases with $n^{\phi} > 0$, whereas the metastable phases ($n^{\phi} = 0$) do not materialize. Each phase has its own composition, which is generally different from the fixed overall alloy composition. We have thus to supply the functions G^{ϕ} for all the phases.

A wide range of mathematical models for the G^{ϕ} function has been developed as one global model for all types of phases would result in an unnecessary complexity. Those models used to describe the phases within this work are described in the following.

Unary description

The Gibbs energy function for the element i in the phase ϕ, G^{ϕ}, is referred to the SER standard state by the equation

$$G_i^{0,\phi}(T) = G_i^{\phi}(T) - H_i^{SER} \tag{2.2}$$

where H_i^{SER} is the molar enthalpy of the stable element reference (SER) at 298.15 K and 1 bar, and T is the absolute temperature.
It is empirically described by the polynomial equation:

$$G_i^{0,\phi}(T) = a + b \cdot T + c \cdot T \cdot \ln T + d \cdot T^2 + e \cdot T^3 + f \cdot T^{-1} + g \cdot T^7 + h \cdot T^{-9} \tag{2.3}$$

All unary Gibbs energy functions used in this work are taken from the SGTE compilation by Dinsdale [1991Din].

Solution phases Redlich-Kister/Muggianu (Liquid phase, hcp, fcc, bcc, ...)

For a multicomponent solution phase ϕ with c components the following equation is used to describe the molar Gibbs energy:

$$G^{\phi} = \sum_{i=1}^{c} x_i G_i^{0,\phi} + RT \sum_{i=1}^{c} x_i \ln x_i + {}^{E}G^{bin,\phi} + {}^{E}G^{tern,\phi} + ... \tag{2.4}$$

in which R is the gas constant, T the absolutetemperature in K and x_i are the molar fractions of the components i. All excess contributions originating from all the binary interactions (${}^{E}G^{bin}$) or ternary interactions (${}^{E}G^{tern}$) are:

$$ {}^{E}G^{bin,\phi} = \sum_{i=1}^{c-1} \sum_{j>i}^{c} x_i x_j \sum_{v=0}^{n} L_{ij}^{v,\phi} (x_i - x_j)^v \tag{2.5} $$

$$ {}^{E}G^{tern,\phi} = \sum_{i=1}^{c-2} \sum_{j>i}^{c-1} \sum_{k>j}^{c} x_i x_j x_k \{ L_{ijk}^{1,\phi}(x_i + \delta_{ijk}) + L_{ijk}^{2,\phi}(x_j + \delta_{ijk}) + L_{ijk}^{3,\phi}(x_k + \delta_{ijk}) \} \tag{2.6} $$

where

$$ \delta_{ijk} = (1 - x_i - x_j - x_k)/3 \tag{2.7} $$

It is noted that in a ternary system (c=3) $\delta_{ijk} = 0$. In a quaternary or higher order system (c $>$ 3) the same term $\delta_{ijk} \neq 0$. The binary interaction parameter $L_{ij}^{v,\phi}$ and the ternary interaction parameters $L_{ijk}^{v,\phi}$ may be linearly temperature dependent and are optimized using all experimental data concerning the ϕ phase and its relation with other phases.

Stoichiometric compounds

Multicomponent phases modeled as stoichiometric compounds can be referred to the stable elements, either at 298.15 K or, alternatively, at T. The latter is resulting in a floating reference.

The formalism is presented for the example of the τ-Phase $Al_{38}Mg_{58}Sr_4$:

$$ G^{\tau} = 38\, G_{Al}^{0,fcc}(T) + 58\, G_{Mg}^{0,hcp}(T) + 4\, G_{Sr}^{0,fcc}(T) + A^{\tau} + B^{\tau} \cdot T \tag{2.8} $$

where the $G_i^{0,\phi}(T)$ correlate to the unary functions and the parameters A^{τ} and $-B^{\tau}$ correspond to the enthalpy and entropy of formation.

An alternative is to use the absolute reference at 298K and a full c_p description. Details for this model can be found in [2007Koz].

Compound energy formalism (CEF)

The compound energy formalism was used in this work to describe line compound phases in the binary (e.g. γ-$Mg_{17}Al_{12}$) and ternary (e.g. Al4Sr, Mg2Ca) as well as solution phases in the ternary (C36, γ-$Mg_{17}Al_{12}$). The CEF provides the possibility of describing solubilities by distributing the elements on different sublattices introduced for the phase. A special case arises if we have only one constituent on a sublattice, as used for the second sublattice of the $(Al,Mg)_mSr_n$-phases.

The Gibbs energy of these phases $(Al,Mg)_mSr_n$ (per mole of formula unit) is expressed in the Compound-Energy Formalism [1970Hil] by

$$ \begin{aligned} G^{\phi} = {} & y_{Al} G_{Al:Sr}^{0,\phi} + y_{Mg} G_{Mg:Sr}^{0,\phi} \\ & + m \cdot R \cdot T (y_{Al} \cdot \ln y_{Al} + y_{Mg} \cdot \ln y_{Mg}) + y_{Al} \cdot y_{Mg} \cdot (L_{Al,Mg:Sr}^{0,\phi}) \end{aligned} \tag{2.9} $$

in which y_{Al} and y_{Mg} are the site fractions of Al and Mg on the first sublattice. The parameter $L^{0,\phi}_{Al,Mg:Sr}$ describes ternary interactions essentially within a sublattice. The parameters $G^{0,\phi}_{i:Sr}$, $i =$ Al or Mg, are also called compound energies and describe interactions essentially between the sublattices. The parameters $G^{0,\phi}_{Al:Sr}$ and $G^{0,\phi}_{Mg:Sr}$ represent the metastable end members of the solid solutions in the binary Al-Sr and Mg-Sr system.

Examples for CEF - modeled phases with three sublattices are discussed in the individual sections for the ternary subsystems, e.g. in subsection 3.2.3 starting on page 39.

2.3 Thermal analysis and scanning calorimetry

The two key experimental methods for obtaining phase transition and thermodynamic information are differential thermal analysis (DTA) and differential scanning calorimetry (DSC). These methods are widely established, but the successful usage still demands a thorough knowledge of the theoretical bases, a precise calibration of the equipment and the correct analysis of the calibration curve as prerequisites for reliable measurement results. Both systems use a differential setup, meaning that the difference in heat flow (DSC) or temperature (DTA) is measured between two containers in the same apparatus running through the same experimental program. One container hosts the sample while the other one is filled with the *reference*, usually a piece of sapphire or alumina. Ideally this reference should have a similar thermal behavior compared to the sample, but shows no transformation or reactions in the investigated temperature range. The investigation of Mg alloys at higher temperatures always brings with it the problem of evaporating alloy material. Experiments in the past have shown that the use of ceramic or carbon containers even in combination with an attached lid does often result in a contamination of the equipment. Since this was not acceptable, arc welded Ta capsules have been developed over the past years. These capsules are tested to be pressure tight and allow multiple (consecutive) runs of the same sample and at different scanning rates [2006Mir]. Tantalum has been tested to be quite inert against reactions with the alloy material. Only high Al contents have caused severe reactions with the capsules resulting in a lethal damage. For these samples, inlays machined out of sintered boron-nitride (BN) rods can be used for investigation in DSC. Due to the shape of the DTA capsules BN inlays are not practical. BN-coatings on the inner surface of the capsules were tested and have failed. Probably due to the high temperature during welding of the cap pyrolysis of the boron-nitride occurred. The layout of the different capsules available is illustrated in Fig. 2.2 .

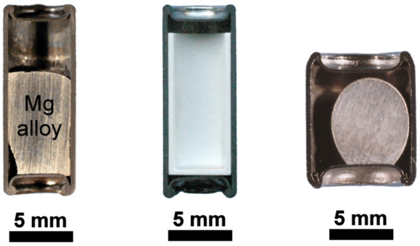

(a) DSC (b) DSC with BN inlay (c) DTA

Fig. 2.2: Different types of Ta-capsules for differential scanning calorimetry (DSC) and differential thermal analysis (DTA) used in this work.

The following is intended to just give a very brief overview on these two equipments. For continuative and detailed information the books from Höhne [1996Hoe] and Boettinger [2006Boe] are highly recommended.

2.3.1 Differential thermal analysis (DTA)

In the DTA only two thermocouples are used to measure the signals: One for each container hosting the sample and the reference. The tip of these thermocouples is in direct contact with the bottom of each Ta capsule.

The thermocouples are connected antipodal so the temperature difference can be measured directly. Based on the shape of the measured curve, information on the reaction temperature, the reaction enthalpy (only qualitative or semi-quantitative) and the reaction characteristics is gained.

A simplified view of the setup is presented in Fig. 2.3 .

A Netzsch DTA 404 (Netzsch-Gerätebau GmbH, Selb, Germany) has been used for DTA experiments in this work.

To minimize the lateral heat flow, the experimental chamber has been evacuated during all measurements.

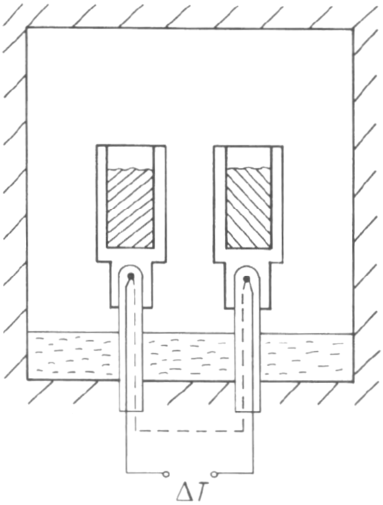

Fig. 2.3: Schematic setup of containers and thermocouples in the DTA [1989Hem].

2.3.2 Differential scanning calorimetry (DSC)

The DSC method has been developed based on the DTA method. In the DSC the exothermic and endothermic heat flows between the furnace and the sample / reference are measured. Plotting the difference in heat flow vs. the temperature gives an area under that curve which is directly proportional to the heat of the reaction which is also the measured signal.

The DSC used in this work was a ‘heat flow DSC’ Setaram MHTC 96 (Calvet-type, Setaram, Caluire, France).

In contrast to the setup of the DTA, a group of thermocouples is arranged in the sample holder around the containers which are arranged symmetrically within one furnace chamber. A simplified view of the setup is presented in Fig. 2.4 .

Since the thermal conduction shall be detected by the surrounding thermocouples, the experimental chamber is filled with Argon. In general DSC is a more quantitative method to measure enthalpies and the correlated temperatures compared to DTA.

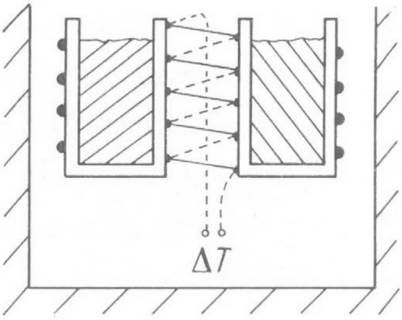

Fig. 2.4: Schematic setup of containers and thermocouples in the DSC [1989Hem].

2.4 Microstructural analysis

The microstructure of all samples has been analyzed after their thermal treatment (cooling or equilibration) using Scanning Electron Microscopy (SEM) with backscattered electrons (BSE). If substantial information about solubilities or a very fine microstructure was expected, the samples were investigated with electron probe microanalysis (EPMA) using a CAMECA SX100 (Cameca, France). All other samples were analyzed with a Scanning Electron Microscope (SEM) with Energy dispersive X-ray spectroscopy (EDX) using a CamScan 44 (CamScan, United Kingdom).

Imaging with BSE gives an image where the contrast is based on the atomic mass difference of the different phases. This can also lead to images with insufficient contrast between phases with similar chemical composition. Sometimes these phases can be rather distinguished using light optical microscopy (LOM).

For the chemical analysis with Energy (EDX) or Wavelength (WDX) dispersive X-ray spectroscopy sample material has to be activated by an electron beam, causing X-rays to be emitted. The beam not only activates the surface layer but also intrudes into deeper areas as shown in Fig. 2.5 , unless a thin-film sample is used. Unfortunately this can lead to a shift in the measured chemical composition if a mixture of different phases is evaporated and analyzed. This incident is independent from the type of analysis, EDX or WDX.
EPMA often enables a higher resolution of both the imaging and the chemical analysis. This is realized via a higher focused beam and often a more precise adjustment of the sample manipulator.

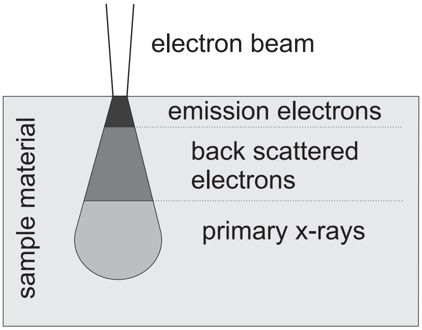

Fig. 2.5: Interaction of the beam with the sample.

2.5 Sample preparation

In principle two groups of experiments have been carried out for this work:

a) Samples for DTA or DSC to study the temperatures of phase transformations and especially invariant reactions

b) Samples equilibrated at specific temperatures to investigate ternary solubilities of binary phases and isothermal phase equilibria.

Both types have been prepared with the same procedures.
Certain specialties regarding the sample preparation will be given in each section in chapter 3 when discussing the specific alloy systems.

The samples investigated in this work have been either prepared from commercial alloy material, which has been machined into pieces that fitted the needed dimensions for the aimed investigation, or sample compositions have been selected based on the calculation with the preliminary dataset (e.g. as stated in section 2.6 or to fit on specific calculated phase diagram sections). These samples were prepared from predominantly high purity elemental materials (>99.9 wt.%, designation related to the metal basis). If necessary due to the oxidation behavior, these metals were stored and prepared under Ar-atmosphere within a glove box. Once weighed out, the materials were pressed carefully to a cylindrical pellet using a hydraulic press and a standard stainless compression mold with 5 mm inner diameter for DSC experiments (6mm for DTA). These pellets were then sealed in Ta-capsules by careful arc welding under argon at 1 bar. The tightness of the capsules was tested before the investigation in DTA and DSC in a separate furnace under rough vacuum atmosphere and heated with 5 K/min up to a temperature at least 20K higher than the intended investigation temperature.

2.6 Key sample selection and the materials balance algorithm

Selecting the key samples for the investigation with DSC or DTA is rather simple for binary systems, manageable for ternary systems **but** increasingly complex for systems with four or even more components.

Measuring the temperature of invariant reactions has been proven to be quite reasonable, since these temperatures do not change over a certain composition range and are often only slightly influenced by effects like supercooling. Other phase boundaries and especially the liquidus temperature have sources for deviations.

In order to identify decisive sample compositions, a procedure has been developed which gives for any investigated invariant reaction the real composition of the centroid. This sample will give the maximum possible amount of heat exchange for this reaction.

This procedure is valid for any multicomponent sample, since it is based on the fundamental rule of the mass balance.

The required inputs are the compositions x_i^φ of all involved phases φ and elements i and at least an estimate of the invariant temperature, T$_{inv}$.

The theory will be discussed with the example of a three-component, four-phase invariant equilibrium since it is both good imaginable and drawable.

Based on the reaction

$$L + \alpha = \beta + \gamma \tag{2.10}$$

as presented in Fig. 2.6 ,
L + α are the educts *(ed)* and
β + γ are the products *(prod)*.

Step 1: Average composition

In the first step one has to get an alloy (① in Fig. 2.6) with a composition inside the invariant equilibrium.

In the data about this invariant reaction provided by Pandat (the table of invariant reactions involving the Liquid phase is a standard output after calculating the projection of the liquidus surface) we get the compositions x_i^φ of the involved phases φ. Calculating the average composition of these phases $\overline{x_i}$ for all elements i will give us a point ① somewhere in the center of the room spanned by the phases.

Step 2: Phase fraction increments and reaction equation

In the second step we have to use a line-calculation which means a 1D point-to-point calculation at constant pressure and chemical composition and varying temperature.

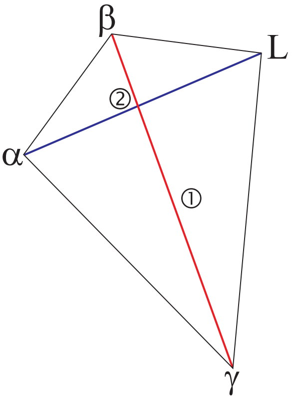

Fig. 2.6: Systematic view of a transition type invariant four-phase reaction in a ternary system.

We use the composition $\overline{x_i}$ of this alloy ① to do the closer calculation at the invariant reaction. This is much better than taking the composition of the liquid phase L, which is just scratching on the equilibrium space. This will only give good results for eutectic reactions and not for those of peritectic or transformation type.

The line-calculation will give us the phase amounts f^{φ} of each phase φ against the temperature. Important are essentially two temperatures: slightly above and below the temperature of the investigated invariant reaction, $\mathrm{T}_{inv} \pm \delta T$.

From the line-calculation at ($\mathrm{T}_{inv} + \delta T$, $\mathrm{T}_{inv} - \delta T$) we will get the individual phase fractions before ($+\delta T$) and after ($-\delta T$) the reaction.

In an n-component system at constant pressure we have $n+1$ phases in equilibrium at an invariant reaction and one less phases, total n, above and below that invariant. At both $\mathrm{T}_{inv} + \delta T$ and $\mathrm{T}_{inv} - \delta T$ the phase fractions are well defined at composition ① and the sum of all phase fractions at constant temperature is equal 1:

$$\sum_{j=1}^{n} f^{\varphi_j} = 1 \tag{2.11}$$

Furthermore the difference between the fractions of each participating phase φ which is transformed by the invariant reaction is

$$\Delta f^{\varphi} = f^{\varphi,after\_reaction} - f^{\varphi,before\_reaction} \quad for \quad \varphi = 1,...,n+1. \tag{2.12}$$

It is important to note that, starting with n phases above the invariant, one additional phase must appear at $\mathrm{T}_{inv}$and a <u>different</u> phase must disappear when cooling to $\mathrm{T}_{inv} - \delta T$. Therefore, eq. 2.12 provides information about <u>all</u>$n+1$ phases in the invariant reaction, irrespective of the selection of the specific n-phase equilibrium at $\mathrm{T}_{inv} + \delta T$.

To fulfill the mass balance the following must be true:

$$\sum_{\varphi=1}^{n+1} \Delta f^{\varphi} = \sum_{\varphi=1}^{n+1} f^{\varphi,after\_reaction} - \sum_{\varphi=1}^{n+1} f^{\varphi,before\_reaction} = 1 - 1 = 0 \tag{2.13}$$

We define educts and products by $\Delta f^{\varphi,ed} < 0$ and $\Delta f^{\varphi,prod} > 0$.

Sorting according to negative and positive phase fractions increments gives the actual invariant reaction equation with proper fractions

$$\varphi_1^{ed} + \varphi_2^{ed} + ... + \varphi_k^{ed} = \varphi_{k+1}^{prod} + \varphi_{k+2}^{prod} + ... + \varphi_{n+1}^{ed} \tag{2.14}$$

Based on the definitions above it is obvious that

$$\left| \sum_{j=1}^{k} \Delta f^{\varphi_j,ed} \right| = \left| \sum_{j=k+1}^{n+1} \Delta f^{\varphi_j,prod} \right| . \tag{2.15}$$

<u>Step 3: Alloy composition for complete reaction</u>

In the third step we get the composition of alloy ② with the maximum (complete) transformed phase amounts.

x_i^{Alloy2} is the composition of a sample which will produce the complete invariant reaction: all the educt phases are fully transformed to the products.
It is essential that the differences of the phase fractions need to be normalized to sum up to unity on each side of the reaction:

$$\Delta f^{\varphi_m,ed-N} = \frac{\Delta f^{\varphi_{m,ed}}}{\left| \sum\limits_{j=1}^{k} \Delta f^{\varphi_{j,ed}} \right|} \tag{2.16}$$

$$\Delta f^{\varphi_m,prod-N} = \frac{\Delta f^{\varphi_m,prod}}{\left| \sum\limits_{j=k+1}^{n+1} \Delta f^{\varphi_j,prod} \right|} \tag{2.17}$$

Similar to the reaction equation 2.14 and eq. 2.15 we than get

$$1 = \left|\Delta f^{\varphi_1,ed-N}\right| + \left|\Delta f^{\varphi_2,ed-N}\right| + ... = \left|\Delta f^{\varphi_1,prod-N}\right| + \left|\Delta f^{\varphi 2,prod-N}\right| + ... \tag{2.18}$$

x_i^{Alloy2} is calculated as a weighed average of educt composition (or alternatively, product composition):

$$x_i^{Alloy2} = \sum_{j=1}^{educts} \left(x_i^{\varphi_j,ed} \cdot \Delta f^{\varphi_j,ed-N} \right) = \sum_{j=k+1}^{products} \left(x_i^{\varphi_j,prod} \cdot \Delta f^{\varphi_j,prod-N} \right) \tag{2.19}$$

This procedure has been used to calculate decisive sample compositions for DTA/DSC for the systems investigated with more than three elements.

Reactions of interest were only those where the (Mg)-phase is involved. Furthermore it has to be checked in preliminary calculations if other thermal signals are expected for this sample very close to the temperature of the aimed invariant reaction. If this is the case, the peaks probably can not be separated properly. Calculating the solidification of the sample using different cooling conditions (equilibrium, Scheil) will give an idea of if the sample composition should be shifted.

For the practical use a Microsoft Excel Spreadsheet has been created to calculate the different steps of this procedure when the needed data is put in. It also checks back for typing errors by calculating both the product und educt side which have to give the same results.
It is recommended to include this algorithm into the Pandat program, giving the user a reasonable *composition* of the invariant reactions.

2.7 Special problem of ternary parameters

The impact of using a ternary parameter L, defined by the excess Gibbs energy ${}^{E}G = L \cdot x_1 \cdot x_2 \cdot x_3$, is elaborated in this section. It is emphasized that this impact is very much counter-intuitive compared to the impact of a binary parameter. Therefore, this parameter should only be used very carefully.

2.7.1 General relations in ternary system A-B-C

For a ternary system A-B-C the simplest (symmetric) formulation of the ternary excess Gibbs energy is:

$$ {}^{E}G^{tern} = L \cdot x_A \cdot x_B \cdot x_C \tag{2.20}$$

L is a ternary parameter and x_i are the mol fractions. The corresponding partial terms, if we assume ideal solution of all binary edge systems, are the following:

$$ {}^{E}\overline{G}_A = R \cdot T \cdot ln\gamma_A = L \quad \cdot x_B \cdot x_C \cdot (1 - 2 \cdot x_A) \tag{2.21a}$$

$$ {}^{E}\overline{G}_B = R \cdot T \cdot ln\gamma_B = L \quad \cdot x_A \cdot x_C \cdot (1 - 2 \cdot x_B) \tag{2.21b}$$

$$ {}^{E}\overline{G}_C = R \cdot T \cdot ln\gamma_C = L \quad \cdot x_A \cdot x_B \cdot (1 - 2 \cdot x_C) \tag{2.21c}$$

It is obvious from Eq. (2.21c) that for all ternary alloys with $x_C = 0.5$ we get

$$ {}^{E}\overline{G}_C \quad = R \cdot T \cdot ln\gamma_C = 0 \tag{2.22a}$$

$$ \Rightarrow \quad \gamma_C = 1 \tag{2.22b}$$

$$ \Rightarrow \quad a_c = \gamma_C \cdot x_c = x_c \tag{2.22c}$$

(at $x_C = 0.5$).

In other words along the section $x_c = 0.5$ we have no variation in the activity a_c for any value of the ternary parameter L. This counter-intuitive impact of the ternary excess term is demonstrated in Fig. 2.7 .

In this example, the activity a_C was calculated from the Redlich-Kister (Muggianu) extrapolation of some non-ideal binary data, but that is not important for the following. The same impact of L will occur for any other extrapolation scheme.

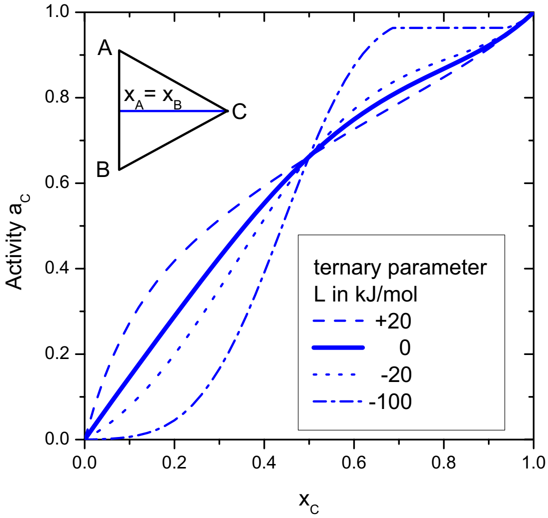

Fig. 2.7: Impact of ternary parameter L on the activity a_C along the equimolar section $x_A = x_B$. The base curve (L=0) was calculated from an extrapolation of some non-ideal binary data.

As one can see in Fig. 2.7 , it is not possible to push the activity curve a_c down (or up) for all alloys on that section by using any value of this simplest (symmetric) ternary L-parameter. An increase of a_c for $x_c < 0.5$ always comes with a decrease of a_c for $x_c > 0.5$ (or vice versa). This impact of the ternary parameter is very much against intuition.

The well known impact of a binary regular solution parameter $L_{A,B}$ on the activity a_B shown in Fig. 2.8 is entirely different from that of the ternary parameter in Fig. 2.7 . Here the binary excess Gibbs energy is $^EG^{bin} = L_{A,B} \cdot x_A \cdot x_B$. In binary systems it is possible to move the entire activity curve up and down, depending on the value of $L_{A,B}$.

This startling behavior can also be illustrated with a comparison of the integral and partial quantities. In spite of the apparent symmetry of the integral excess term in Eq. (2.20), its approach to the value zero at the edge binaries is not at all symmetric. It is quadratic for $x_c \rightarrow 1$ but linear for $x_c \rightarrow 0$ as shown in the top figures of Figs. 2.9(a) and 2.9(b). These figures also demonstrate that the tangent at the integral curve at $x_c = 0.5$ passes through zero at $x_c = 1$, corresponding to the zero value of the partial $^E\overline{G}_C$.

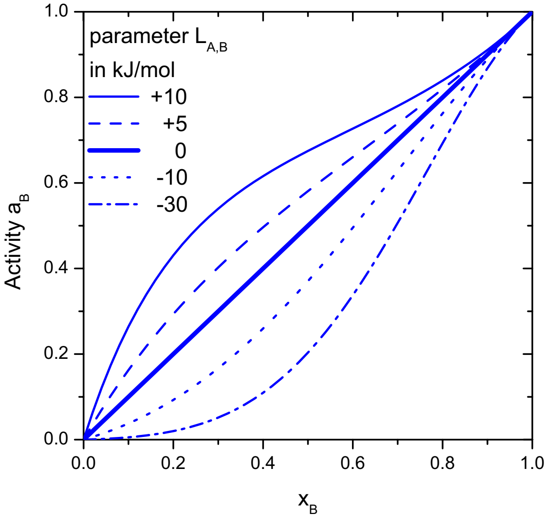

Fig. 2.8: Impact of binary parameter $L_{A,B}$, calculated for T = 727 ° C

2.7.2 Special relations to Redlich-Kister formulation

For a multicomponent solution phase with c components the following equation is used:

$$G^{\phi} = \sum_{i=1}^{c} x_i G_i^{0,\phi} + RT \sum_{i=1}^{c} x_i \ln x_i + {}^{E}G^{bin,\phi} + {}^{E}G^{tern,\phi} + ... \tag{2.23}$$

All excess contributions originating from all the binary interactions (${}^{E}G^{bin}$) or ternary interactions (${}^{E}G^{tern}$) are:

$${}^{E}G^{bin,\phi} = \sum_{i=1}^{c-1} \sum_{j>i}^{c} x_i x_j \sum_{v=0}^{n} L_{ij}^{v,\phi} (x_i - x_j)^v \tag{2.24}$$

$${}^{E}G^{tern,\phi} = \sum_{i=1}^{c-2} \sum_{j>i}^{c-1} \sum_{k>j}^{c} x_i x_j x_k \{ L_{ijk}^{1,\phi}(x_i + \delta_{ijk}) + L_{ijk}^{2,\phi}(x_j + \delta_{ijk}) + L_{ijk}^{3,\phi}(x_k + \delta_{ijk}) \} \tag{2.25}$$

where

$$\delta_{ijk} = (1 - x_i - x_j - x_k)/3 \tag{2.26}$$

It is noted that in a ternary system (c=3) $\delta_{ijk} = 0$. In a quaternary or higher system (or c>3) the same term $\delta_{ijk} \neq 0$.

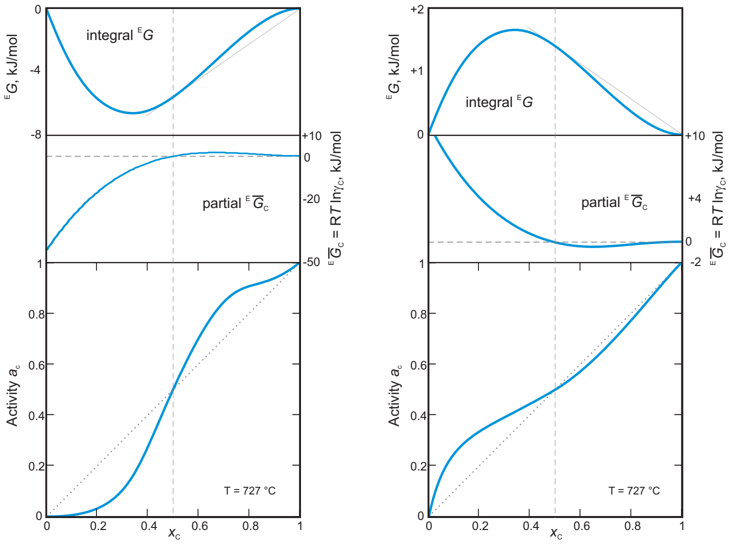

(a) with L = - 200 kJ/mol (b) with L = + 50 kJ/mol

Fig. 2.9: Integral quantity ^{E}G, partial $^{E}\overline{G}_{C}$, and activity a_c along the section x$_A$ = 2·x$_B$,

The particular form of Eq. (2.22c) was presented before [2001Sch], together with corresponding quaternary terms. Instead of Eq. (2.22c) one might have used seemingly simpler equations where the δ_{ijk} term would have been omitted. The main advantage of the given formulation is that Eq. (2.22c) always reduces to the regular solution contribution if all the three L-parameters are identical, as pointed out by Hillert [1980Hil]:

If

$$L_{ijk}^{1,\phi} = L_{ijk}^{2,\phi} = L_{ijk}^{3,\phi} = L_{ijk}^{\phi} \tag{2.27}$$

then

$$^{E}G^{tern,\phi} = \sum_{i=1}^{c-2} \sum_{j>i}^{c-1} \sum_{k>j}^{c} x_i x_j x_k L_{ijk}^{\phi} \tag{2.28}$$

even if $x_i + x_j + x_k \neq 0$ in a quaternary or higher order system [2001Sch, 1980Hil]. This is the more general formulation of the ternary parameter compared to Eq. (2.20). It is emphasized, however, that the startling impact of the ternary parameter is obtained independently of using the Redlich-Kister formulation for extrapolating the binary excess terms. The behavior detailed in section 2.7.1 is related just to the use of a ternary excess term as given in Eq. (2.20) or (2.28).

It is important to point out two more details related to ternary parameters. Firstly, in the widely used tdb-datafile format the ternary parameters are numbered from zero and not from one as in Eq. (2.22c). For example in the liquid phase of Al-Mg-Sr system:

$$L^{\mathbf{1},Liquid}_{Al,Mg,Sr} = \text{PARAMETER G(LIQUID,AL,MG,SR;}\mathbf{0}\text{)}$$

$$L^{\mathbf{2},Liquid}_{Al,Mg,Sr} = \text{PARAMETER G(LIQUID,AL,MG,SR;}\mathbf{1}\text{)}$$

$$L^{\mathbf{3},Liquid}_{Al,Mg,Sr} = \text{PARAMETER G(LIQUID,AL,MG,SR;}\mathbf{2}\text{)}$$

Secondly, a missing parameter may be interpreted by some software by the value zero, whereas some other software may interpret the occurrence of only one parameter as the symmetrical case and set the missing parameters to the same value. It is thus a very wise decision never to use such shortcuts but always to write down **all three parameters** explicitly in a tdb file.

2.7.3 Conclusion

The ternary L-parameter, as defined by Eq. (2.20), should **not** be used as a fitting tool for phase diagrams without carefully checking its impact on activities and comparing with experimental data. It is better not to be used at all if possible, but rather improve on the binary descriptions or on the extrapolation scheme.

Chapter 3

The Mg-Al-Ca-Sr system

Understanding the phase formation in AXJ alloys and modifications of AZ and AM alloys with Ca or Sr requires accurate knowledge about the Mg-Al-Ca-Sr alloy system.

The Calphad approach has been recognized as a powerful method to calculate the phase diagram and thermodynamic quantities for multi-component systems with quite a high degree of accuracy. Importantly, the reliable thermodynamic calculation provides the basis for understanding multi-component solidification behavior. A reliable database is required to secure the quality of the calculations.

Following the route of constructing a multicomponent database as presented earlier in Fig. 2.1 , the starting point for the thermodynamic modeling after the unary descriptions are the thermodynamic datasets for the six binary subsystems Al-Ca, Al-Mg, Al-Sr, Ca-Mg, Ca-Sr and Mg-Sr. These binaries have been already assessed by other authors and were principally taken from the literature; the phase diagrams are briefly discussed in section 3.1 starting on the next page.
In the following steps the four ternary subsystems Mg-Al-Ca, Mg-Al-Sr, Mg-Ca-Sr and Al-Ca-Sr had to be assessed thoroughly in this work. Additional experiments were performed in all these ternaries to fill gaps of information.

The emphasis was put on the two ternary subsystems Mg-Al-Ca (section 3.2 starting from page) and Mg-Al-Sr (section 3.3). These are of central importance for a reasonable description of the multicomponent phase formation and phase equilibria.
The two X-Ca-Sr systems were investigated as well: The distribution of the alloying elements to the different phases should be clarified here.

The quaternary investigation is discussed starting with section 3.6 on page 92 .

A table of all solid phases in the Mg-Al-Ca-Sr system is implemented in Table A.1 in the appendix.

3.1 The binary subsystems

3.1.1 Al-Ca

The Al-Ca system was investigated by Anglezio et al. [1994Ang] and updated with the new phases AlCa and Al_3Ca_8 by Kevorkov et al. [2001Kev2]. Essentially this dataset was used, but with a marginally simplified description for the temperature dependency of the C15-Al_2Ca phase. The parameter B (referred to Eq. 2.8) was changed from +5.02 to +5.0:

$$G^{0,C15}_{AL:CA} = -29700 + 5.0 * T + 0.666667 * G^{0,fcc}_{Al} + 0.333333 * G^{0,fcc}_{Ca} \tag{3.1}$$

The calculated binary phase diagram is shown in Fig. 3.1 , the horizontal line at 443 °C indicates the structure transition of Calcium from face- (α) to body-centered cubic (β).

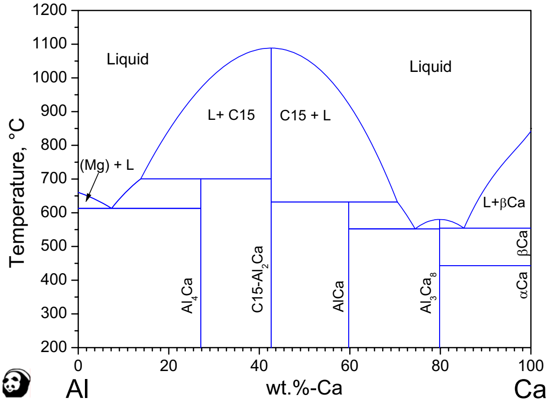

Fig. 3.1: Calculated binary phase diagram of the Al-Ca system.

3.1.2 Al-Mg

The dataset for the central Al-Mg system was optimized by [1998Lia]. Within this phase diagram we have three solution phases (Mg), (Al) and γ-$Mg_{17}Al_{12}$ and two additional stoichiometric compounds β and ϵ. The latter has a limited range of stability, it is only present between 250 and 410 °C.

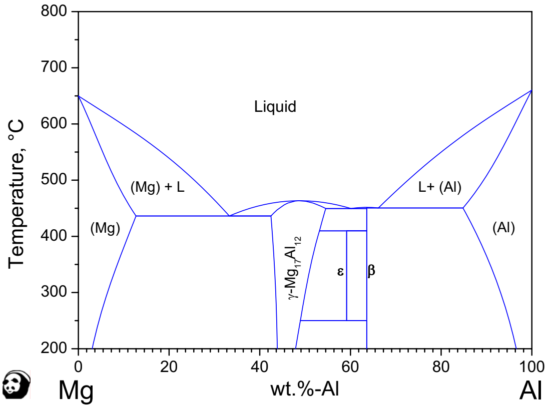

Fig. 3.2: Calculated binary phase diagram of the Al-Mg system.

3.1.3 Al-Sr

The thermodynamic description for the Al-Sr system was taken from [2004Zho]; Version 1 with random solution model and including the compound Al_3Sr_8 was selected. This results in the calculated phase diagram presented in Figure 3.3 . Please note that in contrast to the Al-Ca system, where the Al_2Ca phase is the most stable one, here the Al_4Sr is the predominant phase.

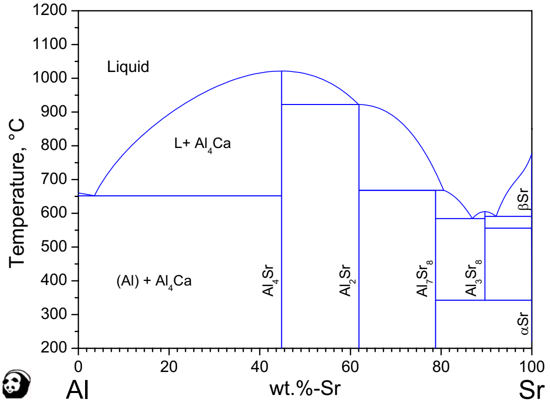

Fig. 3.3: Calculated binary phase diagram of the Al-Sr system.

3.1.4 Ca-Mg

The parameters for the Ca-Mg system where optimized by Agawal et al. in [1995Aga]. The parameters were slightly adjusted to improve the c_p-function of C14-Mg_2Ca as published in [2007Koz]. This is also the only solid binary phase in this system as demonstrated in Fig. 3.4 . Theα/β - transition occurs as usual at at 443 $^\circ$C.

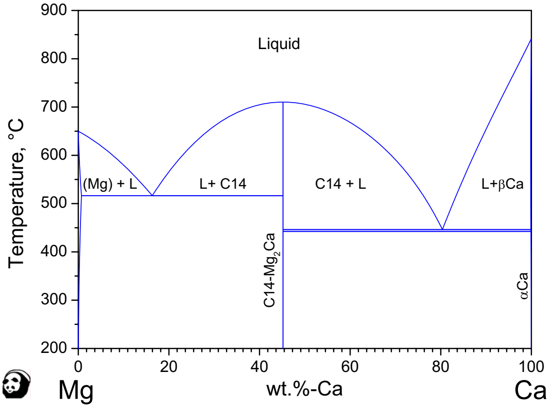

Fig. 3.4: Calculated binary phase diagram of the Ca-Mg system.

3.1.5 Ca-Sr

Fig. 3.5 shows the phase diagram of the Ca-Sr system calculated with the parameters published by Zhong et. al in [2003Zho]. Mutual solubilities between Ca and Sr exist in both the fcc-structured „α “and bcc-structured „β “phase.

3.1.6 Mg-Sr

The Mg-Sr system was assessed and modelled by Zhong et. al [2006Zho]. Four binary compounds exists in this system; the two phases $Mg_{38}Sr_9$ and $Mg_{23}Sr_6$ have a very similar chemical composition. We can also see the structure transition of Sr at 545.5 $^\circ$C in the phase diagram in Fig. 3.6 .

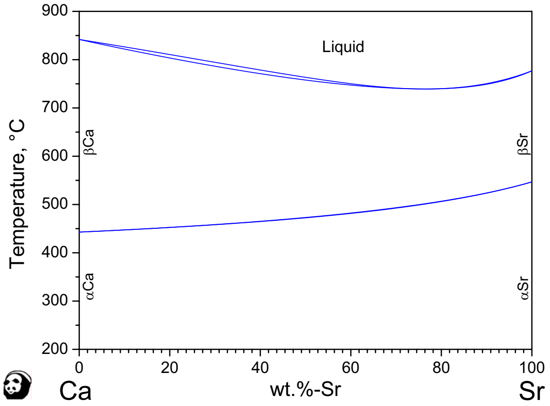

Fig. 3.5: Calculated binary phase diagram of the Ca-Sr system.

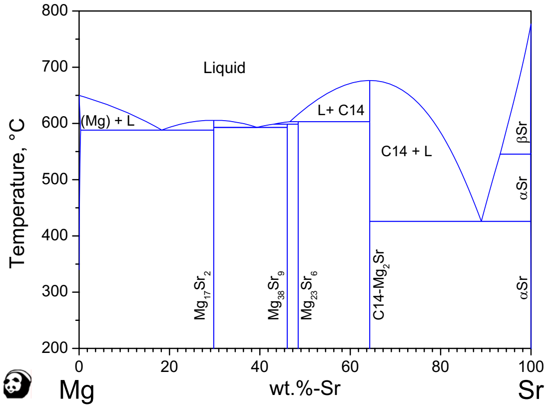

Fig. 3.6: Calculated binary phase diagram of the Mg-Sr system.

3.2 The ternary subsystem Mg-Al-Ca

For a purposeful development of Mg-Al-Ca based alloys as well as for the proper use of Ca as a grain refining addition to AZ or AM alloys, the thermodynamic description of the phase diagram of the Al-Mg-Ca system is required to enable for example solidification calculations. A thermodynamic dataset for this ternary system was published in 2003 [2003Gro], pointing out a remarkable intergrowth between the C14 and C15 Laves phases in some experiments, which made an unequivocal identification with SEM/EDX impossible. Recent investigations proved indeed the existence of a C36-type ternary Laves phase in the Mg-Al-Ca system [2004Suz, 2005Suz , 2007Cao] on the section $CaAl_{2-x}Mg_x$, located between the C14 and C15 phases.

Cao has presented a thermodynamic model for the Mg-rich phase equilibria of the Mg-Al-Ca system. The purpose of the present work is to extend the thermodynamic description to support the calculation of a wider range of alloys in the complete ternary system. A critical evaluation of all available experimental data was performed in conjunction with new experimental work and Calphad-type modeling to generate a complete thermodynamic description.

3.2.1 Experimental data and thermodynamic descriptions in the literature

A first thermodynamic description of the ternary Mg-Al-Ca system has been published by Gröbner et al. 2003 [2003Gro]. This model was based on a literature assessment and experimental data from differential thermal analysis (DTA), X-ray diffraction (XRD), scanning electron microscopy with energy-dispersive X-ray microanalysis (SEM/EDS) and microstructure analysis of as-cast and heat treated samples (300 °C, 3 weeks). The C36 phase was not identified at that time and thus not included into the thermodynamic model. However, the experimentally detected extensive ternary solid solubilities of the C14 (Mg_2Ca) and C15 (Al_2Ca) Laves phases and of Al_2Ca_8 were already reflected in that model.

Amerioun et al. published in the same year their crystallographic results concerning the presence of a $MgNi_2$-type Laves phase on the quasi-binary section $CaAl_{2-x}Mg_x$ based on the investigation of structural changes in the system [2003Ame]. The results were also supported by first-principles calculations.

In the paper of Ozturk et al. [2003Ozt] thermodynamic calculations are compared to literature data and own experiments on two alloys using XRD, EDS and microstructure analysis. The samples were investigated in as-cast status and after heat treatment at 287 °C and 370 °C for one week. A rather simplistic thermodynamic model was used

[2003Ozt] implying no ternary solubilities of the binary solid phases and no ternary interactions either.

Phase equilibria in the Mg-rich corner (50 to 100 wt.% Mg) were investigated by Tkachenko et al. by DTA and XRD with a total of 13 samples [2003Tka]. They also constructed phase diagram sections on the basis of these signals.

Suzuki et al. proved the existence of the C36 phase in Mg-Al-Ca alloys by crystal structure investigation with extensive Transmission Electron Microscopy (TEM) analysis [2004Suz, 2005Suz , 2006Suz]. The report is given in three parts, starting with the general investigation on C36 2004Suz. The results of thermal analysis (TA) are presented in [2005Suz], the findings in isothermal experiments at 400 ° C and 500 ° C using electron probe micro analysis (EPMA) are published in [2006Suz]. They also reported a ternary solubility of Ca in the γ-$Mg_{17}Al_{12}$ phase at 400 ° C of $\sim$ 6 at.% in [2005Suz] and $\sim$4.4 at.% in [2006Suz].

Wang et al. investigated 30 samples in the Mg-Al-Ca system by DSC with a scanning rate of 5 K/min using a graphite crucible [2004Wan]. Eight of these samples are discussed in detail regarding thermal signals, but no information is reported about an investigation of the microstructure of these samples. From the same research group, Islam and Medraj published their work on the thermodynamic modeling of the Mg-Al-Ca system [2005Isl]. They constructed a ternary dataset by extrapolation from the binary subsystems without any ternary interaction. Both the existence of ternary compounds (like the C36 Laves phase) and solid solubilities of the binary compounds were not introduced in this modeling. Aljarrah et al. used DSC, XRD and metallographic techniques to investigate the Mg-Al-Ca system [2007Alj]. A total of 21 samples has been studied and compared to the thermodynamic calculations done with the dataset of [2005Isl]; for 10 of theses 21 samples experimental details are shown. The C36 Laves phase is not mentioned in the experimental results and their discussion.

Zhang et al. report a ternary intermetallic compound with the composition Ca_4Al_3Mg [2005Zha]. The compound was prepared by induction melting followed by heating at 500 ° C for 14 days. It crystallized in the space group *Pbcm* which was investigated using X-ray powder diffraction.

Additional first-principles calculations on the quasi-binary section $CaAl_{2-x}Mg_x$ are presented by Zhong et al. [2005Zho], concluding that the stability of C36 phase is energetically plausible. In a later publication of that group, the calculations were upgraded and experimental work (one diffusion couple held at 415 ° C for two weeks) was added [2006Zho3]. The paper includes an interesting interpretation of the various Al-Ca-Mg Laves phase stabilities including a C36-Al_2(Mg, Ca)-phase, which is a peculiar composition range at constant Al, not Ca, content. Regrettably, only one sample is presented and its diffusion path still remains somewhat unclear, due to the long path from Mg-Ca30 (wt.%) to pure Al and the start in the heterogeneous area (Mg) + C14-Mg_2Ca. Little details are given for the sample preparation (type of encapsulation, way of pressing the two metals); if a silica-capsule was used a contamination by Si cannot be excluded.

The solubility of 'Al_2Ca' in (Mg) has been investigated by Rokhlin et al. [2006Rok]. They assumed a quasi-binary section (Mg) - Al_2Ca while the C36-phase is not mentioned. The effect of the alloying on the electrical resistivity and the hardness of quenched alloys was studied after heating at three different temperatures.

Cao et al. used the technique of directional solidification (DS) to study the solidification paths of three Mg-rich samples [2007Cao]. The samples were investigated using SEM/EPMA and TEM. The experiments confirmed the existence of the C36 Laves phase and proved the eutectic type of the invariant four-phase reaction L $\rightarrow$ (Mg) + C14 + C36. The authors also presented a set of preliminary thermodynamic model parameters which is mainly focused on the Mg-rich corner. Furthermore, the same group of authors used a combined approach of DS, with three alloys, and thermodynamic calculations to establish the saddle points L + (Mg) + C14 and L + (Mg) + C36 [2008Cao].

3.2.2 Experimental study

Based on the previous thermodynamic model [2003Gro] and the new information on the stability of the C36 Laves phase and the solubility of Ca in the γ-$Mg_{17}Al_{12}$ phase, four key samples were selected and prepared to investigate open questions regarding the phase equilibria and liquidus data in this ternary system with DSC/DTA. Their composition is given in Table 3.1 . The samples were prepared from Mg granules (99.98 wt.%, Alfa, Karlsruhe, Germany), Al pieces (99.999 / 99.997 wt.%, Alfa, Karlsruhe, Germany) and Ca pieces (99.99 wt.%, Aldrich-APL, Urbana, IL). All purity designations are related to the metal basis. The weighed materials were pressed carefully to pellets which were then sealed in Ta-capsules by careful electric arc welding under argon at 1 bar.

After testing the tightness of the capsules in a separate furnace, thermal analysis was carried out using a Setaram MHTC 96 Differential Scanning Calorimeter (DSC) for samples #1 to #3 and a Netzsch DTA 404 apparatus for sample #4. The measurements were carried out with heating/cooling rates of 5 and 1 K/min in 3 repeated cycles each. A typical sample weight was about 250 mg. The overall uncertainty of DSC measurements was estimated as ±3 K for temperature determination (±5 K for DTA respectively).

After thermal analysis the samples #1 to #3 were sent to University of Michigan - MSE for microstructural analysis. Details regarding preparation and analysis of the samples are given in [2004Suz, 2005Suz]. sample #4 was selected to cross-check the precision of the TA investigation presented in [2005Suz], the microstructure was analyzed with SEM/BSE imaging and EPMA using a CAMECA SX100 (Cameca, France).

Table 3.1: Temperatures extracted from the DSC/DTA curves obtained by thermal analysis in the Mg - Al - Ca system and their interpretation.

Sample composition in wt.% (Sample No.)	**Thermal signals, ° C**		**Interpretation**
	heating[a]	**cooling**[b]	**Calculated equilibrium phase boundary or invariant reaction**
Mg44.5Al11Ca44.5	720s	720s	720 L/L+C14
(#1)	514w	not detec.	518 L+C14/ L+C14+(Mg)
	-	-	518 L+C14+Mg/ C14+(Mg)
Mg54.8Al38.2Ca7	not cert.	603w	557 L/L+C15
(#2)	-	-	507.7 L+C15/L+C15+C36
	-	-	507.5 L+C15+C36/L+C36
	not cert.	472s	469 L+C36/L+C36+ γ
	not detec.	460w	454 L+C36+γ /C36+γ +(Mg)
	not detec.	445w	-
	438s	438s	438 (Mg)+C36+γ /(Mg)+C15+γ [\$]
Mg15.2Al41.6Ca43.2	955	952s	951 L/L+C15
(#3)	821s	802s	823 L+C15/L+C15+C36
	-	-	818 L+C15+C36/L+C36
	not detec.	783w	-
	-	-	737 L+C36/L+C36+C14
	725s	728s	727 L+C36+C14/C36+C14
	515s	515s	510 C36+C14/C36+C14+C15 [§§]
Mg68.5Al20Ca11.5	-	-	569 L/L+C36
(#4)	535	528	-
	not detec.	525	522 L+C36/ L+C36+(Mg)
	-	-	495 L+C36+(Mg)/C36+(Mg)

[a] Onset for invariant reactions, peak maximum otherwise; Invariant reactions were recognized from the peak shape.

[b] Onset

w = weak and diffuse signal, s = strong and clear signal

not detec. = not detected, not cert. = not certain

[\$] peak shape suggests strong invariant reaction, possibly E_{bin}: L ↔ (Mg) + γ

[§§] peak shape suggests invariant reaction, possibly E1 at 515 ° C

The results of the DSC and DTA-analysis of the four new samples of this work are presented in Table 3.1 . The last column shows the interpretation as obtained from the present thermodynamic calculation for the individual alloys.

The measured phase compositions from EPMA are given in Table 3.2 . The phase identification is based on the phases' chemical composition and the microstructure was analyzed for interpretation of the solidification sequence. The maximum solubilities in the particular phases published in [2003Gro, 2005Suz] (C14, C15, C36 and γ-$Mg_{17}Al_{12}$) were confirmed. The correlation of thermal signals with the microstructure of the solidified samples needs also to be considered. Within the microstructure of sample #1 only one phase was found: C14-Mg_2Ca. The data in Table 3.2 demonstrate a reasonable accuracy of the EPMA composition of this single-phase sample compared with the weighed nominal composition. This finding is also essentially consistent with the calculated equilibrium phase assembly, see Table 3.1 , showing C14 as primary phase plus some additional amount of (Mg), too small to be detected.

Table 3.2: Phase analysis results of the SEM/EPMA investigation of the three DSC samples in the Mg - Al - Ca system.

Sample composition in wt.%; Sample No.	**phase name**	**phase composition in wt.%**		
		Mg	**Al**	**Ca**
Mg44.5Al11Ca44.5 (#1)	C14	44.2	12.2	43.6
Mg54.8Al38.2Ca7 (#2)$^{a)}$	C15	4.5	58.0	37.6
	Al_4Ca	8.4	58.8	32.9
	$\gamma-Mg_{17}Al_{12}$	56.5	39.2	4.3
Mg15.2Al41.6Ca43.2 (#3)$^{a)}$	C15	4.8	52.6	42.7
	C36	17.9	39.6	42.6
	C14	36.1	22.2	41.8
Mg68.5Al20Ca11.5 (#4)	C36	11.0	53.6	35.4
	(Mg)	92.5	7.4	0.1
	$\gamma-Mg_{17}Al_{12}$	60.3	37.5	2.2

$^{a)}$ Additionally observed (Mg) phase was to fine for quantitative EPMA analysis.

The micrograph in Fig. 3.7 displays the mass contrast from back scattered electrons (SEM/BSE) in the sequence Ca-Al-Mg from bright to dark. It shows for sample #2 the existence of four phases; therefore this sample did not reach equilibrium although the final cooling rate was only 1 K/min. As can be seen in the micrograph, (Mg) and γ-$Mg_{17}Al_{12}$ are co-precipitated in a final solidification step. The primary precipitate is obviously C15, consistent with the calculation. Al_4Ca subsequently formed a layer on these large C15 particles, partially consuming them. All phases show significant ternary solubilities.

The microstructure of sample #3 is presented in Fig. 3.8 . The composition of this

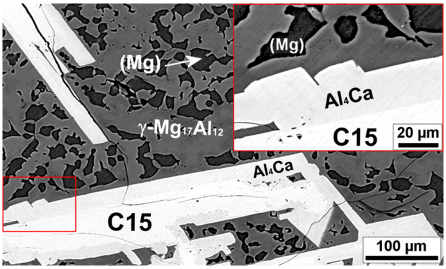

Fig. 3.7: Scanning electron micrograph (SEM/BSE) of sample #2 after slow cooling in DSC; inset on top right shows a higher magnification of a region on the lower left side.

sample is very close to the nominal composition of the C36 phase. The three Laves-phases were formed in the sequence C15-C36-C14. The predicted sequential consumption of the primary C15 phase appears again incomplete, resulting in some deviation from the equilibrium solidification path. Small areas of a very fine (Mg) + C14 microstructure exist as well and this is consistent with the occurrence of the last thermal signal at 515 °C, probably related to a small amount of ternary eutectic. It is also noted that the phase boundary between C15 and C36 is very soft in comparison to the one between C36 and C14.

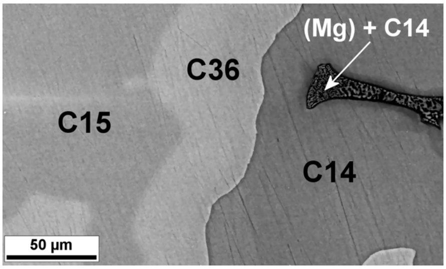

Fig. 3.8: Scanning electron micrograph (SEM/BSE) of sample #3 after slow cooling in DSC.

In Fig. 3.9 the microstructure of sample #4 is displayed. It shows very nicely the fine lamellar eutectic-like C36 + (Mg) – morphology, produced by solidifying along the monovariant equilibrium L ↔ C36 + (Mg). Some larger particles can be assigned as primary precipitates. As for sample #3 the co-precipitation of (Mg) and γ-$Mg_{17}Al_{12}$ occurred in the final step of solidification. The areas of the (Mg) phase in this sample were large enough to be analyzed with EPMA. It dissolved 7.5 wt.% Al but only 0.1 wt.% Ca in accord with the thermodynamic calculations. The eutectic-like microstructure C36 + (Mg) is presented in more detail in Fig. 3.10 . This result is from an alloy Mg-Al17-Ca10 (wt.%), not presented in [2008Cao], but using exactly the same methods of preparation and investigation. The inset shows the TEM SAD pattern that proves the

C36 crystal structure for this sample, passing through the same monovariant equilibrium L ↔ C36 + (Mg) as sample #4.

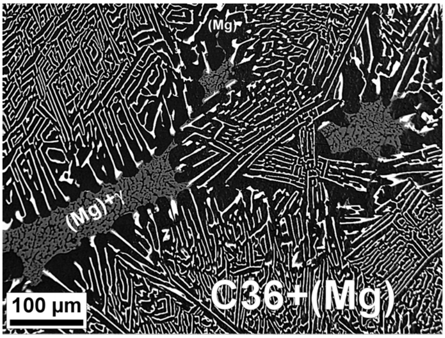

Fig. 3.9: Scanning electron micrograph (SEM/BSE) of sample #4 after slow cooling in DTA.

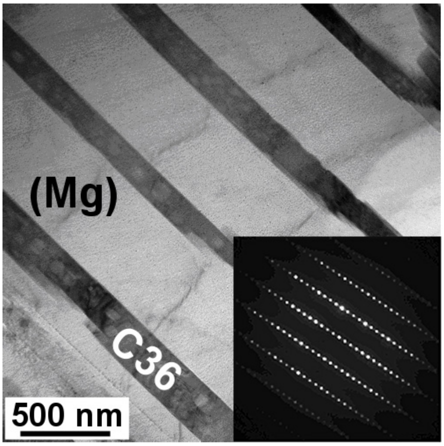

Fig. 3.10: TEM BF image of eutectic-like C36 + (Mg) structure obtained from directionally solidified Mg-Al17-Ca10 (wt.%) alloy. The phase with dark contrast is C36, the bright one is (Mg). The inset shows the TEM selected area diffraction pattern for C36, zone axis: B = $[2\bar{1}\bar{1}0]$.

3.2.3 Thermodynamic modeling

The unary Gibbs energy functions for Al, Ca and Mg are taken from the SGTE compilation by Dinsdale [1991Din], the thermodynamic parameters for the binary systems were taken from the sources discussed in section 3.1 .

The liquid, fcc (Al, αCa), bcc (βCa) and hcp (Mg) solution phases are described by the substitutional solution model. For the liquid phase (L) the molar Gibbs energy is expressed by following Redlich-Kister-type equation:

$$\begin{aligned} G^{Liq} &= x_{Al}G^{0,Liq}_{Al} + x_{Ca}G^{0,Liq}_{Ca} + x_{Mg}G^{0,Liq}_{Mg} + {}^{E}G^{bin,Liq} \\ &+RT\left(x_{Al}\ln x_{Al} + x_{Ca}\ln x_{Ca} + x_{Mg}\ln x_{Mg}\right) + x_{Al}x_{Ca}x_{Mg}\cdot L^{Liq} \end{aligned} \tag{3.2}$$

in which ${}^{E}G^{bin,Liq}$ describes the excess contribution from all binary interactions, R is the gas constant and, x_{Al}, $x_{Ca}\text{and}x_{Mg}$ are the molar fractions of Al, Ca and Mg. The ternary interaction parameter L^{Liq} may be linearly temperature dependent and is optimized for the liquid phase.

The four phases Mg_2Ca (C14), Al_2Ca (C15), Al_3Ca_8 and Al_4Ca were modeled as line-compounds $(\mathbf{Mg},\mathrm{Al})_2\mathrm{Ca}_1$, $(\mathbf{Al},\mathrm{Mg})_2\mathrm{Ca}_1$, $\mathrm{Al}_3(\mathbf{Ca},\mathrm{Mg})_8$ and $(\mathbf{Al},\mathrm{Mg})_4\mathrm{Ca}$ to reflect the experimentally observed ternary solubilities. The element highlighted bold is the major constituent on the particular sublattice. The EPMA data in [2006Suz] suggested that C14 also has some solubility in Ca-Mg direction. This has not been checked in detail but would also imply significant Mg solubility in binary Mg_2Ca. We do not have enough data for a corresponding quantitative revision of the Ca-Mg system, going beyond the binary stoichiometric Mg_2Ca phase assumed by [1995Aga, 2007Koz]. Therefore we continue to use the simplified line compound description at constant Ca-content for the ternary C14 and C15 phases.

The Gibbs energy (per mole of atoms) for $\Phi = Mg_2Ca$ and Al_2Ca is expressed by

$$\begin{aligned} G^{\phi} &= y_{Al}G^{0,\phi}_{Al:Ca} + y_{Mg}G^{0,\phi}_{Mg:Ca} + \tfrac{2}{3}RT\left(y_{Al}\cdot\ln y_{Al} + y_{Mg}\cdot\ln y_{Mg}\right) \\ &+y_{Al}\cdot y_{Mg}\cdot L^{\phi}_{Al,Mg:Ca} \end{aligned} \tag{3.3}$$

in which y_{Al} and y_{Mg} are the site fractions of Al and Mg on the sublattice with variable composition. Similarly, for Al_3Ca_8 we have

$$\begin{aligned} G^{Al3Ca8} &= y_{Ca}G^{0,\phi}_{Al:Ca} + y_{Mg}G^{0,\phi}_{Al:Mg} + \tfrac{8}{11}RT(y_{Ca}\cdot\ln y_{Ca} + y_{Mg}\cdot\ln y_{Mg}) \\ &+y_{Ca}\cdot y_{Mg}\cdot L^{0,\phi}_{Al:Ca,Mg} \end{aligned} \tag{3.4}$$

and for Al_4Ca

$$\begin{aligned} G^{Al4Ca} &= y_{Al}G^{0,\phi}_{Ca:Al} + y_{Mg}G^{0,\phi}_{Ca:Mg} + \tfrac{4}{5}RT(y_{Al}\cdot\ln y_{Al} + y_{Mg}\cdot\ln y_{Mg}) \\ &+y_{Al}\cdot y_{Mg}\cdot L^{0,\phi}_{Ca:Al,Mg} \end{aligned} \tag{3.5}$$

The parameters $G^{0,\phi}_{i:j}$(also called compound energies) are expressed relative to the Gibbs energies of the pure elements (Ca-fcc, Al-fcc, Mg-hcp) at the given temperature T. The proper compound energies $G^{0,Mg2Ca}_{Ca:Mg}$ and $G^{0,Al2Ca}_{Ca:Al}$ represent the stable binary Mg_2Ca and Al_2Ca phases. The values are taken from the binary description of the Ca-Mg [1995Aga, 2007Koz] and Al-Ca [2001Kev2] systems.

For the di-hexagonal ternary Laves phase C36 a more complex three-sublattice model had to be adopted. The crystallographic prototype for this phase is the $MgNi_2$ structure (Pearson symbol hP24, space group $P6_3/mmc$), the stoichiometric formula used in this model is $(\mathbf{Al})_{36}(\mathrm{Al}, \mathbf{Mg})_{14}(\mathbf{Ca}, \mathrm{Mg})_{25}$. Referred to one mole of atoms it is $(\mathbf{Al})_{0.48}(\mathrm{Al}, \mathbf{Mg})_{0.186667}(\mathbf{Ca}, \mathrm{Mg})_{0.333333}$.

Although this is a three-sublattice description, only the second and the third sublattice can vary in composition since the first sublattice is completely occupied by (Al). Therefore, only two site fractions are used as variables. The Gibbs energy for the Laves phase, Φ = C36, is described by the compound energy formalism (CEF) [1986And, 2001Hil], which can be expressed in this case as

$$G^{\phi} = \sum_{i,j} y_i^{II} \cdot y_j^{III} \cdot G^{0,\phi}_{Al:i:j} + 0.186667 \cdot RT \sum_i y_i^{II} \ln y_i^{II} + 0.333333 \cdot RT \sum_j y_j^{III} \ln y_j^{III} + {}^{E}G^{\phi} \tag{3.6}$$

where y_i^{II} (y_j^{III}) is the site fraction of elemental constituents $i(j)$ on the sublattice II (III) and $G^{0,\phi}_{Al:i:j}$ is the Gibbs energy (per mol of atoms) of the formation of (mostly fictitious) compounds, $(\mathrm{Al})_{0.48}(i)_{0.186667}(\boldsymbol{j})_{0.333333}$. ${}^{E}G^{\phi}$ is the excess Gibbs energy expressed as follows,

$$\begin{aligned} {}^{E}G^{\phi} = {} & y^{II}_{Al} y^{II}_{Mg} \cdot y^{III}_{Ca} \cdot L^{\phi}_{Al:Al,Mg:Ca} + y^{II}_{Al} y^{II}_{Mg} \cdot y^{III}_{Mg} \cdot L^{\phi}_{Al:Al,Mg:Mg} \\ & + y^{III}_{Ca} y^{III}_{Mg} \cdot y^{II}_{Al} \cdot L^{\phi}_{Al:Al:Ca,Mg} + y^{III}_{Ca} y^{III}_{Mg} \cdot y^{II}_{Mg} \cdot L^{\phi}_{Al:Mg:Ca,Mg}, \end{aligned} \tag{3.7}$$

where $L^{\phi}_{Al:Al,Mg:M'}$ represents the interaction parameter between Al and Mg on sublattice II when the sublattice III is occupied by M' (Ca or Mg) and $L^{\phi}_{Al:M':Ca,Mg}$represents the interaction parameter between Ca and Mg on sublattice III when the sublattice II is occupied by M' (Al or Mg). The C36 phase has 4 end member compounds in this model.

Also ternary solubility in the binary phase γ-$Mg_{17}Al_{12}$ had to be applied. Already in the binary Mg-Al system the compound energy formalism was selected to describe this phase with the three sublattice model $(\mathbf{Mg})_{10}(\mathrm{Al},\mathbf{Mg})_{24}(\mathbf{Al},\mathrm{Mg})_{24}$. The prototype for γ-$Mg_{17}Al_{12}$ is the A12 body centered αMn structure. The problems of modeling this phase are discussed in [1997Ans], but since Ca is not mentioned at all within this discussion and the question on which sublattice the elements have to be placed remains finally unclear, it was chosen to keep the thermodynamic description as simple as possible and put the Ca on the second sublattice (24g). Doing so less additional parameters for the ternary γ-$Mg_{17}Al_{12}$ are necessary compared to a model where the Ca is put on the first sublattice. Also the field of stability appears to be more reasonable in this case compared to the more symmetric field with Ca on the first sublattice.

The γ-$Mg_{17}Al_{12}$ phase was model as $(\mathbf{Mg})_{10}(\mathrm{Al, Ca}, \mathbf{Mg})_{24}\ (\mathbf{Al}, \mathrm{Mg})_{24}$ in analogy to Equations 3.6 and 3.7 . Again the description can be simplified because this time the first sublattice is completely occupied by (Mg). Due to the triply occupied second sublattice 6 end members occur in Eq. (3.6), compared to only 4 for the C36 phase. Two of the 6 end members are of ternary character whereas the other 4 are known from the binary γ-$Mg_{17}Al_{12}$ description.

All other phases (β, ε and AlCa) were modeled as stoichiometric phases. The ternary compound Ca_4Al_3Mg reported by [2005Zha] was not implemented in the current dataset. Not enough information like melting point or invariant reactions involving this phase is available to model this phase. Furthermore, its existence has not been reported in samples located close to that stoichiometry [2003Gro]. The stability of Ca_4Al_3Mg remains an open question out of the scope of this study.

Results of the final thermodynamic modeling are summarized in the following calculated phase diagrams. The liquidus projection gives an overview and is shown in Fig. 3.11. The corresponding calculated invariant reactions and maxima involving the liquid phase are listed in Tables 3.3 and 3.4 , respectively, and compared with the experimental temperatures. The optimized thermodynamic parameters are given in Table 3.5 .

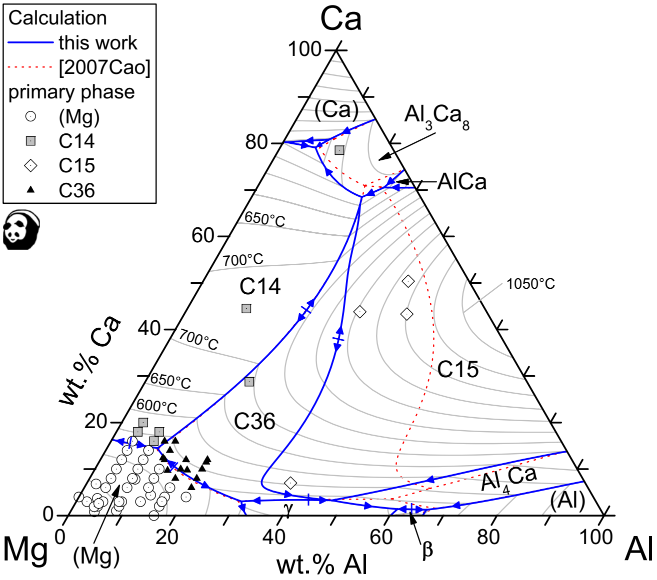

Fig. 3.11: Calculated projection of the Mg-Al-Ca liquidus surface. Superimposed are all those sample compositions for which the primary phase was determined [2003Gro, 2003Tka, 2005Suz , 2007Cao , 2008Cao] and in this work. The dotted monovariant lines are calculated from the data set of [2007Cao].

Table 3.3: Invariant four-phase reactions involving the liquid phase in the ternary Al-Mg-Ca system

Type	**T/ ° C calcul.**	**Reaction**	**Liq. wt.% Al**	**Liq. wt.% Ca**	**T/ ° C exper.**	**Ref.**
U1	545	L + C36 ↔ C14 + C15	21.0	66.9		
U2	531	L + AlCa ↔ C15 + Al_3Ca_8	23.7	70.5		
E1	515	L ↔ (Mg) + C14 + C36	9.4	14.5	515 514 ∼ 514 516	this work [2003Gro] [2005Suz] [2007Cao]
U3	512	L + C15 ↔ C14 + Al_3Ca_8	20.6	68.5	506 513	[2003Gro] [2007Alj]
U4	474	L + C36 ↔ γ-$Mg_{17}Al_{12}$ + C15	46.8	3.3		
U5	473	L + C15 ↔ Al_4Ca + γ-$Mg_{17}Al_{12}$	47.5	3.3		
U6	454	L + C36 ↔ (Mg) + γ-$Mg_{17}Al_{12}$	30.8	3.1	452	[2005Suz]
E2	446	L ↔ (Al) + Al_4Ca + β	66.2	1.3		
E3	445	L ↔ Al_4Ca + β + γ-$Mg_{17}Al_{12}$	60.7	1.4		
U7	442.5	Al_3Ca_8 + βCa ↔ L + αCa	8.3	80.8		
D	442.2	L + {βCa ↔ αCa} + C14	0.7	80.3		
E4	402	L ↔ αCa + C14 + Al_3Ca_8	6.6	79.1	410	[2003Gro]

Table 3.4: Invariant ternary three-phase reactions involving the liquid phase in the Al-Mg-Ca system

Type	**T/ ° C calculated**	**Reaction**
Max1	833	L + C15 ↔ C36
Max2	737	L + C36 ↔ C14
Max3	526	L ↔ (Mg) + C36
Max4	518	L ↔ (Mg) + C14
Max5	476	L ↔ γ-$Mg_{17}Al_{12}$ + C36
Max6	447	L ↔ Al_4Ca + β

Table 3.5: Ternary thermodynamic parameters for the Al-Mg-Ca system.

Phase	Model[a]	Parameters in J/mol
Liquid	(Mg, Al, Ca)	$L^{Liquid}_{Al,Ca,Mg} = -22000 - 3 \cdot T$
C14 (Mg_2Ca)	(**Mg**, Al)$_{0.667}$ (Ca)$_{0.333}$	$G^{0,Mg_2Ca}_{Al:Ca} = -24700 + 3 \cdot T + 0.667G^{0,FCC}_{Al} + 0.333G^{0,FCC}_{Ca}$
C15 (Al_2Ca)	(**Al**, Mg)$_{0.667}$ (Ca)$_{0.333}$	$G^{0,Al_2Ca}_{Mg:Ca} = -4820 + 0.667G^{0,HCP}_{Mg} + 0.333G^{0,FCC}_{Ca}$
C36	(Al)$_{0.48}$ (Al, **Mg**)$_{0.187}$ (**Ca**, Mg)$_{0.333}$	$G^{0,C36}_{Al:Mg:Ca} = -23095 + T + 0.48G^{0,FCC}_{Al} + 0.187G^{0,HCP}_{Mg} + 0.333G^{0,FCC}_{Ca}$ $G^{0,C36}_{Al:Mg:Mg} = -400 + 0.5 \cdot T + 0.48G^{0,FCC}_{Al} + 0.52G^{0,HCP}_{Mg}$ $G^{0,C36}_{Al:Al:Mg} = 2350 + 2 \cdot T + 0.667G^{0,FCC}_{Al} + 0.333G^{0,HCP}_{Mg}$ $G^{0,C36}_{Al:AL:Ca} = -27900 + 5 \cdot T + 0.667G^{0,FCC}_{Al} + 0.333G^{0,FCC}_{Ca}$ $L^{C36}_{Al:Al:Ca,Mg} = -4700$ $L^{C36}_{Al:Mg:Ca,Mg} = -4700$ $L^{C36}_{Al:Al,Mg:Ca} = -1000$ $L^{C36}_{Al:Al,Mg:Mg} = -4550$
Al_4Ca	(**Al**, Mg)$_{0.8}$ (Ca)$_{0.2}$	$G^{0,Al_4Ca}_{Mg:Ca} = -6000 + 0.8G^{0,HCP}_{Mg} + 0.2G^{0,FCC}_{Ca}$
Al_3Ca_8	(Al)$_{0.273}$ (**Ca**, Mg)$_{0.727}$	$G^{0,Al_3Ca_8}_{Al:Mg} = 5000 + 0.273G^{0,FCC}_{Al} + 0.727G^{0,HCP}_{Mg}$ $L^{Al_3Ca_8}_{Al:Mg,Ca} = -25000 + 5 \cdot T$
$\gamma-Mg_{17}Al_{12}$	(**Mg**)$_{10}$ (Al,Ca,**Mg**)$_{24}$ (**Al**,Mg)$_{24}$	$G^{0,\gamma}_{Mg:Ca:Al} = -650000 + 70 \cdot T + 10G^{0,HCP}_{Mg} + 24G^{0,FCC}_{Ca} + 24G^{0,FCC}_{Al}$ $G^{0,\gamma}_{Mg:Ca:Mg} = 100000 + 34G^{0,HCP}_{Mg} + 24G^{0,FCC}_{Ca}$ $L^{\gamma}_{Mg:Ca,Mg:Al} = -1090000 + 50 \cdot T$

[a] Six significant digits were used in the stoichiometry of models normalized to one mol of atoms, such as (Al)$_{0.48}$(Al, **Mg**)$_{0.186667}$(**Ca**, Mg)$_{0.333333}$ for C36

3.2.4 Discussion

The preliminary thermodynamic description presented by Cao et. al. [2007Cao] has been focused on the Mg-rich corner of the phase equilibria; especially, a precise determination of type and composition of the eutectic reaction L ↔ (Mg) + C14 + C36 was performed. The challenge of the present work was to retain this proven description for the Mg-rich phase equilibria while developing a more global model, considering all experimental data pertinent to the entire Al-Ca-Mg system.

The most important experimental data for the modeling are the invariant reactions, the primary precipitating phases, the ternary solubilities and the results of the phase assemblies after heat treatment at various temperatures. They are compared in the following to the calculated phase diagrams. This system shows some very sensitive reactions where phase transition temperatures or compositions may be shifted vastly by just minute changes in corresponding Gibbs energies. This applies in particular to the transitions between C15 and C36; these two Laves phases resemble each other much more closely than the third Laves phase in this group, which is C14.

3.2.4.1 Liquidus surface, primary phases and invariant reactions

The projection of the calculated liquidus surface in Fig. 3.11 shows a comparison with the experimentally determined primary crystallizing phases from all literature data [2003Gro, 2003Tka , 2005Suz , 2007Cao , 2008Cao] and this work. It also compares the present calculation with that from the preliminary thermodynamic description [2007Cao] and demonstrates that the Mg-rich corner is virtually identical. Especially the eutectic reaction E1: L ↔ (Mg) + C14 + C36 is located at a liquid composition of Mg76.1-Al9.4-Ca14.5 (wt.%), practically the same compared with the model of [2007Cao], Mg76.2-Al9.5-Ca14.3 (wt.%). The calculated eutectic temperature of 515 °C is even closer to the experimental values, see Table 3.3 . It shall thus be referred to that work [2007Cao] for a more detailed comparison to the experimental evidence in the Mg-rich corner, also from directional solidification, which shall not be repeated here. This also applies to the two saddle point maxima on the monovariant eutectic troughs, L ↔ (Mg) + C14 and L ↔ (Mg) + C36, experimentally established by directional solidification [2008Cao], and calculated likewise by the present comprehensive model as shown in Fig. 3.11 .

The eutectic-like microstructure solidifying along the monovariant L ↔ (Mg) + C36 line is demonstrated in Fig. 3.10 . This result is from an alloy Mg-Al17-Ca10 (wt.%), not presented in [2008Cao], but using exactly the same methods of directional solidification and TEM investigation. In addition to supporting the calculated eutectic-type three-phase equilibrium it also demonstrates in the TEM SAD pattern that C36, and not the competing C15, is involved. Another alloy in the work of Cao et al. [2008Cao], following that solidification path even deeper, showed in the micrographs additional Mg + γ-$Mg_{17}Al_{12}$ microstructure, supporting the transition type of the calculated invariant four-phase reaction U6: L + C36 ↔ (Mg) + γ. The calculated temperature at 454 °C is not only in accord with an experimental value, see Table 3.3 , it is also 15 K above the corresponding binary Mg-Al eutectic L ↔ (Mg) + γ (439 °C); therefore, this monovariant line descends into that binary edge in Fig. 3.11 . This descend is also consistent with the reaction type of U6 and due to the substantial solid solubility of Ca in γ-$Mg_{17}Al_{12}$.

The ternary Laves phase C36 is formed in a peritectic reaction at 833 °C, L + C15 ↔ C36, at the maximum in the corresponding monovariant line in Fig. 3.11 . Its field of primary precipitation extends widely towards Mg. This is in good agreement with the experimental data identifying C36 as primary phase in samples at higher Mg content, as shown on the liquidus surface.

Compared to the results of the thermodynamic description focused on the Mg-rich corner of the liquidus surface [2007Cao], significantly different results are obtained in the Mg-poor region. The present work essentially provides larger primary fields of the Al-Ca based phases C15, Al_4Ca and Al_3Ca_8. Most obvious is the shift of the L + C15 + C36 equilibrium from the dotted monovariant line to much higher Mg content. The primary precipitates of C15, as observed in the experiments, are now consistently described by the calculation with the new parameters. The extension of the primary C15 field also results in a contact to the γ-$Mg_{17}Al_{12}$ primary field and, consequently, to the new reaction U4: L + C36 $\leftrightarrow$ γ C15 at 474 $^\circ$C.

The primary fields of C15 and C36 merge with almost no bend on the liquidus surface as demonstrated by the smooth course of the isothermal lines when passing the L + C15 + C36 monovariant line. This also indicates the similarity of C15 and C36, which was also noted during the modeling work: subtle changes in the Gibbs energies of these two phases result in significant differences in their competing equilibria. A quite different reason causes the enlargement of the primary fields of Al_4Ca and Al_3Ca_8 compared to [2007Cao]; this is due to the introduction of ternary Mg-solubilities in these Al-Ca phases, as will be discussed with the experimental evidence more detailed in section 3.2.4.2 . The phase with the largest impact of ternary solubilities on its stability field is C14. The solid solubility of Al in Mg_2Ca is even larger than in the liquid phase, resulting in an ascending liquidus surface of C14 in that direction. This will be discussed in more detail in section 3.2.4.4 .

3.2.4.2 Isothermal sections

The four isothermal phase diagram sections, calculated from the present thermodynamic model and shown in Figs. 3.12(a) to 3.12(d), emphasize the significant changes within the Mg-Al-Ca system between 300 and 600 °C. In Figs. 3.12(a) to 3.12(c) all the sample compositions are marked that were equilibrated at the corresponding temperature, quenched and the results of the phase analysis are also given [2003Gro, 2005Zha , 2006Suz].

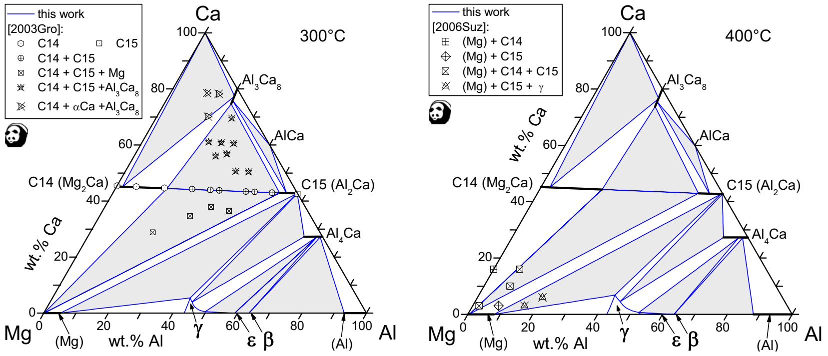

(a) 300 °C (b) 400 °C

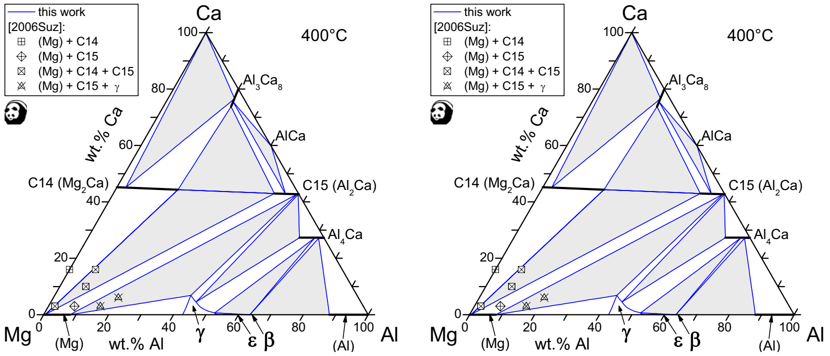

(c) 500 °C (d) 600 °C

Fig. 3.12: Calculated isothermal sections at the given temperatures. Solid solubilities of binary phases are highlighted with bold lines, light grey areas indicate three-phase regions. The ternary phase C36 is stable only in the 500 and 600 °C sections. Superimposed are the compositions of samples with phase analysis after heating at the given temperature [2003Gro, 2005Zha , 2006Suz].

At 300 °C we can see all binary solid phases stable within this system. Ternary solubilities of binary phases modeled as line compounds are highlighted with bold lines, these are C14, C15, Al_4Ca and Al_3Ca_8. The terminal solid solutions of hcp (Mg) and fcc (Al) appear also as a line since their Ca-solubility is too small to be shown on the graph. The Ca-solubility in γ-$Mg_{17}Al_{12}$ is so large that a single-phase field clearly appears for this solid solution phase with three sublattices. This large Ca-solubility may have a substantial impact on the physicochemical properties, for example the corrosion properties, of this phase. The ternary Laves phase C36 is not yet stable at this temperature. The experimental data from [2003Gro] are reproduced very well by the calculation.

At 400 °C the C36 phase is still not stable. We can see that the ternary solubilities of the binary phases are extended compared to the calculation at 300 °C. The experimental phase analysis data of [2006Suz] at 400 °C are reproduced completely by the thermodynamic model; the measured phase composition data are also essentially in accord with the calculation.

The C36 phase becomes stable slightly above 400 °C, and it is present with a quite substantial solubility range at 500 °C, extending from the C14 - C15 section to a Ca-deficient region. The binary Al-Mg compounds are already molten at this temperature; a second liquid region emerges from the Ca-rich ternary eutectic E4 and extends into the binary Mg-Ca edge. Nearly all of the experimental data of [2006Suz] (phase occurrence and, in essence, EPMA-composition) are in agreement with this calculation. Only one sample does not fit: it is the one near the edge of the ternary C14 solubility limit. One may argue that on cooling this sample actually passes through the C14 + C36 field which are the phases detected in that sample. The position of the suggested ternary phase Ca_4Al_3Mg reported from an experiment at 500 °C by [2005Zha] is also shown in this section.

The calculated isothermal section at 600 °C in Fig. 3.12(d) shows extended areas of both the (Mg, Al)-rich liquid and the Ca-rich liquid. All three Laves phases C14, C36 and C15 are in equilibrium with both these liquids. The ternary solubility of Al_4Ca is smaller compared to the calculation at 500 °C whereas the ones for C14 and C15 are even larger. The phase region of C36, already narrower compared to 500 °C, is due to vanish into a single point at 833 °C.

3.2.4.3 Vertical phase diagram sections with constant Al content

For Mg-rich alloys many experimental data are available from both thermal analysis (TA, DTA, DSC) and the phase assembly analysis after equilibration at various temperatures. For a concise comparison of these results with the present calculation four parallel vertical sections in the Mg-rich corner were selected with constant Al concentrations of 4, 8, 16 and 20 wt.% because most of the experiments were placed on these sections or close-by. In all vertical sections the calculations are compared to those performed with the dataset of [2007Cao].

The first two diagrams Figs. 3.13 and 3.14 represent sections which have less Al than the ternary eutectic liquid of the E1 reaction, L ↔ (Mg) + C14 + C36. Thus only one alloy in Fig. 3.13 and only four alloys in Fig. 3.14 actually pass through that ternary eutectic after some primary/secondary equilibrium solidification. The superimposed data from thermal analysis [2005Suz] and especially the results of the phase assembly analysis at 400 and 500 °C [2006Suz] are reproduced very well. However, the liquidus signals of all samples with C14 as primary phase are below the calculation (15∼25 K). This may be safely considered as supercooling effect since there is no way to obtain lower liquidus lines of C14 in a thermodynamically consistent way while retaining the precisely reflected separation between primary crystallizing C14 and (Mg), detailed above.

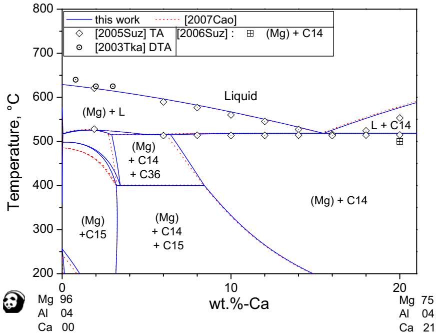

Fig. 3.13: Calculated vertical section at constant 4 wt.% Al; dotted lines are calculated with the parameters of [2007Cao]. Superimposed are experimental data from [2003Tka, 2005Suz, 2006Suz]. In addition to thermal analysis data (TA, DTA) the phase assembly is given for a sample at 20 wt.% Ca, equilibrated at 500 °C.

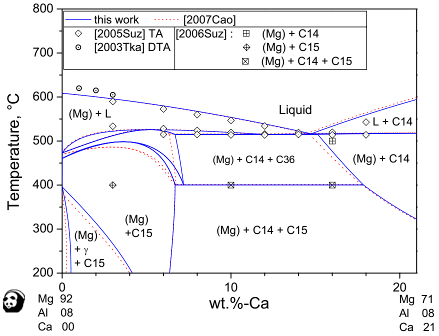

Fig. 3.14: Calculated vertical section at constant 8 wt.% Al; dotted lines are calculated with the parameters of [2007Cao]. Superimposed are experimental data from [2003Tka, 2005Suz, 2006Suz]. In addition to thermal analysis data (TA, DTA) the phase assembly is given for samples equilibrated at 400 and 500 °C.

The DTA data of [2003Tka] are 5 to 15 K above the calculated liquidus line, which cannot be explained with the higher Al-content of 4.5 and 8.5 wt.% compared with the sections in Figs. 3.13 and 3.14 , respectively. Remarkably, the liquidus signal of the sample with the smallest Ca content is even above the liquidus point in the binary in both diagrams. The initial rise of the liquidus line starting from the binary edge system as plotted in all three polythermal phase diagram sections in [2003Tka], just to meet the data points, is not agreeable. Such a rise is identified as a thermodynamic impossibility by the calculations since there is no corresponding irregularity in the solid solubility of (Mg). Only the liquidus signals of [2003Tka] are shown for comparison in Figs. 3.13 and 3.14 since the other signals are very scattered compared to the data of [2005Suz]. The results of the present calculations on these two sections at 4 and 8 wt.% Al are virtually identical to those performed with the dataset of [2007Cao], despite minor changes on the left side of the diagrams. These are related to the C36/C15 transformation.

The section at 12 wt.% Al is similar to the one at 16 wt.% Al presented in Fig. 3.15 ; both have more Al than the ternary eutectic liquid of the E1 reaction. Therefore, the phase field L + C14 is not found but L + C36. The liquidus signals for this equilibrium L/L+C36 [2005Suz] fit the calculation much better than those for L + C14 shown in Figs. 3.13 and 3.14 . The other thermal signals are also reasonably well reproduced by the model; the results of the phase assembly analysis [2006Suz] are in perfect agreement. If we compare the present calculations with that based on the preliminary dataset of [2007Cao], some refinement is observed, again related to the C36/C15 transformation. The calculated temperature of the reaction U6: L + C36 ↔ (Mg) + γ-$Mg_{17}Al_{12}$, 454 °C, is 4 K lower and therefore closer to the experimental data of [2005Suz], see Table 3.3 . The solid transformation reaction (Mg) + C36 ↔ γ-$Mg_{17}Al_{12}$+ C15, almost coinciding with U6 when calculated with the preliminary parameters [2007Cao] occurs now 18 K lower at 438 °C. Again we see the phase field of (Mg) + γ-$Mg_{17}Al_{12}$ slightly widened due to the larger solubility of Ca in the γ-phase.

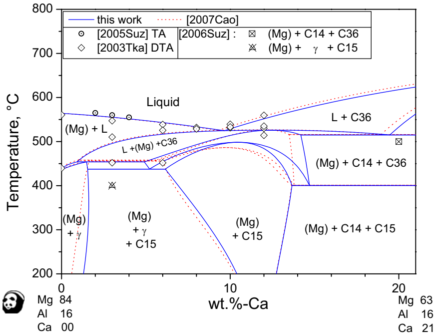

Fig. 3.15: Calculated vertical section at constant 16 wt.% Al; dotted lines are calculated with the parameters of [2007Cao]. Superimposed are experimental data from [2003Tka, 2005Suz, 2006Suz], including samples equilibrated at 400 and 500 °C.

The section at 20 wt.% Al in Fig. 3.16 appears quite similar to that at 16 wt.% Al. On this section additional information was available from the new DTA experiments (sample #4) as well as from the DSC investigations by [2004Wan] and [2007Alj]. The highest signal of the DSC sample at 7.2 wt.% Al [2007Alj] cannot be explained by a reasonable liquidus surface and may be considered an artifact. The differences between the two thermodynamic models are again small in the region of small Ca-content; both represent the entirety of experimental results quite well.

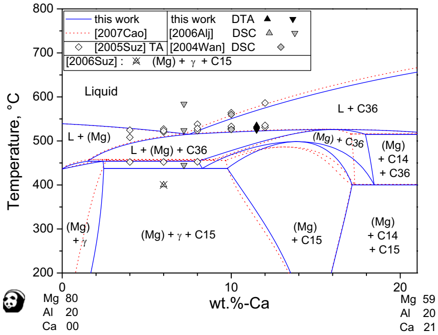

Fig. 3.16: Calculated vertical section at constant 20 wt.% Al; dotted lines are calculated with the parameters of [2007Cao]. Superimposed are experimental data from this work and [2004Wan, 2005Suz , 2007Alj , 2006Suz], including samples equilibrated at 400 and 500 ° C.

One further section with constant Al-content at 38 wt.% Al, thus parallel to the ones discussed above, is presented in Fig. 3.17 to demonstrate the impact of the maximum solubility of Ca in γ-$Mg_{17}Al_{12}$. Furthermore, sample #2 is located on this section. In contrast to the model of [2007Cao], the new parameters predict a primary precipitation of C15 for this sample which matches the experimental observation in Fig. 3.7 . Although most of the thermal signals from the DSC analysis fit quite well to phase boundaries, they have to be treated carefully since the microstructure showed four phases, therefore this sample did not reach equilibrium. Also reactions which should have a large heat effect based on the calculation gave only weak signals and vice versa. The maximum in the monovariant line L ↔ C36 + γ-$Mg_{17}Al_{12}$ is very close to the reaction U4: L + C36 ↔ γ-$Mg_{17}Al_{12}$ + C15 in Fig. 3.11 . We may thus assume that a separation might have occurred in the solidification path of this sample with one part proceeding to the growth of Al_4Ca, resulting in the coarse lamellar structure C15 + Al_4Ca, and another part proceeding to the Mg-rich side from the maximum, producing the finer γ + (Mg) structure in Fig. 3.7 . The lowest thermal signal found at 438 ° C with a peak shape indicating a quite strong invariant reaction supports this interpretation, being related to the binary Mg-Al eutectic, L ↔ (Mg) + γ at 439 ° C, as a non-equilibrium termination of solidification. By contrast, the ternary solid transformation reaction (Mg) + C36 ↔ γ-$Mg_{17}Al_{12}$+ C15, shown at 438 °C in Fig. 3.17 , displays only a feigned agreement with the DSC signals since only a small heat effect is predicted by the equilibrium calculation.

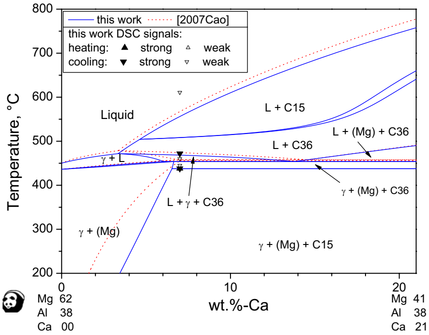

Fig. 3.17: Calculated vertical section at constant 38 wt.% Al; dotted lines are calculated with the parameters of [2007Cao]. Superimposed are experimental data from this work. The extended solid solubility of Ca in γ-$Mg_{17}Al_{12}$ is demonstrated in this section.

3.2.4.4 Vertical phase diagram sections Mg_2Ca-Al_2Ca

The very complex phase relations within the area between C14 (Mg_2Ca) and C15 (Al_2Ca), "almost" passing the C36 phase, should be discussed with the two diagrams presented in Figs. 3.18 and 3.19 .

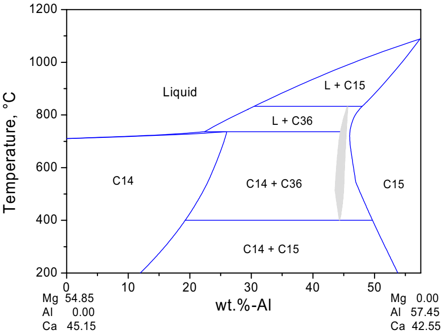

Fig. 3.18: The semi-quantitative ideal pseudo-binary vertical section C14 (Mg_2Ca) - C15 (Al_2Ca) at a molar fraction of Ca of 1/3. The grey area indicates the projected phase field of C36 $(Al,Mg)_2Ca$.

For a better understanding the first graph (Fig. 3.18) shows the semi-quantitative ideal pseudo-binary section between the stoichiometric end points Mg_2Ca and Al_2Ca.

Since these two phases are modeled as line compounds with only mutual solubilities along that section all the equilibria among C14, C15 and Liquid are quantitative with all tie lines located in that section. By contrast, the C36 phase has a variable composition range with Ca deficit and its single phase field touches the section C14 - C15 only selectively, as can be seen in the isothermal sections at 500 and 600 ° C in Fig. 3.12 . Therefore, the range of the 'C36 field' in this diagram, which is indicated by the grey area, displays the projection of the maximum solubilities of C36 at each temperature in equilibrium with C14, C15 or Liquid, respectively, onto this section, at constant Mg/Al-ratio.

Figure 3.18 shows clearly - and quantitatively - the huge solubility ranges of C14 and C15. The mutual solubility in solid C14 is even larger than in the equilibrium liquid phase, causing a rise in its melting point in a very narrow L+C14 phase field. The slope of the liquidus line of C14 is only rising slowly with increasing solute amount of Al until the sharp bend caused by passing the reaction L + C36 ↔ C14. On the other hand there is hardly any difference in the slope of the liquidus lines when the primary precipitation changes between C15 and C36.

The two peritectic reactions L + C15 ↔ C36 at 833 ° C and L + C36 ↔ C14 at 737 ° C essentially coincide with the two maxima on the liquidus surface between these phases in Fig. 3.11 . The eutectoid reaction shown in Fig. 3.18 , C36↔ C14 + C15 at 400.3 ° C is actually related to the invariant ternary eutectoid C36 ↔ C14 + C15 + (Mg) because of the small Ca-deficit of C36. Two of the projected phase boundaries in the C14-C15 section show bends which are caused by the technique of projecting the phase equilibria of C36 from ternary isothermal sections. The bend in the boundary C15 / C15 + C36 at 545 ° C refers to the lowest temperature at which the C36 single phase field touches this section. Below 545 ° C we have additional phases, Liquid or (Mg), in the projected C15 + C36 field. The second bend is in the C14 + C36 / C36 boundary at 515 ° C and corresponds to the occurrence of additional (Mg) in the C14 + C36 field at the Mg-rich side of C36.

Of course it is practically impossible to prepare samples exactly at this $''33.\bar{3}\ at.\%\ Ca''$ section due to weighing uncertainties and oxidation problems. One will always run into the equilibria either towards the Ca corner or the (Mg, Al) side during solidification. To eliminate this ambiguity the new samples #1 and #3 have been placed onto a section with slightly less Ca content, presented in the second diagram Fig. 3.19 . Superimposed into this diagram are the thermal signals from these two DSC samples, from a DTA sample at 32.5 wt.% from [2003Gro] and the results from the phase assembly analysis of two samples at 500 ° C from [2006Suz]. The calculation is again compared with a calculation performed with the parameter set of [2007Cao]. The main differences are the composition of the C36 phase and the corresponding two-phase fields, the formation temperature of C36 and the equilibria with the two other laves phases. The higher extension of the three-phase field C14 + C36 + C15 is reproduced nicely by the phase assembly of the 500 ° C sample at

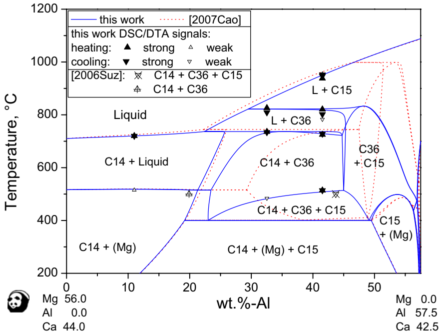

Fig. 3.19: Calculated vertical section close to the (Mg$_2$Ca) - (Al$_2$Ca) section with slightly less calcium; dotted lines are calculated with the parameters of [2007Cao]. Superimposed are the experimental data from [2006Suz]; DTA signals of the sample at 32.5 wt.% Al are taken from [2003Gro].

43.7 wt.% Al.

Only the experimental phase assembly at 500 °C and 20 wt.% Al 'C14 + C36' is not met, the calculation predicts C14 with tiny amounts of (Mg). The revised model represents especially the thermal signals at ~ 820 °C significantly better than the preliminary data set [2007Cao]. The strong thermal signal seen in sample #1 (11 wt.% Al) at 720 °C is not only in perfect accord with the liquidus line of C14; its shape, indicating an almost invariant reaction is also supported by the calculated narrow freezing range of this alloy with 95% of the liquid phase solidifying in a very small temperature interval of less than 5 K.

3.2.5 Conclusion

- For the thermodynamic description presented in this work all available experimental data in the Mg-Al-Ca system were considered.
- The precise description of [2007Cao] for the Mg-rich corner was only marginally changed but was extended to higher Al- and Ca contents.
- Thus a **quantitative** description is given for a wide area of the Mg-Al-Ca system, reproducing the primary precipitates, the extensive and important ternary solubilities of the binary phases and the DTA and DSC signals both in the Mg- rich corner and at the calculated vertical section C14 – C15. The solidification paths derived from the micrographs are reproduced for most of the samples. The Ca-rich region is less well supported by experimental data; however the thermodynamic extrapolation includes the available information i.e. the ternary solubility of Al$_3$Ca$_8$.

3.3 The ternary subsystem Mg-Al-Sr

The addition of Sr helps to improve the properties of AZ and AM - series magnesium alloys at elevated temparatures. Luo [2004Luo] has discussed the potential of these alloys and showed first promising results on the high temperature strength of AJ series alloys. Baril et al. [2003Bar] studied creep resistance, mechanical properties and microstructure of magnesium alloys with less than 7 wt.% Al and 3 wt.% Sr. They report good creep resistance and excellent castability for such alloys, showing a microstructure consisting of a lamellar phase Al_4Sr at the grain boundaries of primary magnesium, (Mg). For higher Sr/Al ratio, a ternary phase is reported [2003Pek]. Formation of the $\gamma(Al_{12}Mg_{17})$-phase is only observed at lower Sr/Al ratio. The microstructure evolution of a Mg-5Al-2Sr (wt.%) alloy during semisolid molding was studied by Czerwinski and Zielinska-Lipiec [2005Cze].

These studies on promising applications emphasize the need for a precise thermodynamic description of the phase diagram of the ternary system Mg-Al-Sr. This is an important basis for a purposeful alloy development, enabling solidification calculations and the understanding of microstructures of promising alloys for various applications. The first thermodynamic calculation of the ternary system by Chartrand and Pelton [1994Cha] was limited to an extrapolation from the binary subsystems. The early experimental work of Makhmudov et al. [1980Mak] - [1982Mak2] will be discussed in detail below. Numerous samples in the entire Mg-Al-Sr system were recently investigated by Parvez et al. [2005Par] using DSC, XRD and metallography. The original experimental data of [2005Par] are critical re-assessed in the present work in cooperation with that group and was actually used for preliminary thermodynamic calculations in order to select the key samples studied here. The results of a recent study on the Mg-rich corner of the Mg-Al-Sr system by Cao et al. [2006Cao] are also implemented in this work. The purpose of this work is to generate a comprehensive and consistent thermodynamic description of the phase equilibria based on the new experimental data obtained in this work together with the bulk of, partly re-assessed, experimental literature data.

3.3.1 Experimental data from the literature

The early experimental information of the ternary Mg-Al-Sr system is from several publications of the group of Makhmudov and coworkers from Dushanbe, Tajikistan [1980Mak, 1981Mak1 , 1981Mak2 , 1982Mak1 , 1982Mak2]. Although these papers on the ternary Mg-Al-Sr system all originate from the same group, several discrepancies can be observed.

The first paper [1980Mak] reports solubility limits at 400 °C for Mg-rich and Al-rich alloys derived by measurement of the variation of lattice parameter and microhardness with composition and metallographic identification of the phases. Alloys were synthesized in a resistance furnace in corundum crucible in an atmosphere of helium. Homogenization was performed in silica ampoules at 400 °C during 240 h. A ternary compound „X“ in equilibrium with $Mg_{17}Sr_2$, γ and (Mg) was assumed by [1980Mak], but not confirmed in [1981Mak2]. Discrepancies between these two papers also concern the (Al) + Al_4Sr two-phase region and ternary solubilities in the binary Mg-Sr and Al-Sr compounds. No comment is made by [1981Mak2] on these discrepancies. Partial liquidus surfaces of the Mg- and Al-corners were reported by [1981Mak1] using differential thermal, microstructural and X-ray diffraction analysis and microhardness measurements. Two ternary eutectics were found, corresponding to E_2 and U_7 in the present notation.

The isothermal section at 400 °C, investigated by X-ray diffraction and microhardness measurements, is given by [1981Mak2]. Large ternary solubilities of the binary phases were observed and confirmed by the variation of the lattice parameters. A ternary compound S in the Sr-rich corner, approximating to Al_6MgSr_{10}, was detected by [1982Mak2]. Since its crystal structure has not been determined, the possibility of it being a ternary solubility of Mg in an Al_2Sr_3 phase was mentioned; that phase, Al_2Sr_3 is, however, not accepted as stable compound in the binary Al-Sr. [1982Mak1] examined the sections γ - $Mg_{17}Sr_2$, β - $Mg_{17}Sr_2$, Mg_2Sr - Al_4Sr, $Mg_{17}Sr_2$ - Al_4Sr and β - Al_4Sr by DTA, X-ray diffraction analysis, metallography and microhardness measurements. They *assumed* all sections to be pseudobinary eutectic systems. The solubility limits at 300 ° and 400 °C were determined after annealing alloys for 300 hours and water quenching. These solubilities do not agree with the 400 °C isothermal section given by [1981Mak2] because these vertical sections are not aligned with all the tie-line directions and, thus, they are not „pseudobinary systems“. Liquidus temperatures of 26 ternary alloys investigated by DTA were reported in [1982Mak2]. For Sr-rich alloys the temperatures and liquid compositions of six invariant reactions were given in the Sr-Mg_2Sr-Al_4Sr partial ternary system. Unfortunately [1982Mak2] did not tabulate the results of the DTA experiments. Again a ternary phase S in the Sr-rich region was reported.

A critical evaluation and thermodynamic calculation of the related binary subsystems was given by [1994Cha]. The ternary literature was mentioned, but the ternary phase diagram was only extrapolated from binary data using the quasi-chemical model for the liquid phase. The key feature of this ternary system, that is the formation of substantial ternary solid solutions or compounds, was not taken into account. The calculated phase equilibria and triangulation of the ternary system does not follow those determined experimentally by Makhmudov et al. [1980Mak] - [1982Mak2].

In one of the commercial Mg-Al-Sr alloys, AJ52x, investigated by Baril et al. [2003Bar] precipitates were found and claimed to be a ternary phase with unclear stoichiometry, tentatively named $Al_3Mg_{13}Sr$ or Mg68.3-Al17-Sr14.7 (wt.%).

More recent experimental results are presented by Parvez et al. [2005Par]. These data are carefully re-evaluated in cooperation with that group, based on the complete raw experimental information, and included in the present work. Part of these data required a substantial re-interpretation as detailed later.

In an investigation of phase equilibria in the Mg-rich corner the results of five samples are presented by Cao et al. [2006Cao]. Information was given on the primary phases observed and on the results of three samples annealed at 400 ° C and investigated with SEM/BSE and EPMA.

3.3.2 Experimental investigation

3.3.2.1 Sample preparation

Within this work, seven new key samples were selected on the basis of preliminary thermodynamic calculations to provide relevant missing information on the Mg-Al-Sr phase equilibria. Samples denoted as C1-C7 are the new samples prepared in Clausthal, samples 01-21 are re-assessed samples from Montreal [2005Par]. The first sample C1 should represent a commercial alloy („AJ62“) in the Mg-rich corner, the other six samples C2-C7 were placed on the section Mg65Al35 - Sr (wt.%) to investigate three-phase equilibria and the ternary solubilities of the involved phases and to get additional information like liquidus data and the primary crystallizing phase. The samples compositions are given in Table 3.6 , sample C3 was destroyed during testing. Samples were prepared from Mg granules (99.98 wt.%, Alfa, Karlsruhe, Germany), Al pieces (99.999 / 99.997 wt.%, Alfa, Karlsruhe, Germany) and Sr pieces (99.99%, Aldrich-APL, Urbana, IL). All purity designations are related to the metal basis. The weighed materials were pressed carefully to pellets which were sealed in Ta-capsules by careful electric arc welding under argon at 1 bar.

After testing the tightness of the Ta-capsules in a separate furnace, differential thermal analysis was carried out using a Setaram MHTC 96 (Setaram, Caluire, France) Differential Scanning Calorimeter (DSC). The DSC measurements were carried out with heating/cooling rates of 5 and 1 K/min in 3 repeated cycles each. The temperature range of each cycle was typically 300 to 800 ° C. A typical sample weight was about 250 mg. The overall uncertainty of DSC measurements was estimated as ±3 K for temperature determination.

After thermal analysis the samples were prepared metallographically. Care must be taken of the reactivity of the samples with oxygen which increased drastically with Sr-content. Therefore ethanol had to be used for grinding and polishing with strictly limited time. As a consequence, not all scratches in the micrographs could be removed, as will be shown later.

The microstructure was investigated with scanning electron microscopy mostly using

Table 3.6: Temperatures extracted from the DSC curves obtained by thermal analysis in the Mg-Al-Sr system for samples prepared in Clausthal and their interpretation. Invariant reactions were recognized from the peak shape.

		Thermal signal, °C			Interpretation
Nr.	Sample composition, wt.%	Heating [1]	Cooling [2]	Evaluated temperature	Calculated temperature, °C; phase boundary or **invariant reaction**
C1	Mg92Al6Sr2	610	610	610	601 L/L+(Mg)
		546 w	537 w	546	544 L+(Mg)/ L+(Mg)+ $Mg_{17}Sr_2$
		521 s	516 s	521	**527 U4**
C2	Mg58.5Al31.5Sr10	603	604	604	617 L/L+Al_4Sr
		482 w	478 s	482	488 L+Al_4Sr/ L+Al_4Sr+ (Mg)
		474 w	465 w	476	**477 U5**
		438 s	433 s	465	458 L+(Mg)+τ/(Mg)+τ
				438	**436 E4**
C4	Mg45.5Al24.5Sr30	672	668	670	665 L/L+Al_4Sr
		577 s	566	577	595 L+Al_4Sr/ L+Al_4Sr+ (Mg)
		521 w	518 s	521	**527 U4**
C5	Mg39Al21Sr40	653	651	652	652 L/L+Al_4Sr
		607 s	601 n.c.	607	649 L+Al_4Sr/ L+Al_4Sr+Al_2Sr
		577 s	575 s	577	**595 E1**
					582 Al_2Sr+$Mg_{17}Sr_2$ = Al_4Sr+ $Mg_{38}Sr_9$
C6	Mg26Al14Sr60	668	669	668	708 L/L+Al_2Sr (Mg_2Sr)
		not detec.	650 w	650	625 L+Mg_2Sr/ L+Mg_2Sr+AL_2Sr
		620 w	not detec.	620	**611 U1**
		619 s	601 s	618	
C7	Mg18.2Al9.8Sr72	634	632	633	676 L/L+Mg_2Sr
		513 s	not detec.	513	?
		480 w	482 s	480	?
		422 s	420 s	422	422 L+ Mg_2Sr/ L+ Mg_2Sr + Al_3Sr_8

w = weak and diffuse signal, s = strong and clear signal
not detec. = not detected, not cert. = not certain, ? = not assigned

back scattered electrons (SEM/BSE) and local compositions were analyzed with electron probe microanalysis (EPMA) using a CAMECA SX100 (Cameca, France).

3.3.2.2 Experimental results

The results of the DSC-analysis of the six samples of this work prepared in Clausthal are presented in Table 3.6 . The last column shows the interpretation as obtained from the present thermodynamic calculation for the individual alloys.

Microstructures of most representative samples for the ternary system are shown in Figs. 3.20(a) to 3.20(e). Phase identification was based on local chemical composition as measured by EPMA. Detailed analysis and interpretation of the solidification sequence of these microstructures will be given in the discussion section, considering also the results of the thermodynamic calculations. It is noted that the Sr-richest sample, C7, was very brittle and difficult to investigate. For the other samples with less Sr-content reasonably clear morphology could be obtained after proper preparation, as can be seen in the examples in Fig. 3.20 .

An EPMA X-ray map of the two-phase (Mg)+γ-$Mg_{17}Al_{12}$ region in sample C2, Fig. 3.20(d), is shown in Fig. 3.21 . The key finding here is the negligible Sr-solubility in *both* phases, (Mg) and γ-$Mg_{17}Al_{12}$. The measured maximum ternary solubilities from EPMA are given in the second last column of Table 3.7 . The large primary grown Al_4Sr-bars, such as the one in Fig. 3.20(d), show no variation in composition from center to edge, according to a line-scan over such a particle.

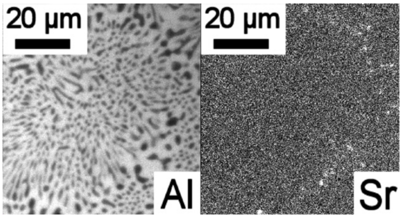

Fig. 3.21: X-ray mapping of an (Mg) + γ-$Mg_{17}Al_{12}$-region in sample C2. The left picture shows the Al-content (max. 800 counts, bright areas are γ-$Mg_{17}Al_{12}$, dark areas are (Mg)) and right picture shows the Sr-content (max. 8 counts).

The ternary phase τ was clearly identified in sample C2 (Fig. 3.20(d)) with an approximate content of ~13.5 wt.% Sr based on EPMA data, thus differing significantly from the γ-$Mg_{17}Al_{12}$ phase. The EPMA measurement of τ gives 46.5 wt.% Mg and 40 wt.% Al. This measured Mg/Al ratio of τ is, very similar to that of γ-$Mg_{17}Al_{12}$. The fact that τ is a distinct ternary phase and not the suspected ternary solubility of γ-$Mg_{17}Al_{12}$ is further

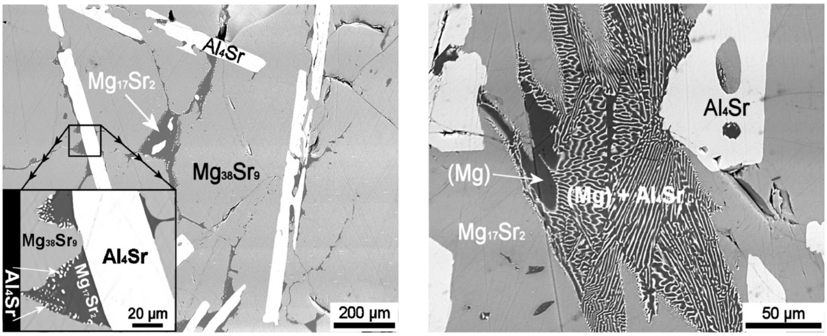

(a) Mg39Al21Sr40 (sample C5)

(b) Mg45.5Al24.5Sr30 (sample C4)

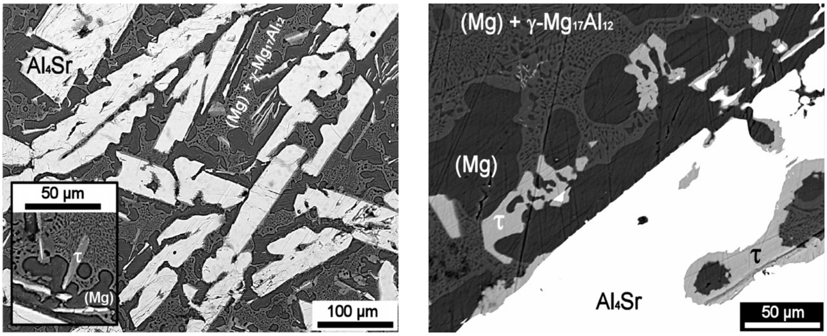

(c) Mg43.8Al33.6Sr22.6 (sample 06)

(d) Mg58.5Al31.5Sr10 (sample C2)

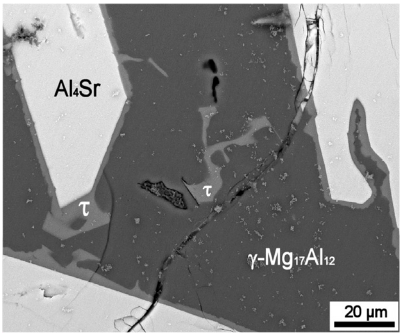

(e) Mg30Al46Sr24 (sample 08)

Fig. 3.20: Scanning electron micrographs (SEM/BSE) of five important samples, marked in Fig. 3.24 , after slow cooling in DSC. Insets show a higher magnification.

Table 3.7: All solid phases of the Mg-Al-Sr system and ternary solubilities of binary compounds.

Phase / Temperature range, °C	**Pearson symbol/ Prototype**	**Lattice parameters (pm)**	**Ref.**	**Ternary solubility, wt.%**		
				Experimental		**Calculated**
				[1981Mak2]	**[this work]**	**[this work]**
(Al) < 660	cF4 Cu	a = 404.96 pure Al at 25 ° C	[1990Mas]			
(Mg) < 650	hP2 Mg	a = 320.94 c = 521.07 pure Mg at 25 ° C	[1990Mas]			
αSr < 556	cF4 Cu	a = 608.4 pure αSr at 25 ° C	[1990Mas]			
βSr 547-777	cI2 W	a = 487 pure βSr at 614 ° C	[1990Mas]			
$Mg_{17}Sr_2$ < 605	hP38 Th_2Ni_{17}	a = 1053.0 to 1031.0 c = 1040.8 to 1019.0	[1981Mak2]	11.6 Al	16.5 Al	16.3 Al
$Mg_{38}Sr_9$ < 601	hP94 Sr_9Mg_{38}	a = 1050.0 c = 2825.1	[1994Cha]		16.8 Al	16.3 Al
$Mg_{23}Sr_6$ < 614	cF116 Th_6Mn_{23}	a = 1503 to 1463.5	[1981Mak2]	21.2 Al	15.9 Al	14.6 Al
Mg_2Sr < 713	hP12 $MgZn_2$	a = 647.5 to 635.2 c = 1043.0 to 1034.5	[1981Mak2]	6.2 Al	12.9 Al	11.5 Al
Al_4Sr < 1021	tI10 $BaAl_4$	a = 446.3 to 448.5 c = 1107.0 to 1131.0	[1981Mak2]	17.0 Mg	10.2 Mg	10.2 Mg
Al_2Sr < 922	oI12 $CeCu_2$	a = 480.2 to 480.9 b = 791.2 to 794.3 c = 796.5 to 804.0	[1981Mak2]	11.3 Mg	17.9 Mg	18.0 Mg
Al_7Sr_8 < 668	cP64 Sr_8Al_7	a = 1275.3	[1994Cha]		$\sim$ 1 Mg	nil
Al_3Sr_8 342-605	aP22 Ca_8In_3		[2004Zho]			nil
β, Al_3Mg_2 < 451	cF1832 Mg_2Al3	a = 2823.9	[1997Su]		$<$ 1 Sr	nil
ε, $Al_{30}Mg_{23}$ 250-410	hR53 $Mg_{23}Al_{30}$	a = 1282.54 c = 2174.78	[1991Vil]		$<$ 1 Sr	nil
γ, $Al_{12}Mg_{17}$ < 464	cI58 αMn	a = 1054.38	[1991Vil]		$<$ 1 Sr	nil
τ, $Al_{38}Mg_{58}Sr_4$ < 477	Not certain		[this work]			

compounded by the marked contrast in the SEM/BSE micrographs in Figs. 3.20(d) and 3.20(e), indicating a two-phase structure of $\tau + \gamma$-$Mg_{17}Al_{12}$.

All of the original experimental data from samples prepared in Montreal, including unpublished SEM and EPMA data, were used for this work. The data which were partly previously published [2005Par] were critically reassessed in detail. This included both the raw XRD-patterns as well as the raw thermal analysis DSC signal curves. The entity of this DSC data was reassessed with the objective to obtain both higher accuracy and proper information on the type of reaction. Some samples had to be dismissed due to inconsistencies between heating and cooling cycles. The results are shown in Table 3.8 , with the present interpretation from the calculation in the same format as in Table 3.6 .

Table 3.8: Temperatures extracted from the DSC curves obtained by thermal analysis in the Mg-Al-Sr system in *Montreal* and their interpretation in the present work.

Nr.	Sample composition, wt.%	Thermal signal, °C: Heating [1]	Cooling [2]	Evaluated temperature	Interpretation: Calculated temperature, °C; phase boundary or **invariant reaction**
01	Al8.0	605 s	596 s	600	601 L/L+(Mg)
	Mg88.5	530 w	-	530	544 L+(Mg)/ L+(Mg)+ $Mg_{17}Sr_2$
	Sr3.5	527 s	524 s	527	**527 U4**
04	Al27.7	-	-	not detec.	567 L/L+Al_4Sr
	Mg65.6	-	524 w	524	498 L+Al_4Sr/ L+Al_4Sr+(Mg)
	Sr6.7	476 w	475 w	476	**477 U5**
		442 s	435 w	442	**436 E4**
		-	427 s	-	?
05	Al28	653 w	652 w	653	655 L/L+Al_4Sr
	Mg52	513 s	510 s	510	500 L+Al_4Sr/ L+Al_4Sr+(Mg)
	Sr20	489 s	453 s	?	475 L+Al_4Sr+(Mg)/ Al_4Sr+(Mg)
		441 s	431 s	-	472 Al_4Sr+(Mg)/ Al_4Sr+(Mg)+τ
				436	(E4 ?)
07	Al40.1	-	661 w	661	687 L/L+Al_4Sr
	Mg46.9	501 w	-	501 ?	476 L+Al_4Sr/ L+Al_4Sr+τ
	Sr13.0	453 s	444 s	453	**460 U6**
		443 s	431 s	436	(E4 ?)
08	Al46	499 s	-	-	800 L/L+Al_4Sr
	Mg30	489 w	460 w	-	473 L+Al_4Sr/ L+Al_4Sr+τ
	Sr24	457 s	445 s	457	**460 U6**
		438 w	430 w	-	?
10	Al22.8	625w	612 s	625	625 L/L+Al_4Sr
	Mg54.4	560 s	544 s	560	581 L+Al_4Sr/ L+Al_4Sr+$Mg_{17}Sr_2$
	Sr22.8	523 s	513 s	523	**527 U4**
11	Al28	-	-	-	694 L/L+Al_4Sr
	Mg43	561 s	546 s	561	586 L+Al_4Sr/ L+Al_4Sr+ $Mg_{17}Sr_2$
	Sr29	524 s	513 s	524	**527 U4**

Continued on next page

Table 3.8 – continued from previous page

Nr.	Sample composition, wt.%	Thermal signal, °C			Interpretation
		Heating [1]	Cooling [2]	Evaluated temperature	Calculated temperature, °C; phase boundary or **invariant reaction**
13	Al22.4	677 w	672 w	672	661 L/L+Al_4Sr
	Mg41.4	-	-	-	597 L+Al_4Sr/ L+Al_4Sr+$Mg_{17}Sr_2$
	Sr36.2	597 s	583 s	597	**595 E1**
		581 s	568 s	581	**582 Al_2Sr+$Mg_{17}Sr_2$ = Al_4Sr+ $Mg_{38}Sr_9$**
14	Al29.4	-	-	-	746 L/L+Al_4Sr
	Mg30.7	605 s	599 s	605	594 L+Al_4Sr/ Al_4Sr+$Mg_{17}Sr_2$+Al_2Sr
	Sr39.9	579 s	570 s	579	**582 Al_2Sr+$Mg_{17}Sr_2$ = Al_4Sr+ $Mg_{38}Sr_9$**
15	Al50.5	492 ?	662	662 ?	703 L/L+Al_4Sr
	Mg40	-	458 w	?	463 L+Al_4Sr/ L+Al_4Sr+γ
	Sr9.5	459 s	448 s	454	450 L+Al_4Sr+γ/ Al_4Sr+γ
16	Al59	670 w	670 w	670	748 L/L+Al_4Sr
	Mg30	453 s	441 s	446	447 L+Al_4Sr/ Al_4Sr+$\gamma + \beta$
	Sr11	-	-	-	410 Al_4Sr+$\gamma + \beta$/ Al_4Sr+$\gamma + \beta + \varepsilon$
18	Al63.8	-	600 ?	-	674 L/L+Al_4Sr
	Mg31.6	472 w	444 w	460	451 L+Al_4Sr/ L+Al_4Sr+β
	Sr4.6	452 s	442 s	452	**450 E2**
19	Al87.2	-	-	-	614 L/L+Al_4Sr
	Mg10.8	607 s	597 s	602	598 L+Al_4Sr/ L+Al_4Sr+(Al)
	Sr2.0	-	-	-	490 L+Al_4Sr+(Al)/Al_4Sr+(Al)
		455 s	442 s	455	(U7 ?)
20	Al62	-	-	-	872 L/L+Al_4Sr
	Mg15	505 w	497 w	-	?
	Sr23	476 w	-	476	476 L+Al_4Sr/ L+Al_4Sr+(Al)
		454 s	440 s	454	**450 E2**
21	Al8.0	-	-	-	599 L/L+$Mg_{17}Sr_2$
	Mg70.5	584 s	572 s	575	573 L+$Mg_{17}Sr_2$/ L+$Mg_{17}Sr_2$+(Mg)
	Sr21.5	564 s	557 s	561	560 L+$Mg_{17}Sr_2$+(Mg)/ $Mg_{17}Sr_2$+(Mg)

w = weak and diffuse signal, s = strong and clear signal
not detec. = not detected, n. c. = not certain, ? = not assigned
Invariant reactions were recognized from the peak shape.
[1]onset for invariant reactions, peak maximum otherwise [2]onset

Information on all solid phases of the Mg-Al-Sr system is compiled in Table 3.7 . The crystallographic data are from the literature. The ternary solubilities determined in this work by experiment and/or calculations are compared with the experimental data of [1981Mak2]. Large solubilities of the third component up to 18 wt.% are observed in nearly all Sr-containing binary phases. The ternary phase τ found in this work is given with its approximated atomic composition, $Al_{38}Mg_{58}Sr_4$.

Reassessment of the XRD phase analysis data partly published in [2005Par] was done comparing the entity of raw XRD-patterns with calculated spectra obtained using the software PowderCell 2.4 [PowderCell]. It was possible to reproduce nearly all of the peaks in the XRD-patterns by adjusting the lattice parameters of the binary phases slightly, assuming extended ternary solubilities. Doing so, most of the proposed „ternary phases“[2005Par] could be explained as ternary solubilities of known binary phases. The ternary solubilities obtained during this evaluation are in qualitative agreement with the more precise information measured with EPMA, which is given in Table 3.7 . This information, together with the aggregated thermal analysis data in Tables 3.6 and 3.8 , forms the basis of the current thermodynamic modeling. The experimental information gathered from the microstructures, regarding phase formation and primary phases, had been used as an independent check as discussed in section 3.3.4 .

3.3.3 Thermodynamic modeling

The present modeling of the ternary phase equilibria is based on the published binary thermodynamic datasets of the subsystems Al-Mg [1998Lia], Al-Sr (version 1 with random solution model and including the compound Al_3Sr_8) [2004Zho] and Mg-Sr [2006Zho].

The Gibbs energy function $G_i^{0,\phi}(T) = G_i^{\phi}(T) - H_i^{SER}$ for the element i (i= Al, Mg, Sr) in the ϕ phase (ϕ = fcc (Al, αSr), bcc (βSr), hcp (Mg), and liquid) is described by the equation:

$$G_i^{0,\phi}(T) = a + b \cdot T + c \cdot T \cdot \ln T + d \cdot T^2 + e \cdot T^3 + f \cdot T^{-1} + g \cdot T^7 + h \cdot T^{-9} \qquad (3.8)$$

where H_i^{SER} is the molar enthalpy of the stable element reference (SER) at 298.15 K and 1 bar, and T is the absolute temperature. The Gibbs energy functions for Al, Mg and Sr are taken from the SGTE compilation of Dinsdale [1991Din].

The liquid, fcc (Al, αSr), bcc (βSr) and hcp (Mg) solution phases are described by the disordered substitutional solution model. For the phase ϕ the molar Gibbs energy is expressed by the following equation:

$$G^{\phi} = \sum_{i=1}^{3} x_i G_i^{0,\phi} + RT \sum_{i=1}^{3} x_i \ln x_i + {}^{E}G^{bin,\phi} + {}^{E}G^{tern,\phi} \qquad (3.9)$$

in which R is the gas constant, and $x_i$are the molar fractions of i = Al, Mg and Sr. All excess contributions originating from all the binary interactions (${}^{E}G^{bin}$) or ternary interactions (${}^{E}G^{tern}$) are:

$${}^{E}G^{bin,\phi} = \sum_{i=1}^{2} \sum_{j>i}^{3} x_i x_j \sum_{v=0}^{n} L_{ij}^{v,\phi} (x_i - x_j)^v \qquad (3.10)$$

$$ {}^{E}G^{tern,\phi} = x_1 x_2 x_3 \{ L_{123}^{0,\phi} x_1 + L_{123}^{1,\phi} x_2 + L_{123}^{2,\phi} x_3 \} \tag{3.11}$$

The ternary interaction parameters $L_{123}^{\nu,\phi}$ may be linearly temperature dependent and are optimized together with all experimental data concerning the ϕ phase. Ternary parameters were only used for the liquid phase in this system. Specifically, only one parameter $L_{123}^{1,Liquid}$ was used for an asymmetric modeling of the ternary liquid phase. The other parameters, $L_{123}^{0,Liquid}$ and $L_{123}^{2,Liquid}$ were taken as zero. Equations (2-3) without ternary parameters correspond to a Redlich-Kister/Muggianu type extrapolation from the binary sets, which was chosen for the sake of simplicity.

The six binary phases $Mg_{17}Sr_2$, $Mg_{38}Sr_9$, $Mg_{23}Sr_6$, Mg_2Sr, Al_4Sr and Al_2Sr exhibit ternary solution ranges, forming line compounds. Since all ternary solubilities extend only at constant strontium content, Sr has become the only constituent on the second sublattice of these phases. They were modeled with two sublattices and a substitutional solution on the first sublattice, such as (Al,**Mg**)$_{17}$Sr$_2$, (Al,**Mg**)$_{38}$Sr$_9$, (Al,**Mg**)$_{23}$Sr$_6$ and (**Al**,Mg)$_4$Sr. The bold symbol denotes the majority species. The phases Mg2Sr and Al2Sr were modeled as separate phases because of their different crystal structure, using (Al,**Mg**)$_2$Sr and (**Al**,Mg)$_2$Sr. The Gibbs energy of these phases (Al,Mg)$_m$Sr$_n$ (per mole of formula) is expressed in the Compound-Energy Formalism [2001Hil] by

$$ G^{\phi} = y_{Al} \cdot G_{Al:Sr}^{0,\phi} + y_{Mg} \cdot G_{Mg:Sr}^{0,\phi} + m \cdot R \cdot T (y_{Al} \cdot \ln y_{Al} + y_{Mg} \cdot \ln y_{Mg}) + y_{Al} \cdot y_{Mg} \cdot L_{Al,Mg:Sr}^{0,\phi} \tag{3.12}$$

in which y_{Al} and y_{Mg} are the site fractions of Al and Mg on the first sublattice. The parameters $L_{Al,Mg:Sr}^{0,\phi}$ describe ternary interactions essentially within the sublattice. The parameters $G_{i:Sr}^{0,\phi}$, $i =$ Al or Mg, are also called compound energies and describe interactions essentially between the sublattices. The parameters $G_{Mg:Sr}^{0,\phi}$for the stable binary Mg-Sr phases ($\phi =$ $Mg_{17}Sr_2$, $Mg_{38}Sr_9$, $Mg_{23}Sr_6$, Mg_2Sr) were taken from the binary dataset Mg-Sr [2006Zho]. For these solution phases the parameters $G_{Al:Sr}^{0,\phi}$ represent the metastable end members of the solid solutions in the binary Al-Sr system. They were given sufficiently large positive values in this work. For the stable binary Al-Sr phases (Al_4Sr and Al_2Sr) the parameters $G_{Al:Sr}^{0,\phi}$were taken from the binary dataset Al-Sr [2004Zho] and the parameters $G_{Mg:Sr}^{0,\phi}$ represent the metastable end members of the solid solutions in the binary Mg-Sr system. The ternary interaction parameters $L_{Al,Mg:Sr}^{0,\phi}$ together with the compound energy parameters of the metastable end members were optimized in the present study using mainly the experimental data obtained in this work.

The binary phases β, ε and $Al_7Sr_8$and theternary phase τ were modeled as stoichiometric compounds referred to the stable elements as given for the example of τ, $Al_{38}Mg_{58}Sr_4$:

$$ G^{\tau} = 38\, G_{Al}^{0,fcc}(T) + 58\, G_{Mg}^{0,hcp}(T) + 4\, G_{Sr}^{0,fcc}(T) \quad + A^{\tau} + B^{\tau} \cdot T \tag{3.13}$$

The parameters A^{τ} and $-B^{\tau}$ correspond to the enthalpy and entropy of formation. This Gibbs energy of formation parameter for the ternary phase τ was determined according to the observed solid state equilibria and the nonvariant reaction U_5 : L + Al_4Sr = τ + (Mg), which was measured at 476 °C.

In order to check if reasonable values are assigned to the parameters $A^{\tau}$and B^{τ}, the absolute entropy and the entropy of fusion of τ were calculated. The absolute entropy of the phase τ at 298 K is $S_{298}^{0,\tau}$= 26.92 J/K·mol-atoms, which is in a reasonable range compared with the data of the components. The negative entropy of formation, -5 J/K·mol-atoms, is also not excessively large. The entropy of fusion at the metastable congruent melting point of τ (507.4 °C) is $\Delta_{fus}S(\tau)$= 19.02 J/K·mol-atoms or 2.3 R. This is about twice as high as the values for typical fcc and hcp metals but still substantially below the values for strongly covalent elements, such as Ge or Si [1991Din]. Lower values of $\Delta_{fus}S(\tau)$ could not be obtained during parameter optimization without deteriorating the overall quality of the description.

It is noted that the corresponding entropies of formation (negative B parameters) for the metastable end members of the solution phases $(Al,\mathbf{Mg})_{38}Sr_9$ and $(Al,\mathbf{Mg})_{23}Sr_6$, i.e. $(Al)_{38}Sr_9$ and $(Al)_{23}Sr_6$, are relatively high, about 17 J/K·mol-atoms. Converting this to absolute entropies, relatively small but still acceptable values are obtained for these two metastable phases. The final parameter settings for the actually stable phases $(Al,\mathbf{Mg})_{38}Sr_9$, $(Al,\mathbf{Mg})_{23}Sr_6$ are a delicate balance resulting from the large Al-solubilities and maintaining a stable solid solution around 400 °C for these two adjacent and competing phases.

Results of the final thermodynamic modeling are summarized in the following calculated phase diagrams. The liquidus projection is shown in Fig. 3.22(a) with a detailed view of the Mg-Al-rich side in Fig. 3.22(b). The corresponding calculated invariant reactions and maxima involving the liquid phase are listed in Tables 3.9 and 3.10 , respectively, and compared with the experimental temperatures. The optimized thermodynamic parameters are given in Table 3.11 .

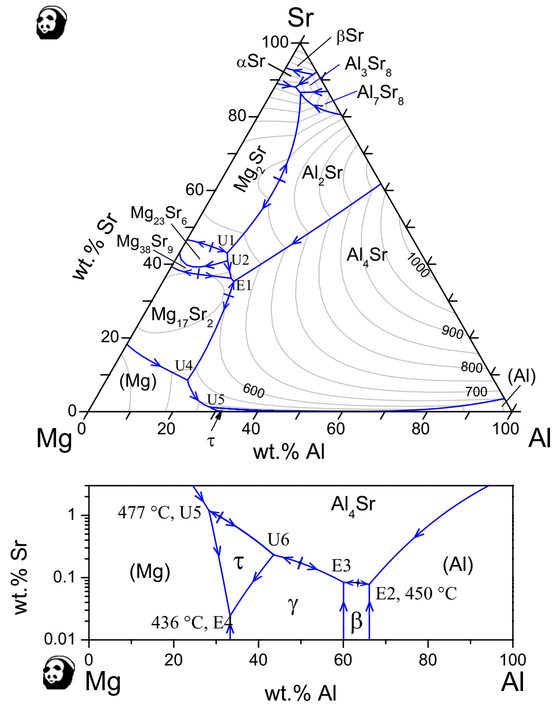

Fig. 3.22: Calculated liquidus projection of the Mg-Al-Sr system. (a) The black lines represent monovariant lines and the grey lines isotherms with an interval of 50 ° C. The data points show compositions of samples with experimentally observed primary phases including data from Refs. [2005Par, 2006Cao]. (b) Detailed view of the Mg-Al side in logarithmic presentation.

Table 3.9: Invariant four-phase reactions involving liquid phase in the ternary Mg-Al-Sr system.

Type	**T/ ° C calculated**	**Reaction**	**T/ ° C measured Clausthal**	**T/ ° C measured Montreal**	**T/ ° C [1981Mak1, 1982Mak1]**
U1	611	$L + Mg_2Sr \leftrightarrow Al_2Sr + Mg_{23}Sr_6$	619		610 ?
U2	606	$Mg_{23}Sr_6 + Al_2Sr \leftrightarrow Mg_{38}Sr_9 + L$			
U3	595.4	$L + Mg_{38}Sr_9 \leftrightarrow Mg_{17}Sr_2 + Al_2Sr$			
E1	595.3	$L \leftrightarrow Mg_{17}Sr_2 + Al_2Sr + Al_4Sr$	607	597	
D	555	$Al_3Sr_8 + \beta Sr \leftrightarrow \alpha Sr + L$			
U4	527	$L + Mg_{17}Sr_2 \leftrightarrow (Mg) + Al_4Sr$	521/519	527/524/523	
U5	477	$L + Al_4Sr \leftrightarrow \tau + (Mg)$	473	476	
U6	460	$L + Al_4Sr \leftrightarrow \tau + \gamma$		457/453	
E2	450	$L \leftrightarrow Al_4Sr + (Al) + \beta$		454/452	445
E3	449	$L \leftrightarrow Al_4Sr + \beta + \gamma$			
E4	436	$L \leftrightarrow (Mg) + \gamma + \tau$	438	442	438
U7	427	$L + Al_2Sr \leftrightarrow Mg_2Sr + Al_7Sr_8$			
U8	423	$L + Al_7Sr_8 \leftrightarrow Mg_2Sr + Al_3Sr_8$			
E5	399	$L \leftrightarrow Al_3Sr_8 + Mg_2Sr + \alpha Sr$			

Table 3.10: Invariant ternary three-phase reactions involving liquid phase in the Mg-Al-Sr system.

Type	**T/ ° C calculated**	**Reaction**
Max1	710	$L \leftrightarrow Al_2Sr + Mg_2Sr$
Max2	614	$L \leftrightarrow Mg_{23}Sr_6 + Mg_2Sr$
Max3	601	$L \leftrightarrow Mg_{17}Sr_2 + Mg_{38}Sr_9$
Max4	598	$L \leftrightarrow Al_4Sr + Mg_{17}Sr_2$
Max5	478	$L \leftrightarrow Al_4Sr + \tau$
Max6	463	$L \leftrightarrow Al_4Sr + \gamma$
Max7	452	$L \leftrightarrow Al_4Sr + \beta$

Table 3.11: Ternary thermodynamic parameters for the Mg-Al-Sr system.

Phase name	**Model**	**Parameters** in J/mol
Liquid	(Al,Mg,Sr)	$L^{0,Liquid}_{Al,Mg,Sr} = 0$
		$L^{1,Liquid}_{Al,Mg,Sr} = -25000$
		$L^{2,Liquid}_{Al,Mg,Sr} = 0$
$Mg_{17}Sr_2$	(Al,**Mg**)$_{17}$Sr$_2$	$G^{0,Mg_{17}Sr_2}_{Al:Sr} = -175000 + 50{*}T + 17{*}G^{0,fcc}_{Al} + 2{*}G^{0,fcc}_{Sr}$
		$L^{0,Mg_{17}Sr_2}_{Al,Mg:Sr} = -75400$
$Mg_{38}Sr_9$	(Al,**Mg**)$_{38}$Sr$_9$	$G^{0,Mg_{38}Sr_9}_{Al:Sr} = -1250000 + 810{*}T + 38{*}G^{0,fcc}_{Al} + 9{*}G^{0,fcc}_{Sr}$
		$L^{0,Mg_{38}Sr_9}_{Al,Mg:Sr} = -220000$
$Mg_{23}Sr_6$	(Al,**Mg**)$_{23}$Sr$_6$	$G^{0,Mg_{23}Sr_6}_{Al:Sr} = -750000 + 500{*}T + 23{*}G^{0,fcc}_{Al} + 6{*}G^{0,fcc}_{Sr}$
		$L^{0,Mg_{23}Sr_6}_{Al,Mg:Sr} = -190000$
Mg_2Sr	(Al,**Mg**)$_2$Sr	$G^{0,Mg_2Sr}_{Al:Sr} = -78600 + 19.8{*}T + 2{*}G^{0,fcc}_{Al} + G^{0,fcc}_{Sr}$
Al_4Sr	(**Al**,Mg)$_4$Sr	$G^{0,Al_4Sr}_{Mg:Sr} = -41000 + 50{*}T + 4{*}G^{0,hcp}_{Mg} + G^{0,fcc}_{Sr}$
Al_2Sr	(**Al**,Mg)$_2$Sr	$G^{0,Al_2Sr}_{Mg:Sr} = -31016 + 10{*}T + 2{*}G^{0,hcp}_{Mg} + G^{0,fcc}_{Sr}$
		$L^{0,Al_2Sr}_{Al,Mg:Sr} = +900$
τ, $Al_{38}Mg_{58}Sr_4$	$(Al)_{38}(Mg)_{58}(Sr)_4$	$G^{0,\tau}_{Al:Mg:Sr} = -1050000 + 500{*}T + 38{*}G^{0,fcc}_{Al} + 58{*}G^{0,hcp}_{Mg} + 4{*}G^{0,fcc}_{Sr}$

3.3.4 Discussion

3.3.4.1 Comparison between experimental thermal analysis and EPMA data and the thermodynamic calculations

Superimposed in Fig. 3.22(a) are all the sample compositions prepared in Clausthal (see Table 3.6) and Montreal (see Table 3.8) and the five samples of Cao et al. [2006Cao]. The good agreement between the observed primary crystallizing phases and the calculation is noted. Generally, Al_4Sr is the dominating phase in this system. For Mg-rich alloys the primary fields of (Mg) and $Mg_{17}Sr_2$ are also supported by experimental data. The solidification sequence of alloys with primary (Mg)-matrix solidification may also involve the phases τ and γ, as detailed in Fig. 3.22(b) and discussed later.

The location of the pertinent solid phases is exposed in two calculated isothermal sections, Figs. 3.23 and 3.24 . In both diagrams the substantial ternary solubilities of the binary phases are displayed with thick black lines; in Fig. 3.23 three-phase fields are highlighted in grey color. Calculated equilibria >70 wt.% Sr are not supported by ternary experimental data.

The ternary phase τ forms below 477 °C and is not present in the 500 °C section in Fig. 3.23 . Two residual liquids are stable at this temperature: one in the Sr-rich corner, the other one close to the binary eutectic L = (Mg) + γ-$Mg_{17}Al_{12}$.

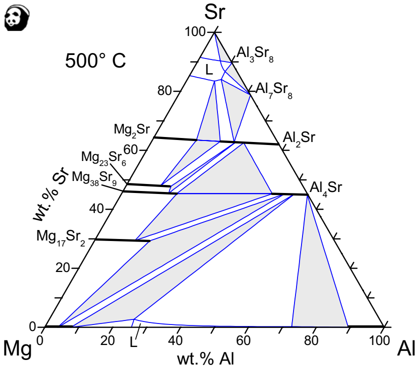

Fig. 3.23: Isothermal section calculated at 500 ° C. The grey areas indicate threephase regions. The ternary phase τ does not exist at 500 ° C.

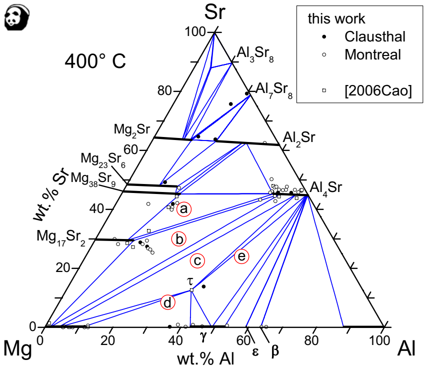

Fig. 3.24: Isothermal section calculated at 400 ° C. Small dots show room temperature EPMA data including data from Ref. [2006Cao]. The three-phase regions marked with characters (a) - (e) correspond to the micrographs in Figs. 3.20(a) - 3.20(e). Calculated equilibria >70 wt.% Sr are not supported by experimental data.

At 400 ° C in Fig. 3.24 theτ phase appears and solidification of the Mg-Al-rich liquid is complete. Superimposed on this diagram are the measured chemical compositions of the investigated phases from EPMA (this work and [2006Cao]). These data compound the modeled negligible solubility of Sr in the Mg-Al binary solid phases. The ternary solid solution range of Al_4Sr is also reasonably well supported, considering experimental difficulties with increasing Sr content. The same applies to the ternary solubility limit of $Mg_{23}Sr_6$ and $Mg_{38}Sr_9$, whereas a larger scatter is noted for the $Mg_{17}Sr_2$ phase with more data points falling into the adjacent three-phase field $Mg_{17}Sr_2$+(Mg)+Al_4Sr. Overall, the triangulation of [1981Mak2] with the dominating tie line from (Mg) to Al_4Sr is also in good agreement with the present thermodynamic calculations.

The samples C2-C7 in this work (Table 3.6) have been placed on the section Mg65Al35 - Sr. The corresponding partial vertical section up to 80 wt.% Sr is given in Fig. 3.25 (a). Superimposed are also the DSC results of samples 04 and 13 (Table 3.8), their compositions are close to this section. A good agreement of the calculation with the measured liquidus data up to 50 wt.% Sr is noted. Also the invariant reactions are well reproduced by the thermodynamic modeling, such as the peritectic formation of the τ phase at 477 ° C.

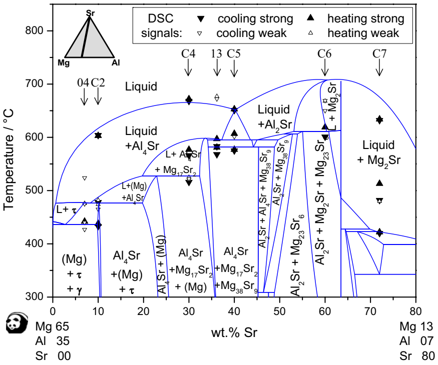

(a) From Mg65Al35 to the Sr-corner

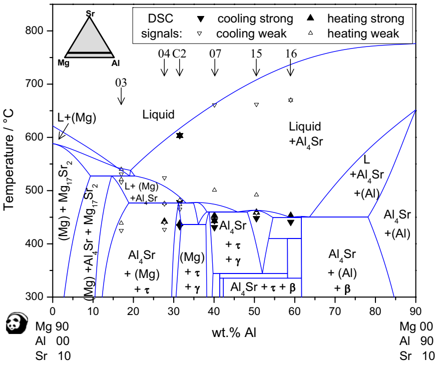

(b) At constant 10 wt% Sr

Fig. 3.25: Calculated vertical phase diagram sections compared with experimental data from DSC analysis.

The thermodynamic modeling at more than 70 wt.% Sr is only partly supported by the experimental data. The measured ternary solubilities of the binary phases, especially along the Mg_2Sr-Al_2Sr section, and the accepted Sr-Al and Sr-Mg binary descriptions essentially determine the thermodynamic calculation in the Sr-rich corner. There is not much room to shift the reaction temperatures in the calculation. This disagreement above 70 wt.% Sr might be due to the existence of a ternary phase in this Sr-rich area as mentioned in [1982Mak2]. Since the Sr-corner is not in the main focus of this work, this problem will not be further addressed.

The second vertical section presented in Fig 3.25(b) is calculated at constant 10 wt.% Sr. Superimposed are the thermal signals of 6 samples with a composition close to this section. Most of these data show good agreement between calculated and measured invariant reactions. Around 665 ° C a weak signal shows up in three samples between 40 and 60 wt.% Al. For samples 15 and 16 a deviation from the calculated liquidus line is observed. The calculated liquidus, however, is strongly fixed by the extension of the smooth Al_4Sr liquidus surface in Fig. 3.22 and the well accepted binary liquidus lines.

Since many other samples cannot be shown on such vertical sections, a comparison of the calculated results with the experimental thermal analysis data was performed for each individual alloy in Tables 3.6 and 3.8 . The result plotted in Fig. 3.26 shows a good agreement, especially for the invariant reactions. The deviating liquidus data at higher temperature are due to some artifacts in the measurement of some samples with higher Al-content, as discussed above for Fig. 3.25(b), and for those with very high Sr-content.

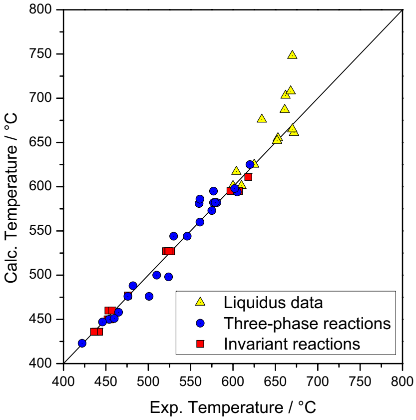

Fig. 3.26: Comparison between calculated results and all experimental thermal analysis data from Tables 3.6 and 3.8 . The straight line is a visual aid corresponding to perfect agreement between experimental values and the calculated results from the present thermodynamic model.

3.3.4.2 Microstructures evolving during slow solidification

The most important solid state three-phase-fields for Mg-Al-rich alloys in this ternary system are highlighted by characters (a) to (e) in the isothermal section given in Fig. 3.24 . On the Al-rich side the three three-phase regions are quite simple due to the tie lines merging to virtually pure binary Al_4Sr. The phase formation in the regions (a) to (e) is discussed below, using the microstructures of five representative samples after slow solidification in the DSC as given in Figs. 3.20(a) to 3.20(e). The sample compositions are approximately located at the corresponding characters in Fig. 3.24 . It is noted that the calculated phase equilibria at room temperature indicate a significant reduction of ternary solubility only for the $Mg_{17}Sr_2$ phase. Focusing on the three-phase equilibria involving the (Mg) phase, the fields (d) and (c) are also present at 25 °C, whereas the field (b) is replaced by two three-phase regions, (Mg) + $Mg_{17}Sr_2$ + $Mg_{38}Sr_9$ and (Mg) + $Mg_{38}Sr_9$ + Al_4Sr.

In Fig. 3.20(a) (sample C5) we can see the three phases Al_4Sr, $Mg_{17}Sr_2$ and $Mg_{38}Sr_9$, which are, according to the thermodynamic calculation at 400 °C, in equilibrium in field (a) of Fig. 3.24 . The shape of the large bars of Al_4Sr also supports the calculated primary precipitation. A more detailed view of the equilibrium solidification is given by the calculated phase fractions of this alloy in Fig. 3.27 . It reveals secondary solidification of the (transient) phase Al_2Sr and additional formation of $Mg_{17}Sr_2$ in the ternary eutectic E1. This $Mg_{17}Sr_2$ reacts with Al_2Sr at 582 °C in the solid state reaction U9, $Mg_{17}Sr_2$+ Al_2Sr = Al_4Sr + $Mg_{38}Sr_9$, resulting in a complete consumption of Al_2Sr and the final equilibrium phase assembly $Mg_{17}Sr_2$+ Al_4Sr + $Mg_{38}Sr_9$. It is noteworthy that this solid state transition type reaction U9 at 582 °C obviously runs to completion since no trace of unreacted Al_2Sr could be found in the microstructure. It is also interesting that the calculated phase growth of Al_4Sr is negligible in the ternary eutectic E1 but noticeable in the solid state reaction U9. This is supported by the fact that Al_4Sr also occurs as very small particles within the $Mg_{17}Sr_2$-field, shown in the magnified inset in Fig. 3.20(a).

The microstructure of sample C4, shown in Fig. 3.20(b), also displays the three equilibrium phases $Mg_{17}Sr_2$+ Al_4Sr + (Mg) at 400 °C. Again the large primary Al_4Sr-blocks are obvious. $Mg_{17}Sr_2$ is the secondary phase solidified in concave shape adjacent to these blocks. Finally, the precipitation of (Mg) + Al_4Sr in fine lamellar texture is observed, formed in the reaction U4: L + $Mg_{17}Sr_2$ = (Mg) + Al_4Sr. The entire equilibrium solidification sequence was calculated in a similar fashion as in Fig. 3.27 for this and the following samples, supporting these conclusions. It is noteworthy that again the transition type reaction runs to completion and terminates solidification in this sample. In a more rapid (non-equilibrium) solidification one should expect incomplete reaction at U4 - and also the following U5 - with residual liquid reaching the eutectic E4, see Fig. 3.22(b). That can be shown by a calculation under Scheil conditions and in this case additional phases τ and γ are expected. These phases could not be observed in the microstructure,

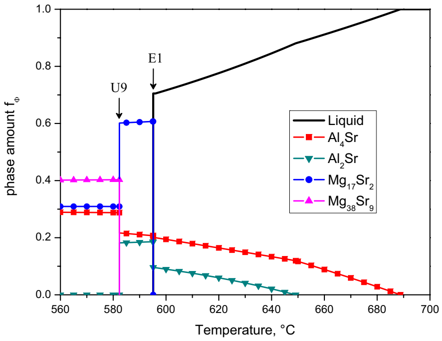

Fig. 3.27: Phase amounts (atomic fractions) calculated for solidification under equilibrium conditions for sample C5, see Fig. 3.20(a). U9 is a solid state reaction, $Mg_{17}Sr_2$ + Al_2Sr = Al_4Sr + $Mg_{38}Sr_9$.

compounding the equilibrium solidification of this sample in accord with the thermodynamic calculation, even though the thermal signals of secondary and tertiary reactions are somewhat below the calculation, see Fig. 3.25(a). Nevertheless, the actual occurrence of an invariant reaction U4 is also supported by the thermal data.

Also in sample 06 (Fig. 3.20(c)) primary Al_4Sr precipitates dominate the microstructure as large blocks. Adjacent to these blocks large fields of (Mg) were grown, which is the secondary phase in accord with the calculated monovariant reaction L = (Mg) + Al_4Sr. Solidification of this sample should terminate in equilibrium at the reaction U5 with formation of τ in a phase fraction of 20 %. This transition type reaction, L + Al_4Sr = τ + (Mg), is obviously overrun, with substantial amount of residual liquid reaching the ternary eutectic E4, where the fine lamellar structure (Mg) + γ-$Mg_{17}Al_{12}$ is produced. This eutectic structure is almost binary, considering the small Sr-content of 0.024 wt.% Sr in the liquid at E4. Taking a closer look at the BSE-image, we can see some areas of a larger grown particle, denoted as τ in the magnified inset, which is different from the lamellar eutectic structure and also brighter than the (Mg) phase. This particle is very close to the color of γ-$Mg_{17}Al_{12}$ but slightly brighter, indicating higher Sr content. This is probably the first appearance of the τ-phase, even though these particles are too small for a meaningful EPMA. The kinetics of τ formation seems to be slow, so sample 06 did not fully equilibrate compared to the thermodynamic calculations. This microstructure is in good agreement with the Scheil calculation, indicating a very small amount of τ and a substantial amount of non-equilibrium γ-$Mg_{17}Al_{12}$ phase.

Considering the chemical similarity of Sr and Ca and the reported substantial solubility of 6 at.% Ca at 400 °C in γ-$Mg_{17}Al_{12}$ [2005Suz], one might suspect that Sr dissolves similarly in γ-$Mg_{17}Al_{12}$. It is shown with sample C2 (Fig. 3.20(d)) that this suspicion is not true and, moreover, that a distinct ternary phase τ exists, which is not just a ternary solubility of Sr in γ-$Mg_{17}Al_{12}$. The solidification of this sample starts with the primary blocky Al_4Sr and the secondary growth of (Mg) next to it, so far obeying equilibrium conditions. At 477 °C all of the primary Al_4Sr should be entirely consumed in the U5 reaction, L + Al_4Sr = τ + (Mg), forming a huge amount of 78% of τ. Again, this reaction does not run to complete equilibrium, especially for the large blocks of Al_4Sr. The reaction type, however, is supported by the microstructure in Fig. 3.20(d), showing small residuals of white Al_4Sr spots enclosed by τ adjacent to (Mg). A Scheil calculation for the same alloy demonstrates that, after overrunning U5, a small amount of only 7 % of τ is formed during the monovariant eutectic reaction L = τ + (Mg), located between U5 and E4 in Fig. 3.22(b). Such a small amount of τ is quite consistent with the microstructure in Fig. 3.20(d), showing also the perfect agreement with the subsequent ternary eutectic solidification at E4, with the fine lamellar (Mg) + γ-$Mg_{17}Al_{12}$ structure and negligible amount of τ. The mass contrast produced by the back scattered electrons clearly distinguishes τ (light grey, higher Sr-content) and γ-$Mg_{17}Al_{12}$ (dark grey, lower Sr-content) as separate phases. In the large particles of τ the substantial Sr-content was quantitatively analyzed with EPMA to be ~13.5 wt.% Sr. The measured Mg/Al ratio of τ is 46.5/40 wt.%, which is very similar to that of γ-$Mg_{17}Al_{12}$. Even though the γ-$Mg_{17}Al_{12}$ phase is too finely distributed in Fig. 3.20(d) for a meaningful point analysis, its negligible Sr-solubility is demonstrated by the EPMA X-ray map of the fine lamellar two-phase (Mg)+γ-$Mg_{17}Al_{12}$ region shown in Fig. 3.21 . This compounds the negligible Sr-solubility in *both* phases, (Mg) and γ-$Mg_{17}Al_{12}$. The approximate molar composition of the ternary phase τ, $Al_{38}Mg_{58}Sr_4$, was assigned according to the EPMA data of large single phase particles; it is not related to a crystal structure, which is unknown. There is some scatter in the EPMA data of τ measured at different points; as an average value, also considering the data of [2006Cao], 12.6 wt.% Sr, 50.4 wt.% Mg and 37 wt.% Al was finally assessed. The fixed stoichiometry of τ may be a simplification.

The mass contrast distinction between the phases τ and γ-$Mg_{17}Al_{12}$ is also demonstrated in sample 08 (Fig. 3.20(e)). After the primary solidification of the Al_4Sr-bars the thermodynamic calculation indicates a secondary monovariant peritectic reaction, L + Al_4Sr = τ. This equilibrium reaction occurs over the narrow temperature range of 473 to 460 °C, producing about 36 % of τ phase while nibbling off Al_4Sr from the primary amount of 42 % down to 35 %. This peritectic reaction type is in perfect agreement with Fig. 3.20(e), showing a peripheral rim of τ around all Al_4Sr crystals. This peritectic reaction ends at U6, see also Fig. 3.22(b), where the equilibrium solidification ends in a production of a large amount of γ-$Mg_{17}Al_{12}$ and some τ. This calculation is in excellent agreement with the microstructure in Fig. 3.20(e). Only a very small amount of Al_4Sr needs to be consumed in this reaction at 460 °C, L + Al_4Sr = τ + γ, and this is probably the reason for the near-equilibrium completion of this reaction. By contrast, a Scheil calculation for that alloy predicts roaming of a residual liquid down to E4, where 7 % of (Mg) should form, in addition to the large amount of γ. A small amount of such eutectic

(Mg)-precipitates might be present in the sample, e.g. in the area between the two marks of τ; the black spots above that area in Fig. 3.20(e) are holes.

3.3.5 Conclusion

- The discrepancies in the experimental data in the ternary system Mg-Al-Sr concerning the existence of ternary phases or solubilities reported by Makhmudov et al. [1980Mak, 1981Mak1 , 1981Mak2 , 1982Mak1 , 1982Mak2] and Parvez et al. [2005Par] could be solved by investigating six key samples, combined with a more detailed evaluation of the complete raw experimental information of [2005Par].
- Substantial mutual solid solubilities of Al in binary Mg-Sr compounds and of Mg in binary Al-Sr compounds exist. The suspected Sr solubility in γ-$Mg_{17}Al_{12}$ is negligible. Only one distinct ternary phase τ, $Al_{38}Mg_{58}Sr_4$, exists.
- A consistent thermodynamic modeling of the ternary phase equilibria is generated. It is well supported by experimental data in the partial system Mg-Al-Al_2Sr-Mg_2Sr. The most complex equilibria involving the (Mg) phase are studied meticulously. The Sr-rich corner, above ≈70 wt.% Sr, is calculated for the sake of completeness. This region is not investigated in more detail in this work because of problems in sample preparation and its insignificance for Mg- or Al-based alloys.
- The evolution of microstructures during slow solidification (5 and 1 K/min) is analyzed by detailed thermodynamic calculations for five samples representing different important phase sequences. This analysis goes beyond the calculated phase diagrams and the liquidus surface. The kinetics of formation of the ternary phase τ is apparently slow; the corresponding microstructures are best understood applying non-equilibrium Scheil calculations. The formation of τ is verified both in a partly occurring four-phase transition type reaction, U5, and in a monovariant peritectic reaction, $L + Al_4Sr = \tau$. By contrast, the invariant reaction involving the Mg-richest liquid, U4, proceeds in near-equilibrium, even though it is also of the transition type. The good agreement with all of the experimental microstructures provides additional support for the thermodynamic description generated in this work.

3.4 The ternary subsystem Mg-Ca-Sr

The ternary system Mg-Ca-Sr comprises two chemically rather similar alloying elements, Ca and Sr. Even though, it will be shown that non-trivial ternary phase equilibria occur in this system. This highlights the need to study the ternary interactions in detail rather than treat these alloys as simplified Mg-(Ca+Sr) alloys.
Furthermore this ternary system could be useful for the continuing development of Al-free Mg alloys.

3.4.1 Experimental data and thermodynamic descriptions in the literature

Two publications were found in the literature on the ternary Mg-Ca-Sr system. Zhong et al. [2006Zho] stated, that no experimental data in the ternary is available, however, they did not perform any experiments. Their thermodynamic modeling for the ternary system was constructed by combining the datasets of the three binary subsystems and extrapolating to the ternary. Ideal mixing was assumed between Mg_2Ca and Mg_2Sr.

Also in the second publication by Aljarrah and Medraj [2008Alj1] no experiments were performed or found. The Authors reassessed the three binaries and prepared datasets using the modified quasichemical model (MQM). With this database and Kohler-based extrapolation for the ternary liquid phase they calculated phase diagrams presented in their paper.

Table 3.12: Temperatures extracted from the DTA curves obtained by thermal analysis in the Mg-Ca-Sr system and their interpretation. Invariant reactions were recognized from the peak shape.

Nr.	Sample composition, wt.%	Thermal signal, °C			Interpretation
		Heating [1]	Cooling [2]	Evaluated temperature	Calculated temperature, °C; phase boundary or **invariant reaction**
#1	Mg70.9Ca13.9Sr15.2	552 w	553	553	566 L/L+C14
		533 w	530 w	533	535 L+C14/ L+C14+ $Mg_{17}Sr_2$
		512 s	511 s	512	**510 E1**
#2	Mg57.8Ca3.5Sr38.7	603 s	595 w	603	?
		587 w	587 s	587	585 L/L+C14
		-	-	-	583 L+C14/ L+C14+$Mg_{38}Sr_9$
		566 w	566 w	566	**564 U2**

[1] onset for invariant reactions, peak maximum otherwise [2] onset
w = weak and diffuse signal, s = strong and clear signal, - = not detected, ? = not assigned

3.4.2 Experimental study

Two ternary samples were selected and prepared in the way described previously. Their compositions and the results of the differential thermal analysis are given in Table 3.12 . Microstructural analysis was done with SEM/BSE, local chemical compositions were identified with EPMA.

Figure 3.28 shows the microstructure of sample #1. Large plate-like particles of $Mg_{17}Sr_2$ and smaller ones of C14-Mg_2Ca can be seen. Also, a significant amount of (Mg) + C14 (+ $Mg_{17}Sr_2$) eutectic microstructure was formed in the final step of solidification. Microprobe analysis identified small ternary solubilities in C14-Mg_2Ca and $Mg_{17}Sr_2$ (> 5 wt.%), an even smaller solubility of Ca in the (Mg) phase and no Sr solubility in (Mg), analyzed in an other part of the sample with larger (Mg)-grains.

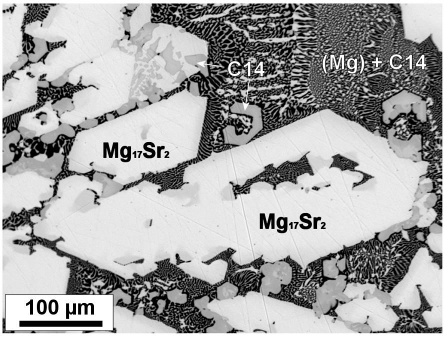

Fig. 3.28: Scanning electron micrograph (SEM/BSE) of sample #1 after slow cooling in DTA with 1K/min.

Sample #2 was placed close to the Mg-Sr binary edge. The microstructure (Fig. 3.29) shows large grains of $Mg_{38}Sr_9$ which sometimes have smaller C14-Mg_2Sr particles within them. Furthermore $Mg_{17}Sr_2$ areas and a fine $Mg_{17}Sr_2$ + C14-$Mg_2(Ca,Sr)$ microstructure are present. It is noteworthy that the C14 in the fine microstructure has a significantly higher Ca content compared to that of the C14 found inside the $Mg_{38}Sr_9$ particles. This will be discussed later in detail.

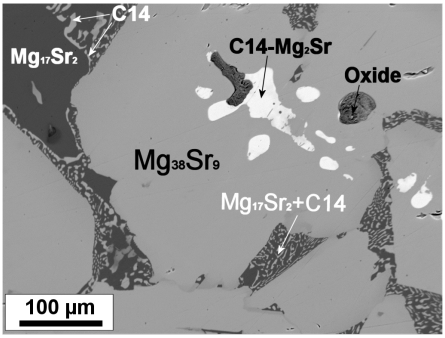

Fig. 3.29: Scanning electron micrograph (SEM/BSE) of sample #2 after slow cooling in DTA with 1K/min.

3.4.3 Thermodynamic modeling

The thermodynamic modeling of the binary edge systems remaining unchanged from the description of these subsystems in section 3.1 were used for the preliminary dataset. Based on the experimental results ternary solubilities have been introduced for the binary Mg-Sr phases $Mg_{17}Sr_2$ and $Mg_{38}Sr_9$. The Compound Energy Formalism (CEF) [2001Hil] has been adopted as described in section 2.2 on page 11 using interactions only on the second sublattice.
The Gibbs energy of these phases $(Mg)_m(Ca,Sr)_n$ (per mole of formula unit) is expressed analogue to eq. 3.12 :

$$G^{\phi} = y_{Sr} \cdot G^{0,\phi}_{Mg:Sr} + y_{Ca} \cdot G^{0,\phi}_{Mg:Ca} + n \cdot R \cdot T (y_{Sr} \cdot \ln y_{Sr} + y_{Ca} \cdot \ln y_{Ca}) + y_{Sr} \cdot y_{Ca} \cdot L^{0,\phi}_{Mg:Sr,Ca} \quad (3.14)$$

The two laves phases C14-Mg_2Ca and C14-Mg_2Sr are modeled as one phase with mutual solubility and approximately ideal solution. Not enough experimental data were available in order to justify the introduction of a ternary parameter for the liquid phase.

Results of the final thermodynamic modeling are summarized in the following calculated phase diagrams. The liquidus projection gives an overview and is shown in Fig. 3.30. The corresponding calculated invariant reactions involving the liquid phase are listed in Table 3.13 and compared with the experimental temperatures, Table 3.14 shows the compositions of the phases involved at reaction E1. In contrast to the Mg-Al-Ca and -Sr systems, there is no maximum involving the liquid phase in the Mg-Ca-Sr system. The optimized thermodynamic parameters are given in Table 3.15 .

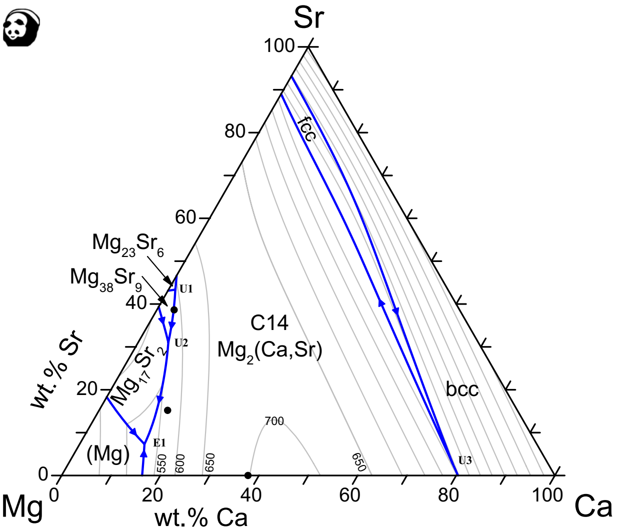

Fig. 3.30: Calculated liquidus projection of the Mg-Ca-Sr system. The round marks (●) represent the sample compositions, the grey lines represent isotherms with an interval of 50 °C.

Table 3.13: Invariant four-phase reactions involving liquid phase in the ternary Mg-Ca-Sr system.

Type	**T/ °C calculated**	**Reaction**	**T/ °C experimental**
U1	594	L + $Mg_{23}Sr_6$ ↔ C14 + $Mg_{38}Sr_9$	
U2	564	L + $Mg_{38}Sr_9$ ↔ $Mg_{17}Sr_2$ + C14	566
E1	510	L ↔ (Mg) + $Mg_{17}Sr_2$ + C14	512
U3	443	L + βSr ↔ αSr + C14	

Table 3.14: Calculated phase compositions at the ternary eutectic reaction E1 (at 510 °C) in the Mg-Ca-Sr system.

Phase	**wt.% Mg**	**wt.% Ca**	**wt.% Sr**
L	79.54	13.14	7.32
(Mg)	99.28	0.59	0.13
$Mg_{17}Sr_2$	72.40	2.61	24.99
C14	51.30	36.89	11.82

Table 3.15: Ternary thermodynamic parameters for the Mg-Ca-Sr system.

Phase name	**Model**	**Parameters** in J/mol
$Mg_{17}Sr_2$	$Mg_{17}(Ca,\mathbf{Sr})_2$	$G^{0,Mg_{17}Sr_2}_{Mg:Ca} = -73000 + 40*T + 17*G^{0,hcp}_{Mg} + 2*G^{0,fcc}_{Ca}$
$Mg_{38}Sr_9$	$Mg_{38}(Ca,\mathbf{Sr})_9$	$G^{0,Mg_{38}Sr_9}_{Mg:Ca} = -205000 + 120*T + 38*G^{0,hcp}_{Mg} + 9*G^{0,fcc}_{Ca}$

3.4.4 Discussion

The predominant primary precipitating phase in the Mg-Ca-Sr system is the C14-Mg_2(Ca,Sr). Due to the mutual solubility of Ca and Sr in this phase it reaches from the binary Mg-Ca to the Mg-Sr edge. Beside the three invariant reactions in the Mg corner (two U-type transformations and one eutectic) one further transformation reaction appears close to the Ca corner. This reaction is almost degenerated and originates from the bcc-fcc transformation of Ca and Sr, though in fact, small amounts of Liquid and C14 take part in this reaction as well. The primary precipitation observed in the microstructures of the two samples in Figs. 3.28 and 3.29 is consistent with the calculation. The complete calculated phase sequence during solidification is given in the right column of Table 3.12 .

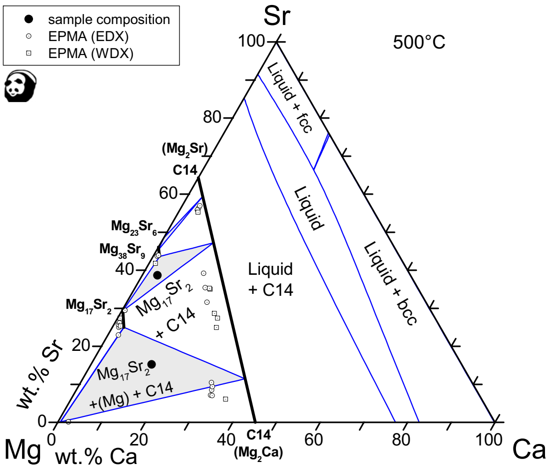

Fig. 3.31: Calculated isothermal phase diagram section at 500 ° C compared with experimental data from EPMA. The round marks (●) represent the sample compositions, the grey areas indicate threephase regions. Ternary solubilities of binary phases are highlighted with bold lines.

The calculated isothermal section at 500 ° C is presented in Fig. 3.31 . Superimposed

into this diagram are the chemical compositions of the two DTA samples as well as the EPMA results of the chemical analysis of the phases in these samples.
A substantial deviation between the measured and the calculated micro-chemical phase composition is visible for the C14 phase, suggesting a solubility of Mg in this phase in addition to the interchangeable Ca and Sr. These data are most likely caused by a shifted analysis where the Mg-Matrix was detected together with the C14 visible on the surface in the micrograph. This incident has been described in section 2.4 on page 16 .

The EPMA data points for C14 near the Mg-Ca side are from sample #1. Those in the center of the phase diagram *and* on the Mg-Sr side are from sample #2 - this occurrence of C14 over a composition range has been noticed already in the microstructure of sample #2 in Fig. 3.29 . To assist the understanding of this situation the solidification of this sample was calculated under Scheil conditions. Although this scenario may be too drastic for the quite slow solidification in DTA, we can see in Fig. 3.32 that the solidification starts with a Sr-rich C14. In the C14-particles solidified during ongoing solidification Sr is more and more substituted by Ca. This may very well explain the actually measured compositions in sample #2, ranging from 21 to 57 wt.% Sr in Fig. 3.31 . Altogether, the phases observed in the microstructures of the two samples are in full agreement with the calculated results at subsolidus temperature.

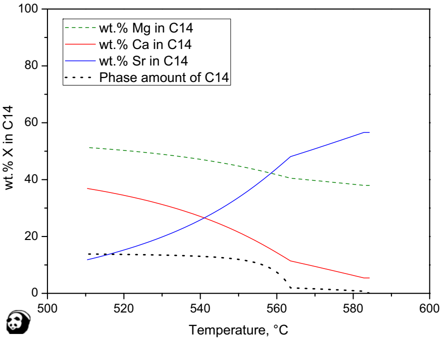

Fig. 3.32: Calculated change in composition of the C14 phase during solidification of sample #2 under Scheil conditions.

Fig. 3.33 shows a calculated vertical phase diagram section through the Mg-Ca-Sr system. This section crosses the composition of both samples, their thermal signals from DTA as listed in table 3.12 are superimposed. The calculated liquidus line in this diagram is quite flat, the thermal signal from sample #1 at 13.9 wt.% Ca suggests slightly higher temperatures. All other DTA signals of this sample are in very good agreement with the calculation, especially the eutectic at 510 ° C in the Mg-corner.

The first signal of sample #2 at 3.5 wt.% Ca can not be assigned to a reaction - it is close to the temperature of the metastable congruent melting point of $Mg_{38}Sr_9$ which is

600.2 ° C. This strong peak in the heating curve would indicate a kinetic barrier for the melting of $Mg_{38}Sr_9$. The other thermal signals are well reproduced by the calculation.

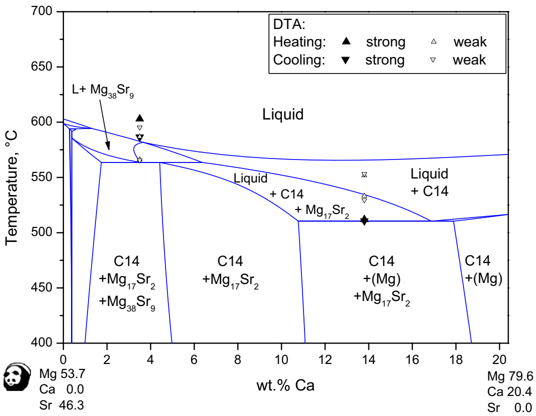

Fig. 3.33: Calculated vertical phase diagram section in the Mg-Ca-Sr system with experimental data from DTA.

3.4.5 Conclusion

- A thermodynamic dataset was developed for the Mg-Ca-Sr system, validated (in contrast to the models of [2006Zho] and [2008Alj1]) by experimental work.
- Key experiments were performed to investigate the phase equilibria in the Mg rich corner up to the C14 phase. The ternary solubilities of the binary phases were evaluated.
- It was shown that the solidification of alloys with higher Ca and Sr content is non-trivial due to the mutual solubility in the C14 phase.

3.5 The ternary subsystem Al-Ca-Sr

In the Al-Ca-Sr system the phase equilibria between the Al-Ca and the Al-Sr phases have been investigated experimentally and modeled thermodynamically. Large ternary solubilities were expected due to the similarity of Ca and Sr which results in mutual solubilities in both α-fcc and β-bcc as we saw in Fig. 3.5 on page 31 and in the Mg-Ca-Sr system in the previous section. The purpose of this work was to generate a consistent thermodynamic dataset of the phase equilibria in this system by combining experimental work and thermodynamic modeling.

3.5.1 Experimental data and thermodynamic descriptions in the literature

Only one experimental publication could be found in the literature for the ternary Al-Ca-Sr system. Zhang et al. [2001Zha] investigated six alloys on the section $Sr_{1-x}Ca_xAl_2$ ($0 \leq x \leq 1$) with XRD. They were interested in the hydrogenation behavior of these alloys but first investigated the alloys they started with. Based on the change of the lattice parameters and a significantly different crystal structure, they determined a small solubility of Ca in the Zintl phase Al_2Sr and a very large Sr-solubility in the Laves phase Al_2Ca. A narrow two phase region was found between these phases.

A thermodynamic assessment of the phase equilibria in the Al-Ca-Sr system has been presented by Aljarrah and Medraj in [2008Alj2]. They did not find any experimental work for the ternary, therefore they reviewed the binary subsystems and did a reoptimization of the binary model parameters using the modified quasichemical model. The various ternary calculations are based on an extrapolation since no experimental data were used to adjust the parameters; no ternary solubilities of the binary phases were considered in that work.

3.5.2 Experimental study

In total three sample compositions were selected on the basis of the preliminary dataset to investigate the phase equilibria and ternary solubilities of the binary phases in the Al-Ca-Sr system. Thermal analysis was performed with DTA, microstructural analysis was conducted using SEM/BSE and EPMA. Sample #2 (Al60Ca12.5Sr27.5, wt.%) was heated up to 1000 °C for 30 minutes, then cooled down to 500 °C and kept at that temperature for 20 days. The compositions of the other samples and the obtained thermal signals from DTA are presented in Table 3.16 , Table 3.17 gives an overview of the phases detected in each sample using SEM/BSE and EPMA.

Table 3.16: Temperatures extracted from the DTA curves obtained by thermal analysis in the Al-Ca-Sr system and their interpretation. Invariant reactions were recognized from the peak shape.

		Thermal signal, ° C			Interpretation
Nr.	Sample composition, wt.%	Heating [1]	Cooling [2]	Evaluated temperature	Calculated temperature, ° C; phase boundary or **invariant reaction**
#1	Al79.3Ca6.5Sr14.2	-	890 s	890	868 L/L+Al_4Sr
		620 s	618 s[a]	619	620 L+Al_4Sr/ L+Al_4Sr + (Al)
		-	-	-	**614 U2**
#3	Al49.7Ca15.7Sr34.6	965 w	965 w	965	974 L/L+C15
		955 s	950 s	953	939.0 L+C15/ L + C15+ Al_4Sr
					938.6 L + C15+ Al_4Sr/ C15+ Al_4Sr

[1] onset for invariant reactions, peak maximum otherwise [2] onset
w = weak and diffuse signal, s = strong and clear signal, - = not detected
[a] Double peak

Table 3.17: Phases detected in present samples using SEM/BSE and EPMA.

sample	**phases**
#1	Al_4Sr + Al_4Ca + (Al) {+ Al_3Ta + $Al_88Ta_8Ca_4$}
#2	(Al) + Al_4Sr + C15 + Al_7Sr_8 {+ CaO ?}
#3	Al_4Sr + C15

Sample #1 is placed within the expected equilibrium of (Al), Al_4Sr and Al_4Ca. The sample was exposed to a maximum temperature of 930 ° C for 30 minutes during the six DTA cycles. The sample was contaminated with Al-Ta phases due to the reaction with the Ta-capsule. Since the composition of the sample is close to the Al-corner, both Al_4Sr and Al_4Ca phases formed as can be seen in the micrographs (Fig. 3.34), even though the amount of Al was reduced (but not the activity a_{Al} as (Al) is still present). EPMA showed that both phases have noticeable ternary solubilities in the Ca-Sr direction. The white particles are identified as Al_3Ta. They often are surrounded by an unknown ternary phase with an approximate composition of $Al_{88}Ta_8Ca_4$. Al_4Sr formed as solid bars as already known from the investigations of the Mg-Al-Sr phase equilibria. The Al_4Ca phase formed a layer on the Al_4Sr particles and finally a eutectic microstructure with the fcc-(Al).

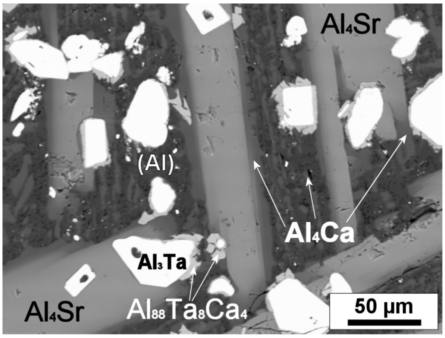

Fig. 3.34: Scanning electron micrograph (SEM/BSE) of sample #1 after slow cooling in DTA.

Fig. 3.35 shows the microstructure of sample #3 after final cooling from 980 °C with 1K/min in DTA. Obviously the mass contrast between the phases present is very small, in most cases no difference is visible. Using standard Light optical microscopy (LOM) small differences were observable. With EPMA it was possible to identify two phases with ternary solubility: Al_4Sr and $Al_2(Ca,Sr)$.

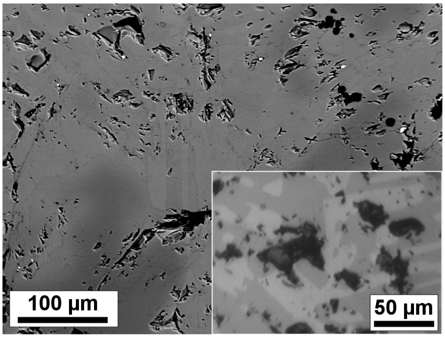

Fig. 3.35: Scanning electron micrograph (SEM/BSE) of sample #3 after slow cooling in DTA. The inset shows the microstructure with LOM.

The microstructure of sample #2 after heating at 500 °C for 20 days in a Ta-capsule is presented in Fig. 3.36 . In contrast to sample #1, the capsule has not been affected, probably due to the shorter exposure time to higher temperatures. We can see that the sample has not fully reached equilibrium since four phases can be identified: (Al), Al_4Sr, C15 and Al_7Sr_8. This order represents the increasing Sr-content in these phases. Anyhow the ternary solubilities of the binary phases measured in this sample with EPMA are used to support the solubility data for the individual phases. It was not possible to analyze the coarse structure in the lower part of the image.

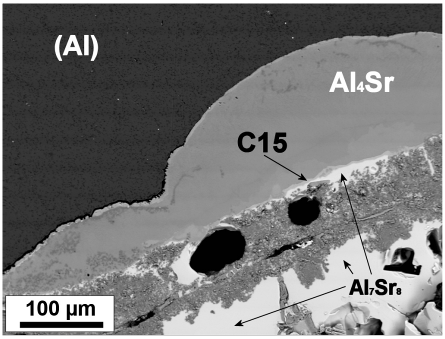

Fig. 3.36: Scanning electron micrograph (SEM/BSE) of sample #2 after heating at 500 ° C for 20 days.

3.5.3 Thermodynamic modeling

The preliminary dataset was formed out of the binary subsystems as discussed in section 3.1 ; ternary interactions were then extrapolated from these descriptions. Based on the experimental results (DTA and EPMA) presented above, ternary solubilities were introduced for the binary phases Al_4Ca, C15-Al_2Ca, Al_4Sr, Al_2Sr and Al_7Sr_8. They were modeled as line compound using the compound energy formalism as described in section 2.2 on page 11 .

The Gibbs energy G^{ϕ} for all these phases ϕ with the formula $(Al)_m(Ca,Sr)_n$ can be described with

$$G^{\phi} = y_{Ca} \cdot G^{0,\phi}_{Al:Ca} + y_{Sr} \cdot G^{0,\phi}_{Al:Sr} + n \cdot R \cdot T (y_{Ca} \cdot \ln y_{Ca} + y_{Sr} \cdot \ln y_{Sr}) + y_{Ca} \cdot y_{Sr} \cdot L^{0,\phi}_{Al:Sr,Ca} \quad (3.15)$$

Both the Al_4Ca and the Al_4Sr have the same body centered tetragonal crystal structure (Pearson symbol tI10, prototype $BaAl_4$). Therefore these two phases could be merged into one phase $Al_4(Ca,Sr)$. The results from SEM/BSE and EPMA of sample #1 however show that no mutual solubility exists between the two binary end members. A merged model for this phase would have to reproduce this demixing which is fairly complex to be realized. For the sake of simplicity it was decided to keep both phases separate.

It is not possible to merge the Laves phase C15-Al_2Ca (Pearson symbol cF24, prototype $MgCu_2$) and the Zintl phase Al_2Sr (Pearson symbol oI12, prototype $CeCu_2$), as these two phases have a different crystal structure.

No ternary parameters were introduced for the liquid phase, which is described with the Redlich-Kistler/Muggianu model.

Results of the final thermodynamic modeling are summarized in the following calculated phase diagrams. The liquidus projection gives an overview and is shown in Fig. 3.37. The corresponding calculated invariant reactions and maxima involving the liquid phase are listed in Tables 3.18 and 3.19 , respectively, and compared with the experimental temperatures. The optimized thermodynamic parameters are given in Table 3.20 .

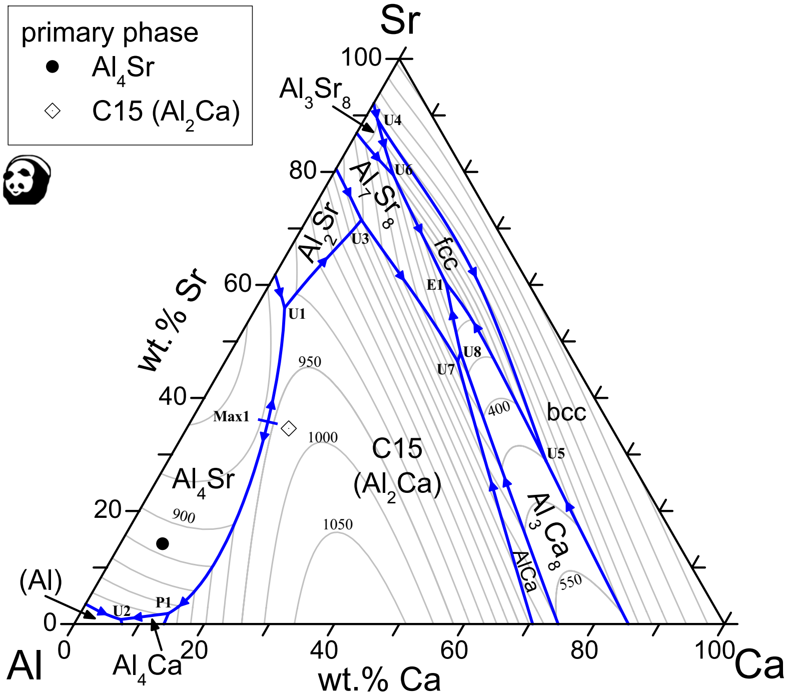

Fig. 3.37: Calculated liquidus projection of the Al-Ca-Sr system. The grey lines represent isotherms with an interval of 50 ° C.

Table 3.18: Invariant four-phase reactions involving liquid phase in the ternary Al-Ca-Sr system.

Type	**T/ ° C calculated**	**Reaction**	**T/ ° C experimental**
U1	907	L + Al_4Sr ↔ C15 + Al_2Sr	
P1	712	L + Al_4Sr + C15 ↔ Al_4Ca	
U2	614	L + Al_4Sr ↔ Al_4Ca + (Al)	(615)
U3	604	L + Al_2Sr ↔ C15 + Al_7Sr_8	
U4	554	Al_3Sr_8 + βSr ↔ αSr + L	
U5	450	L + βSr ↔ αSr + Al_3Ca_8	
U6	405	L + Al_3Sr_8 ↔ Al_7Sr_8 + αSr	
U7	300	L + C15 ↔ Al_7Sr_8 + AlCa	
U8	235	L + AlCa ↔ Al_7Sr_8 + Al_3Ca_8	
E1	235	L ↔ Al_7Sr_8 + Al_3Ca_8 + αSr	

Table 3.19: Invariant ternary three-phase reaction involving liquid phase in the Al-Ca-Sr system.

Type	**T/ ° C calculated**	**Reaction**
Max1	939	L ↔ Al_4Sr + C15

Table 3.20: Ternary thermodynamic parameters for the Al-Ca-Sr system.

Phase name	**Model**	**Parameters** in J/mol
C15	Al_2(**Ca**,Sr)	$G^{0,C15}_{Al:Sr} = -83700 + 6*T + 2*G^{0,fcc}_{Al} + G^{0,fcc}_{Sr}$
Al_4Ca	Al_4(**Ca**,Sr)	$G^{0,Al_4Ca}_{Al:Sr} = -217700 + 50*T + 4*G^{0,fcc}_{Al} + G^{0,fcc}_{Sr}$
Al_2Sr	Al_2(Ca,**Sr**)	$G^{0,Al_2Sr}_{Al:Ca} = -83468 + 18.32*T + 2*G^{0,fcc}_{Al} + G^{0,fcc}_{Ca}$
Al_4Sr	Al_4(Ca,**Sr**)	$G^{0,Al_4Sr}_{Al:Ca} = -103000 + 32*T + 4*G^{0,fcc}_{Al} + G^{0,fcc}_{Ca}$
Al_7Sr_8	Al_7(Ca,**Sr**)$_8$	$G^{0,Al_7Sr_8}_{Al:Ca} = -285000 + 0*T + 7*G^{0,fcc}_{Al} + 8*G^{0,fcc}_{Ca}$

3.5.4 Discussion

The projection of the calculated liquidus surface presented in Fig. 3.37 shows the C15-Al_2Ca phase as the predominant primary precipitate in the Al-Ca-Sr system. We can see a number of invariant reactions of the transformation type U, one ternary peritectic P and one ternary eutectic E. The latter is calculated to appear at only 235 ° C which is very low even considering the high amount of Ca and Sr in this reaction. This behaviour is caused by the limitation of the extrapolation calculation and the missing data for the ternary solubilities of the phases AlCa, Al_3Ca_8 and Al_3Sr_8. Introducing ternary solubilities to these phases in the same order of magnitude as for the other binary phases would change these Al-poor phase equilibria drastically and would shift the resulting ternary eutectic reaction to a higher temperature.

Since no experimental data are available in this range of phase equilibria, it was decided to introduce no ternary solubilities for these phases. This limitation is probably acceptable since only samples with less than 55 wt.% Al would be involved in these uncertain phase equilibria. The solidification of all other samples will run down to the (Al) corner.

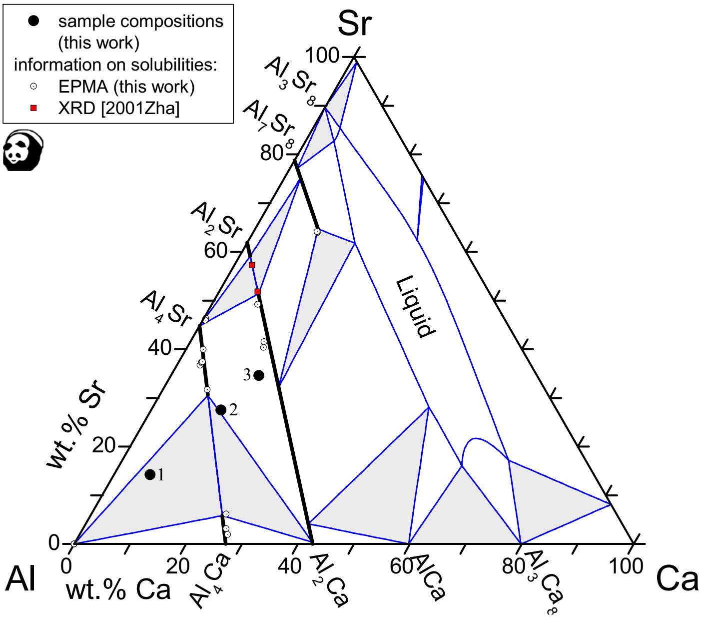

Fig. 3.38: Calculated isothermal phase diagram section in the Al-Ca-Sr system at 500 °C. Superimposed are chemical compositions of the samples and phase analysis with EPMA of this work and of XRD from [2001Zha].

The calculated isothermal phase diagram section at 500 °C is presented in Fig. 3.38 . Superimposed into this diagram are the chemical compositions of the samples and the results of the phase analysis with EPMA (this work) and by XRD from [2001Zha].

The huge ternary solubility of the C15 -Al_2Ca phase is remarkable, ending only 10 wt.% before hitting the binary Al-Sr. This incident found by Zhang et al. [2001Zha] with XRD is well supported by this works' findings with EPMA. The EPMA data for the local chemical composition of the phases alone would possibly lead to the assumption of a higher Ca-solubility in the Al_2Sr phase. With the combination of the results from XRD and EPMA the context becomes clear and approved.

Furthermore a substantial single phase field for the Al-poor liquid phase exists at 500 °C. This field also exists at this temperature for all other ternary subsystems of the Mg-Al-Ca-Sr system. Introducing ternary solubilities for the Mg-poor phases as discussed earlier would shrink the area of Liquid.

Sample #2 showed, based on the microstructure presented in Fig. 3.36 , similar behaviour to a diffusion couple. The Al_4Sr acted like an inert barrier separating the (Al) in the upper part of the figure from the Sr-rich phases in the lower part. Since the sample composition had more Ca compared to all detected phases, the coarse structure is probably CaO. The sample is totally off the equilibrium state, solely the results from microchemical analysis are used as an indication for (maximum) ternary solubilities in the particular phases. Except the ternary solubility of Al_7Sr_8 resolved this way, the calculated phase equilibria in the area Ca - Sr - Al_2Sr - C15-Al_2Ca are not supported by ternary experimental data.

In Fig. 3.39 the thermal signals from the two DTA samples are superimposed into the calculated vertical phase diagram section. A quite reasonable agreement is found for both samples lacking only in the liquidus signal of sample #3. The final phase assembly as detected for these samples in the microstructure is in good agreement with the calculation at subsolidus temperature.

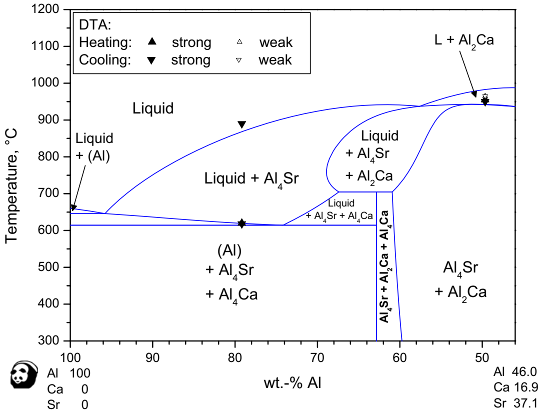

Fig. 3.39: Calculated vertical phase diagram section in the Al-Ca-Sr system. Superimposed are the thermal signals from DTA.

3.5.5 Conclusion

- A thermodynamic dataset was developed for the Al-Ca-Sr system on the basis of critically evaluated experimental data.
- It was shown that no mutual solubility exists between the two phases Al_4Ca and Al_4Sr. It is possible to merge these two phases since they have the same crystal structure. It would than be necessary to model a solid miscibility gap inbetween.
- The very large ternary solubility for the C15 -Al_2Ca phase as proposed by [2001Zha] was reproduced by the findings with EPMA.

3.6 Quaternary experimental data in the literature

Both the AJ and the AX alloy series have been discussed in previous sections 3.2 and 3.3. Mg-Al - based alloys with a combination of Ca and Sr are available on the market with labels like AXJ and AJx. Suzuki et al. [2007Suz] prepared a series of AXJ alloys by mixing commercial AX and AJ alloys. The target composition was achieved by adding pure Mg, Al and Ca. Seven alloys were investigated on the section Mg-5Al-3Ca - Mg-5Al-3Sr, substituting the Ca with Sr. Since the Mn-content in the starting alloys was already very low (<0.015 wt.%) these alloys were accepted as quaternary. They noticed a change in the observed particles: While the Ca-rich samples contained C14 and C36 particles in the Mg-matrix, the phases Mg_{17}Sr2 and Al_4Sr were observed with increasing Sr-content. Thermal analysis was performed during slow cooling (0.6 K/s) in a steel crucible.

3.7 Quaternary experimental study

Using the algorithm presented in Section 2.6 on page 18 , two additional key samples were selected to asses the accuracy of the calculated invariant five-phase reactions involving both the liquid and the (Mg) phase, and having a Mg rich overall composition. The compositions of these samples are given in Table 3.21 . The sample preparation was done as described in the previous chapters, differential thermal analysis was performed with three consecutive heating/cooling cycles with 5K/min first and than 1K/min. Sample #1 was analyzed within the temperature range of 300 to 600 °C (400 to 700 °C for sample #2).

The four-phase microstructure of sample #1 is presented in Fig. 3.40 . Two phases appear as large grains: The $Mg_{17}Sr_2$ and the C15-Al_2Ca phase. Furthermore, smaller single phase fields of (Mg), and two different fine lamellar (Mg)+X two-phase regions can be found. The brighter lamellas were identified by EDX as Al_4Sr, whereas the darker lamellas are C15. In other parts of the sample larger areas of (Mg), (Mg)+C15 and (Mg)+Al_4Sr exist than shown in Fig. 3.40 . From this microstructure it is not possible to identify clearly the primary phase, or the areas where last liquid has solidified.

Table 3.21: Temperatures extracted from the DTA curves obtained by thermal analysis in the Mg-Al-Ca-Sr system and their interpretation.

	Sample	Thermal signal, °C			Interpretation
Nr.	composition, wt.%	Heating [1]	Cooling [2]	Evaluated temperature	Calculated temperature, °C; phase boundary or **invariant reaction**
#1	Mg65.83	538 w	525 w	538	537 L/L+$Mg_{17}Sr_2$
	Al19.4	-	-	-	522 L+$Mg_{17}Sr_2$/ L+$Mg_{17}Sr_2$+Al_4Sr
	Ca5.13	505 s	501 s	505	**505 U8**
	Sr9.64	-	-	-	504 L+Al_4Sr+C15+(Mg) /Al_4Sr+C15+(Mg)
#2	Mg91.63	-	609 w	609	609 L+(Mg)
	Al4.79	517 s	524 s	519	523 L+(Mg)/ L+(Mg)+C36
	Ca3.23	-	-	-	510 L+(Mg)+C36/L+(Mg)+C36+C14
	Sr0.35	507 s	509 s	508	**508 E1**

[1] onset for invariant reactions, peak maximum otherwise [2] onset

w = weak and diffuse signal, s = strong and clear signal, - = not detected

Invariant reactions were recognized from the peak shape.

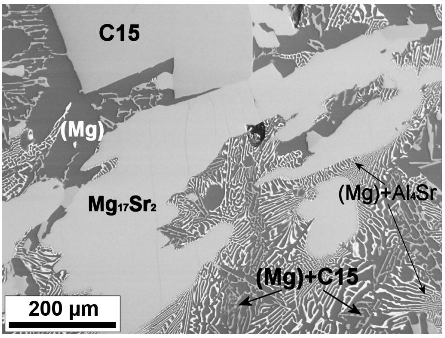

Fig. 3.40: Scanning electron micrograph (SEM/BSE) of sample #1 after slow cooling in DTA.

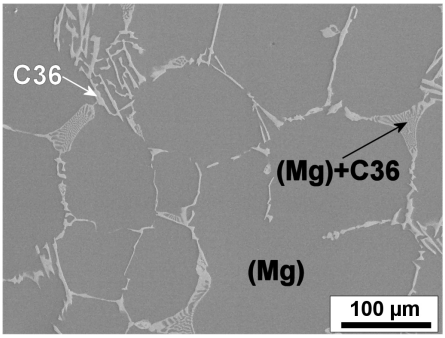

Fig. 3.41: Scanning electron micrograph (SEM/BSE) of sample #2 after slow cooling in DTA.

Fig. 3.41 shows the two-phase microstructure of sample #2, (Mg) dominates the image. Additionally C36 has grown between the (Mg) grains. Both phases together form smaller areas of a final eutectic structure.

3.8 Discussion of the Mg-Al-Ca-Sr system

3.8.1 Calculated quaternary phase relations

As discussed by [1997Kat] *true* quaternary phases are generally not to be expected in metallic systems. This has been checked and confirmed by the keysamples of this work. Therefore an extrapolation based on the four ternary subsets was used for all thermodynamic calculations.

A combination of the ternary liquidus projections from the subsystems of the Mg-Al-Ca-Sr quaternary system is presented in Fig. 3.42 . A tetrahedron comprising quaternary alloy compositions is formed by folding the three Ca-containing ternaries up, thus forming a vertex at pure Ca.
The invariant five phase reactions involving the liquid phase within this tetrahedron are listed in Table 3.22

The reaction at 445 ° C has been interpreted as degenerated since the composition of the liquid phase has only 263 ppm Sr and the Al_4Sr phase is only involved in this reaction with a phase amount of 833 ppm. The temperature of this reaction is identical to that of the E2 reaction in the Mg-Al-Ca system, see Table 3.3 on page 42 .

By the combination of the ternary liquidus surfaces in Fig. 3.42 we can get an overview of the primary precipitates in the quaternary system. A nearly symmetric area is spanned in the Mg corner where (Mg) is the primary phase. This field is in contact with 6 other

Table 3.22: All invariant five-phase reactions involving liquid phase in the quaternary Mg-Al-Ca-Sr system.

Type	**T/ $^\circ$C calculated**	**Reaction**	**T/ $^\circ$C experimental**
U1	697	$L + Al_2Sr + C15 \leftrightarrow Al_4Sr + C14$	
U2	610	$L + Al_2Sr + Mg_{23}Sr_6 \leftrightarrow C14 + Mg_{38}Sr_9$	
U3	586.4	$L + Al_2Sr + Mg_{38}Sr_9 \leftrightarrow Mg_{17}Sr_2 + C14$	
U4	585.6	$L + Al_2Sr \leftrightarrow Al_4Sr + Mg_{17}Sr_2 + C14$	
U5	561	$L + Al_4Sr + C14 \leftrightarrow C15 + Mg_{17}Sr_2$	
U6	544	$L + C15 + C14 \leftrightarrow Mg_{17}Sr_2 + C36$	
U7	512	$L + C36 \leftrightarrow Mg_{17}Sr_2 + \mathbf{(Mg)} + C15$	
E1	**508**	$L \leftrightarrow Mg_{17}Sr_2 + C14 + C36 + \mathbf{(Mg)}$	508
U8	**505**	$L + Mg_{17}Sr_2 \leftrightarrow C15 + \mathbf{(Mg)} + Al_4Sr$	505
U9	475	$L + Al_4Sr + C36 \leftrightarrow \gamma\text{-}Mg_{17}Al_{12} + C15$	
U10	474	$L + Al_2Sr + C15 \leftrightarrow C14 + Al_7Sr_8$	
U11	473	$L + C15 \leftrightarrow Al_4Sr + Al_4Ca + \gamma\text{-}Mg_{17}Al_{12}$	
U12	468	$L + Al_4Sr + C36 \leftrightarrow C15 + \tau\text{-}AlMgSr$	
U13	467.4	$L + Al_4Sr \leftrightarrow C36 + \tau\text{-}AlMgSr + \gamma\text{-}Mg_{17}Al_{12}$	
U14	466.8	$L + Al_4Sr \leftrightarrow C15 + \tau\text{-}AlMgSr + (Mg)$	
U15	465	$L + C15 \leftrightarrow C36 + \tau\text{-}AlMgSr + (Mg)$	
U16	462	$L + Al_3Sr_8 + Al_2Sr \leftrightarrow C14 + Al_7Sr_8$	
U17	454	$L + C36 \leftrightarrow \tau\text{-}AlMgSr + (Mg) + \gamma\text{-}Mg_{17}Al_{12}$	
U18	446	$L + Al_4Sr \leftrightarrow (Al) + Al_4Ca + \beta$	
D[1]	445	$Al_4Sr + \{L \leftrightarrow Al_4Ca + \beta + \gamma\text{-}Mg_{17}Al_{12}\}$	
U19	380	$L + Al_3Sr_8 \leftrightarrow C14 + Al_7Sr_8 + (Al)$	
U20	330	$L + C15 + AlCa \leftrightarrow Al_7Sr_8 + Al_3Ca_8$	
U21	318	$L + C15 \leftrightarrow C14 + Al_7Sr_8 + Al_3Ca_8$	
E2	228	$L \leftrightarrow C14 + Al_7Sr_8 + Al_3Ca_8 + \alpha Sr$	

[1] corresponds to reaction E3 in Table 3.3 on page 42

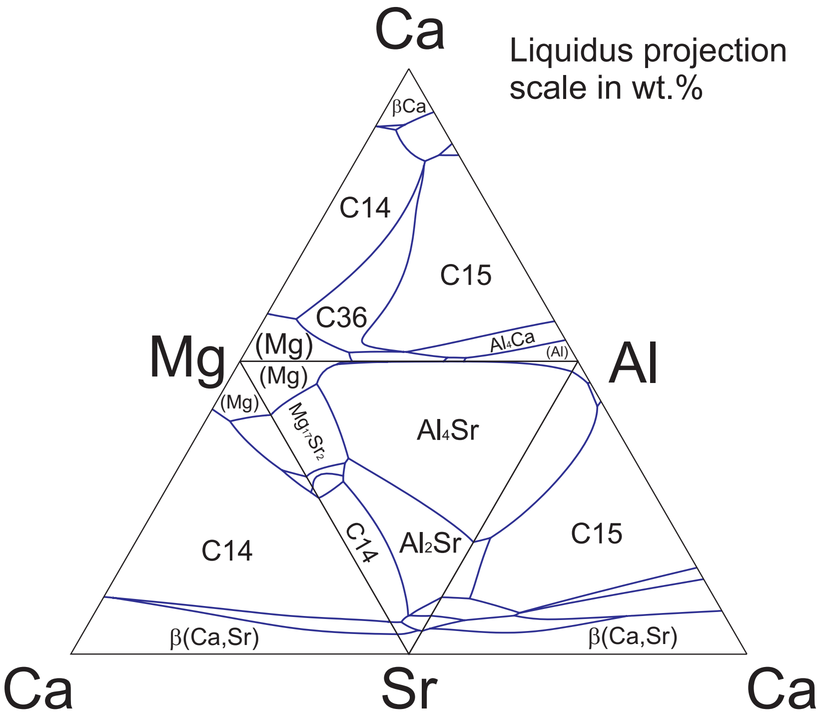

Fig. 3.42: Combination of the calculated ternary liquidus projections from the subsystems of the Mg-Al-Ca-Sr quaternary system.
A tetrahedron comprising quaternary alloy compositions is formed by folding the three Ca-containing ternaries up, thus forming a vertex at pure Ca on top.

fields of primary precipitation. Additions of Ca to Mg cause a primary precipitation of C14-Mg_2Ca while additions of Sr lead to primary precipitation of $Mg_{17}Sr_2$. Al_4Sr, τ and γ are formed by additions of Al and Ca or Sr. The C36 will precipitate first by adding a combination of Al and an increased amount of Ca.

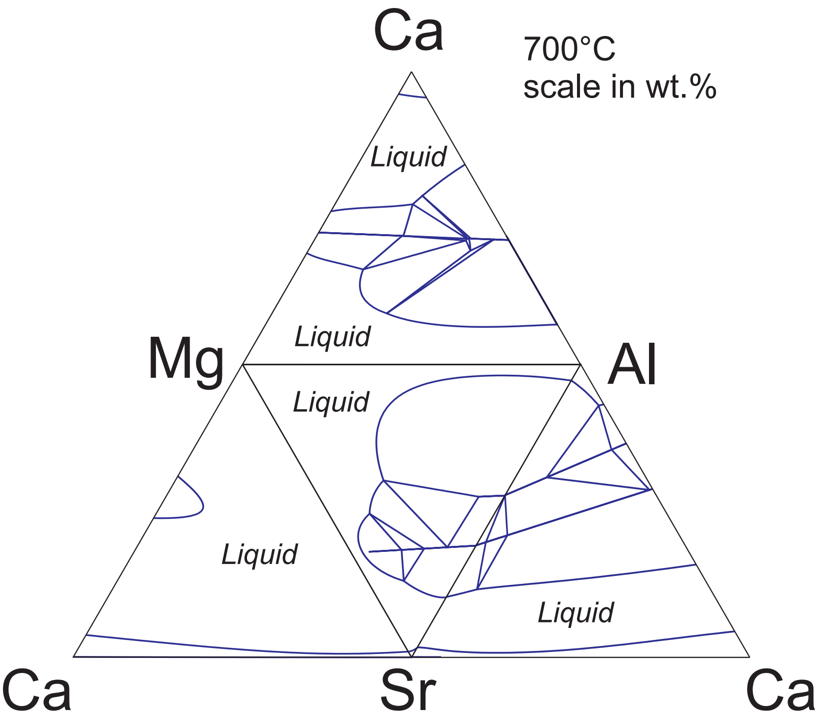

Fig. 3.43: Combination of the calculated ternary isothermal sections at 700 °C from the subsystems of the Mg-Al-Ca-Sr quaternary system.
A tetrahedron comprising quaternary alloy compositions is formed by folding the three Ca-containing ternaries up, thus forming a vertex at pure Ca on the top.

Fig. 3.43 is constructed in the same way as Fig. 3.42 by joining the 4 ternary isothermal sections at 700 °C. It provides information on the significant extension of the Mg-rich liquid phase. At 700 °C six binary solid phases are in equilibrium with this Liquid: C14, C36, C15, Al_4Sr, Al_2Sr and the distant β-(Ca,Sr) is touched due to the almost completely melted Mg-Ca-Sr system.

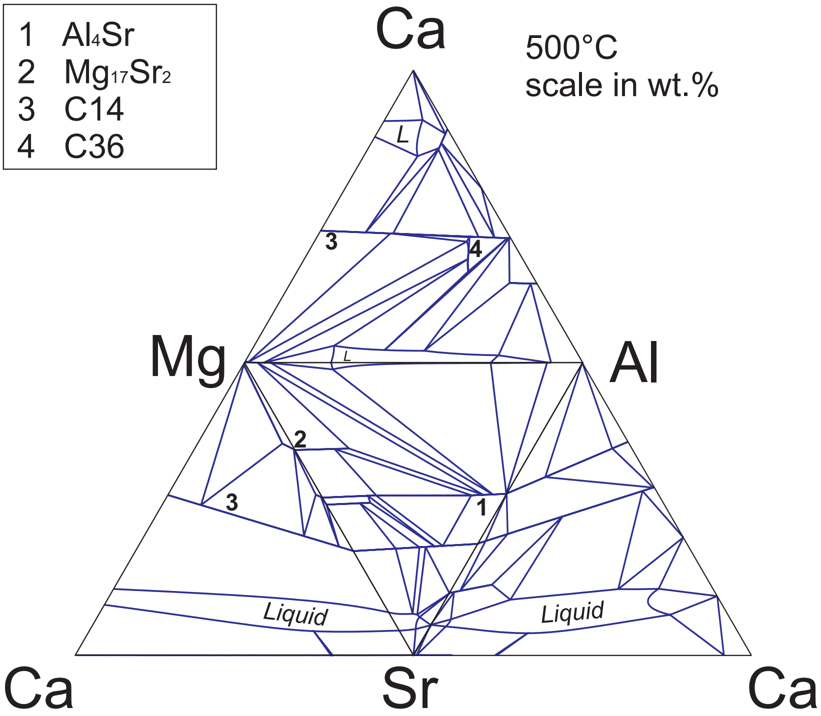

Fig. 3.44: Combination of the calculated ternary isothermal sections at 500 ° C from the subsystems of the Mg-Al-Ca-Sr quaternary system. Solid phases in equilibrium with (Mg) are labeled with numbers.

The corresponding diagram at 500 ° C is shown in Fig. 3.44 . At this temperature only four solid phases are in equilibrium with the emerged solid (Mg) phase: Al_4Sr, $Mg_{17}Sr_2$ and C14-Mg_2Ca, starting from the corresponding binary edges, and the ternary C36, which is located in the Mg-Al-Ca system. These phases are labeled in the diagram with the numbers given in the legend. It is noteworthy that a Mg-Al-rich Liquid (marked with *L*) still exists at this temperature and is in contact with the (Mg) phase field. Further liquids exist close to the Ca corner and close to each Ca-Sr binary.

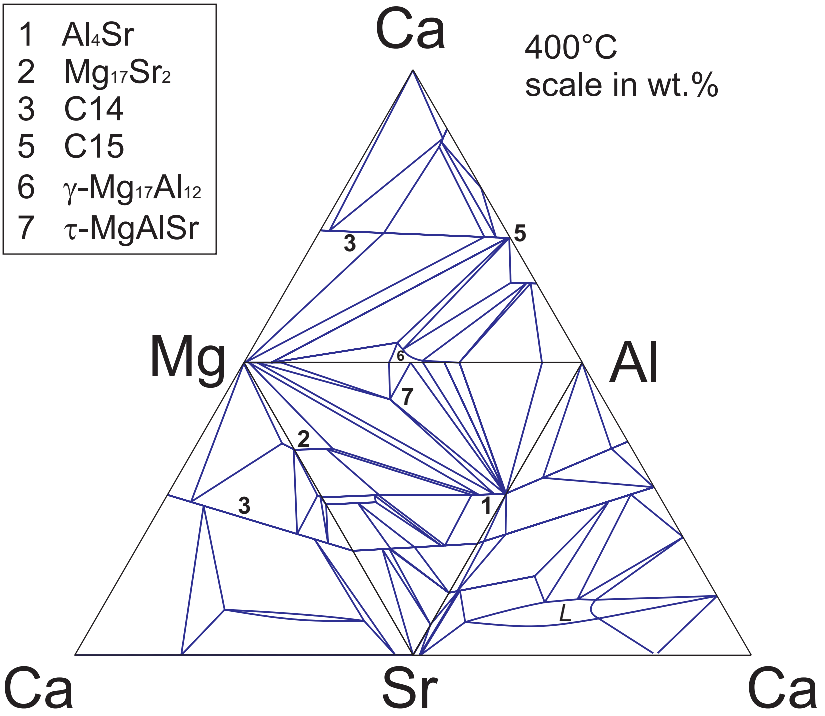

Fig. 3.45: Combination of the calculated ternary isothermal sections at 400 ° C from the subsystems of the Mg-Al-Ca-Sr quaternary system. Solid phases in equilibrium with (Mg) are labeled with numbers consistent with Fig. 3.44 .

The labeling of the phases in the next isothermal diagram at 400 ° C (Fig. 3.45) has been selected consistent with those in Fig. 3.44 . At 400 ° C the number 4 at 500 ° C, C36, is no longer stable. Its equilibrium with the (Mg) phase is replaced by the one with the C15 phase (5). The Mg-Al-rich Liquid has now solidified and brought forward two additional phases in equilibrium with (Mg): On the Ca side γ-$Mg_{17}Al_{12}$ (6) and on the Sr side the ternary phase τ-AlMgSr (7).

3.8.2 Comparison between experimental data and thermodynamic calculations

Looking at the results from DTA listed in Table 3.21 on page 93 , it is obvious that especially for sample #1 the calculated transition signals at 522 and 504 °C are missing. To evaluate the expected signal strength predicted by the calculation, the phase amounts of all phases are plotted vs. the temperature during equilibrium cooling of sample #1 in Fig. 3.46(a) and for the solidification under Scheil conditions in Fig. Fig. 3.46(b). With the information of the evolving phase amounts it becomes clear why only two significant thermal signals could have been detected with DTA: The first one corresponds to the primary precipitation of $Mg_{17}Sr_2$ at 537 °C, the second one to the abrupt solidification of about 80% of the sample while passing the U8 transformation reaction at 505 °C under equilibrium conditions. The final step of solidification was probably too weak (especially being positioned so close to the large peak of the prior reaction) to be detected. The microstructure of this sample, presented in Fig. 3.40 on page 93 , is also in reasonable agreement with this finding. All phases covered by the calculation under equilibrium conditions are present in the sample. The larger grains of C14 might have formed during the sample preparation and have never been remelted since.

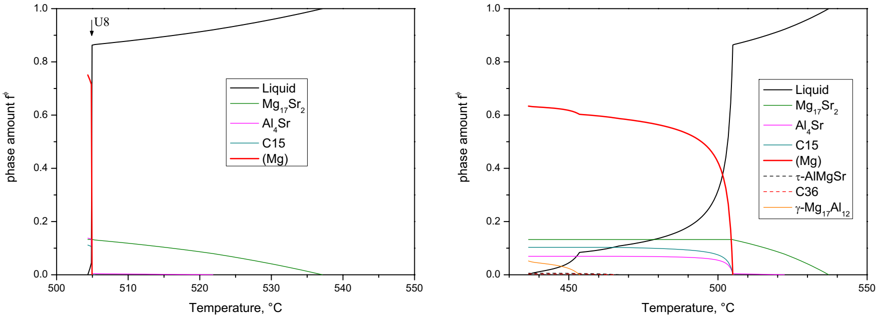

(a) Equilibrium conditions

(b) Scheil conditions

Fig. 3.46: Calculated solidification under different cooling conditions for the composition of sample #1.

For sample #2 the calculation predicted small amounts of C14 and $Mg_{17}Sr_2$. Both phases have not been identified in the microstructure given in Fig. 3.41 . Probably they are hidden in the final eutectic microstructure and are not visible due to their small amount. A similar average atomic mass of both these phases compared to C36 will give only a poor contrast in the BSE image, making the identification within the fine microstructure impossible.

The results published by Suzuki et al. in [2007Suz] from thermal analysis during slow cooling in a steel crucible (0.6 K/s) are plotted into the calculated phase diagram section in Fig. 3.47 . This phase diagram section shows the phase boundaries depending on temperature and composition along a composition line with constant 92 wt.% Mg and 5 wt.% Al, starting at a Sr-free composition and going to a Ca-free composition on the right. The thermal signals of the six virtually manganese-free samples are well reproduced by the thermodynamic calculation. (Mg) is the primary precipitate in all these alloys. It is followed by C36 for the Ca-rich alloys and by $Mg_{17}Sr_2$ for those with more Sr than Ca. These results agree with the experimental findings by Suzuki et al.. At lower temperatures up to 0.5 wt.% Sr only (Mg) and C15 are stable, furthermore additional Al_4Sr is present. C14 was detected by Suzuki et al. in the Sr free sample, which is reproduced by the thermodynamic calculations assuming Scheil conditions for the solidification. This scenario is acceptable since the cooling rate used in these TA experiments is 36 K/min and thus much higher than the 1 to 5 K/min used in DTA and DSC within this work.

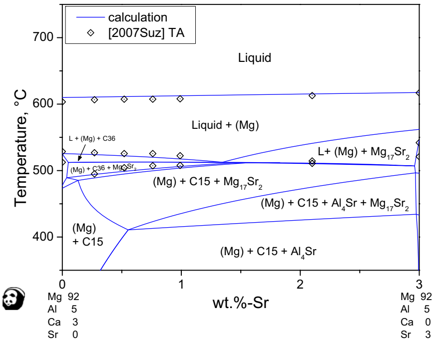

Fig. 3.47: Calculated vertical phase diagram section at Mg-Al5-Ca$(3-x)$-Sr(x) $(0 \le x \le 3$, wt.%). The results from the thermal analysis of [2007Suz] are superimposed.

3.9 Conclusion

- A consistent thermodynamic description for the quaternary Mg-Al-Ca-Sr system was extrapolated from the four ternary subsystems.
- The two important five-phase reactions E1 and U8 predicted by the calculation are exactly confirmed by key experiments.
- The experimental data proved that within the investigated range of chemical compositions no quaternary compound exists. All four component phases are binary phases with quaternary solubilities.
- The thermal signals from TA and DTA as well as the microstructure evolved during solidification are reproduced nicely by the thermodynamic calculations. The comparison contained both synthetic alloys and standard commercial. Minor discrepancies are explained by detailed thermodynamic calculations of the solidification process.

Chapter 4

The Mg-Al-Ca-Sr-Mn system

All commercial Mg-Al - based alloys contain small amounts of Mn. This is essential to improve the corrosion resistance. Free Fe is transformed into Fe-Mn-(Al) compounds and thus rendered harmless.

Adding small amounts of manganese to the Mg-Al-Ca-Sr system brings us to a more realistic approximation of *real* technical and commercial alloys.

4.1 Experimental study

To check the precision of the thermodynamic calculations in this five component system four samples have been selected for differential thermal analysis - their compositions are given in Table 4.1 .

The first two samples were machined out of commercial alloy material (MRI135 and MRI230) from Dead Sea Magnesium Ltd. (Beer Sheva, Israel). The chemical composition of these alloys was analyzed by ICP-AES from the corresponding blooms, a slight deviation of the samples composition is possible though.

The compositions of two additional samples were selected using the algorithm presented in section 2.6 on page 18 . Again only those six-phase invariant reactions were considered where the (Mg) phase takes part. The dataset used for the selection of the key sample compositions comprised the Mg-Al-Mn system as assessed by Ohno et al. [2005Ohn]. The sample MACSM#1 was selected in the center of the calculated reaction U20: L + Al_8Mn_5 ↔ (Mg) + C15 + Al_4Sr + $Al_{11}Mn_4$, sample MACSM#2 in U13: L + Al_8Mn_5 ↔ C14 + $Mg_{17}Sr_2$ + β Mn + (Mg). The samples were prepared from high purity metals in the usual experimental procedures of preparing synthetic samples. Sealing in Ta capsules was done for all four samples as described earlier (section 2.5). The manganese used in these experiments was produced by Chempur (Karlsruhe, Germany) with 0.8-3mm grain size and has a purity of 99.99 %.

Table 4.1: Temperatures extracted from the DTA curves obtained by thermal analysis in the Mg-Al-Ca-Sr-Mn system and their interpretation. Invariant reactions were recognized from the peak shape.

	Sample	Thermal signal, °C			Interpretation
Nr.	composition, wt.%	Heating [1]	Cooling [2]	Evaluated temperature	Calculated temperature, °C; phase boundary or **invariant reaction**
MRI	Mg90.53	-	-	-	642 $L/L+Al_8Mn_5$
135	Al 8.00	604 s	602 s	604	604 $L+Al_8Mn_5/L+Al_8Mn_5+(Mg)$
	Ca 1.01	506 s	504 s	506	503 $L+Al_8Mn_5+(Mg)/L+Al_8Mn_5+(Mg)+C15$
	Sr 0.24	-	-	-	493 $L+Al_8Mn_5+(Mg)+C15$
	Mn 0.22				$/L+Al_8Mn_5+(Mg)+C15+Al_4Sr$
		-	-	-	**490 U20**
		-	-	-	487 $L+(Mg)+C15+Al_4Sr+Al_{11}Mn_4$
					$/(Mg)+C15+Al_4Sr+Al_{11}Mn_4$
MRI	Mg91.92	-	-	-	634 $L/L+Al_8Mn_5$
230	Al 6.16	612 s	606 s	612	612 $L+Al_8Mn_5/L+Al_8Mn_5+(Mg)$
	Ca 1.49	522 s	522 s	522	519 $L+Al_8Mn_5+(Mg)/L+Al_8Mn_5+(Mg)+C36$
	Sr 0.21	-	-	-	511.2 $L+Al_8Mn_5+(Mg)+C36$
	Mn 0.22				$/L+Al_8Mn_5+(Mg)+C36+C15$
		-	-	-	511.0 $L+Al_8Mn_5+(Mg)+C36+C15$
					$/L+Al_8Mn_5+(Mg)+C15$
		-	-	-	505 $L+Al_8Mn_5+(Mg)+C15$
					$/Al_8Mn_5+(Mg)+C15$
M	Mg47.73	-	-	-	$L/L+Al_8Mn_5$
A	Al31.21	517 w	515 w	517	527 $L+Al_8Mn_5/L+Al_8Mn_5+Al_{11}Mn_4$
C	Ca 3.37	507	512	507	507 $L+Al_8Mn_5+Al_{11}Mn_4$
S	Sr 1.85				$/L+Al_8Mn_5+Al_{11}Mn_4+Al_4Sr$
M	Mn15.83	-	-	-	490.4 $L+Al_8Mn_5+Al_{11}Mn_4+Al_4Sr$
# 1					$/L+Al_8Mn_5+Al_{11}Mn_4+Al_4Sr+(Mg)$
		489 s	499 s	490	**490 U20**
		-	-	-	484 $L+Al_{11}Mn_4+Al_4Sr+(Mg)+C15$
					$/Al_{11}Mn_4+Al_4Sr+(Mg)+C15$
		464 w	460 s	463	?
M	Mg76.57	-	-	-	$L/L+Al_8Mn_5$
A	Al 2.36	-	521 w	521	?
C	Ca11.96	514 w	513 w	514	514 $L+Al_8Mn_5/L+Al_8Mn_5+Mg_{17}Sr_2$
S	Sr 8.31	-	-	-	512.1 $L+Al_8Mn_5+Mg_{17}Sr_2$
M	Mn 0.80				$/L+Al_8Mn_5+Mg_{17}Sr_2+(Mg)$
# 2		-	-	-	511.59 $L+Al_8Mn_5+Mg_{17}Sr_2+(Mg)$
					$/L+Al_8Mn_5+Mg_{17}Sr_2+(Mg)+C14$
		505 s	505 s	505	511.55 $L+Al_8Mn_5+Mg_{17}Sr_2+(Mg)+C14$
					$/Al_8Mn_5+Mg_{17}Sr_2+(Mg)+C14$

[1] onset for invariant reactions, peak maximum otherwise

[2] onset

w = weak and diffuse signal, s = strong and clear signal

- = not detected, ? = not assigned

U20 at 490 °C: $L + Al_8Mn_5 \leftrightarrow (Mg) + C15 + Al_4Sr + Al_{11}Mn_4$

After thermal analysis the microstructure of all four samples was investigated using back scattered electrons (SEM/BSE). Local compositions were analyzed with EDX. The results of the DTA investigation are presented in Table 4.1 . The microstructures of the four samples are shown in Figs. 4.1 to 4.4 . Phase identification based on the local chemical composition turned out to be difficult since the microstructure of some phases was very fine. In general the chemical composition of C36 and C15 are very similar. It is difficult to distinguish between these phases with EDX or even with EPMA in the multicomponent alloy systems especially when very fine microstructures evolved. More detailed investigations with TEM, out of the scope of this study, would be required for an improved phase analysis.

The microstructure of sample MRI135 is presented in Fig. 4.1 . As expected from the chemical composition large grains of (Mg) formed. Furthermore we see fine areas of lamellar microstructures (Mg) + C15 and (Mg) + Al_4Sr and in the lower left part of the image an area of (Mg) + γ-$Mg_{17}Al_{12}$.

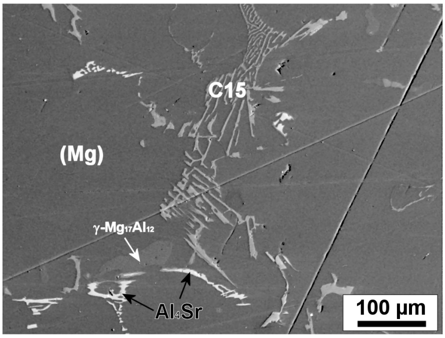

Fig. 4.1: Scanning electron micrograph (SEM/BSE) of sample MRI135 after slow cooling in DTA.

Fig. 4.2 displays the microstructure of sample MRI230. Analogous to Fig. 4.1 the large grains are (Mg). The fine black + grey lamellar regions are (Mg) + C36 (probably). As noted above, it is also possible that this phase is (in total or partly) C15. The chemical analysis of the white particles in the center of the image remained somewhat unclear as not only Al and Mn but also substantial amounts of Mg and Ca as well as some Sr were detected. Most likely these particles are Al-Mn phases and the C36/C15 identified close by is also present underneath and was analyzed too.

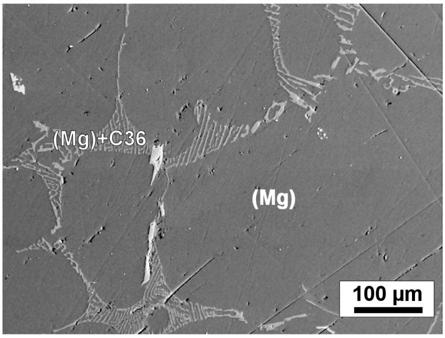

Fig. 4.2: Scanning electron micrograph (SEM/BSE) of sample MRI230 after slow cooling in DTA.

The microstructure of sample MACSM #1 (Fig. 4.3) looks significantly different to those of the standard alloys discussed so far. Large particles with an unusual shape are visible in the left part of the image. Based on the chemical micro-analysis with EDX the phase in the center is $Al_{11}Mn_4$ surrounded peritectic-like by Al_4Mn. In the top right C15 has grown on Al_4Sr needles as well as separately only in direct contact with (Mg). A fine microstructure (Mg) + Al_4Sr exists in the lower part of the figure.

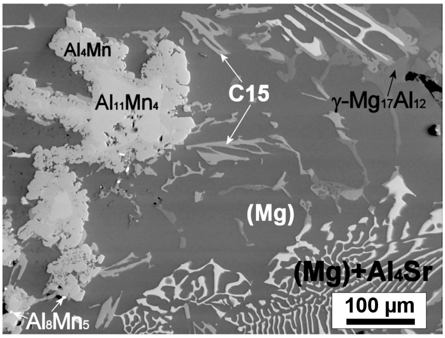

Fig. 4.3: Scanning electron micrographs (SEM/BSE) of sample MACSM #1 after slow cooling in DTA.

Fig 4.4 shows the microstructure of sample MACSM #2. Small Al_8Mn_5 particles were found in this sample as displayed in the inset on the lower right. The largest precipitates were identified as $Mg_{17}Sr_2$, close by we can see also C14. The remaining matrix is an ultrafine mixture of (Mg) and one or more other phase(s). The inset on the top left shows this structure at higher magnification. The average chemical composition of this area contained beside Mg about 10 wt.% Ca, 5-10 wt.% Sr and small amounts of Al.

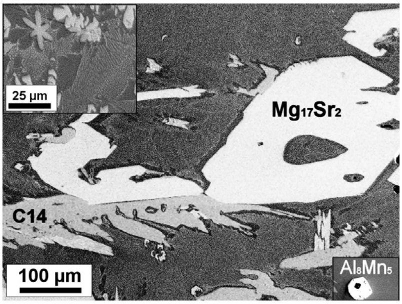

Fig. 4.4: Scanning electron micrographs (SEM/BSE) of sample MACSM #1 after slow cooling in DTA. The inset on the top left shows a higher magnification.

4.2 Thermodynamic modeling

Within the five component system Ma-Al-Ca-Sr-Mn five quaternary subsystems, ten ternary subsystems and ten binary subsystems exist. During the investigation of the Mg-Al-Ca-Sr system in chapter 3 , one quaternary, four ternaries and six binaries were discussed. This four component database was extended with the datasets for the four remaining binary systems and for one ternary system. Tables 4.2 to 4.4 list the sources of all subsets of the quinary system except the ternary Ca-Sr-Mn, which is extrapolated.

Table 4.2: Sources of the binary subsystems of the quinary Mg-Al-Ca-Sr-Mn system.

	Mg	**Al**	**Ca**	**Sr**
Al	[1998Lia]			
Ca	[1995Aga][a]	[2001Kev2][b]		
Sr	[2006Zho]	[2004Zho]	[2003Zho]	
Mn	[2005Gro]	[2007Du]	*estimation*	*estimation*

[a] slightly adjusted by [2007Koz] [b] slightly adjusted within this work

Table 4.3: Sources of the ternary Mg-X-Y subsystems of the quinary Mg-Al-Ca-Sr-Mn system.

Mg+	**Al**	**Ca**	**Sr**
Ca	[this work]		
Sr	[this work]	[this work]	
Mn	[2007Du]	*extrapolation*	*extrapolation*

Table 4.4: Sources of the ternary Mg-free Al-X-Y subsystems of the quinary Mg-Al-Ca-Sr-Mn system.

Al+	**Ca**	**Sr**
Sr	[this work]	
Mn	*extrapolation*	*extrapolation*

The important Mg-Al-Mn was recently re-assessed and modeled by Du et al. [2007Du], the results of their work including the data published previously [2005Ohn]. With these data the assessed datasets of *all* Mg-Al-X ternaries are included into this five component database, covering the major elements' interactions. All other interactions are extrapolated from the corresponding subsystems.

One can see clearly from the tables that essentially assessed information on the ternary systems including Mn, but no Al, is missing. In other words it is the combination of Mn with Ca or Sr where information is lacking. Since the Al-Mn phases in general only show very small solubilities for Ca and Sr, this limitation is acceptable.

In total 46 invariant six-phase reactions involving the liquid phase were identified in the quaternary Mg-Al-Ca-Sr-Mn system. Only those 10 where the (Mg) phase is a reactant are listed in Table 4.5 . It is interesting that none of these show a eutectic reaction type.

Table 4.5: Invariant six-phase reactions involving the liquid and the (Mg) phase in the quinary Mg-Al-Ca-Sr-Mn system.

Type	**T/ ° C calculated**	**Reaction**	**T/ ° C experimental**
U12	511.7	L + C36 $\leftrightarrow$ Al_8Mn_5 + $Mg_{17}Sr_2$ + (Mg) + C15	
U13	511.3	L + Al_8Mn_5 $\leftrightarrow$ C14 + $Mg_{17}Sr_2$ + β Mn + (Mg)	
U14	510.9	L + β Mn + α Mn $\leftrightarrow$ C14 + $Mg_{17}Sr_2$ + (Mg)	
U19	492	L + C36 + Al_8Mn_5 $\leftrightarrow$ (Mg) + C15 + $Al_{11}Mn_4$	
U20	490	L + Al_8Mn_5 $\leftrightarrow$ (Mg) + C15 + Al_4Sr + $Al_{11}Mn_4$	490
U26	467.9	L + $Al_{11}Mn_4$ + C36 $\leftrightarrow$ (Mg) + C15 + Al_4Mn	
U27	467.7	L + $Al_{11}Mn_4$ $\leftrightarrow$ (Mg) + C15 + Al_4Sr + Al_4Mn	
U29	466.8	L + Al_4Sr $\leftrightarrow$ C15 + Al_4Mn + τ-AlMgSr + (Mg)	
U30	465	L + C15 $\leftrightarrow$ (Mg) + Al_4Mn + C36 + τ-AlMgSr	
U33	454	L + C36 $\leftrightarrow$ Al_4Mn + τ-AlMgSr + γ-$Mg_{17}Al_{12}$ + (Mg)	

4.3 Discussion

4.3.1 Calculated quinary phase relations

The 2D-representation of the complete quinary system is impossible as it already was for the quaternary system. In analogy to the figures presented in section 3.8 , the projections of the ternary liquidus surfaces and the ternary isothermal sections at the given temperatures are combined in the diagrams on the following pages. All diagrams are constructed with the same arrangement of the ternary systems. In the centre of each diagram in this chapter one can find the corresponding triangular quaternary diagram of the core system Mg-Al-Ca-Sr from Figs. 3.42 to 3.45 , the additional subsystems containing Mn are added to the left and right. The only additional assessed system, Mg-Al-Mn, can be found top right.

In Fig. 4.5 , showing the combination of the projected liquidus surfaces, we can see the extended liquid miscibility gaps in all Mn containing ternary systems, especially in the Al-free ones. These miscibility gaps are already present in the Mn-(Mg, Ca, Sr) binary systems and now extended to the ternary. Since no assessment is available for most of these ternary systems, it is possible that the size of the miscibility gaps is over- or underestimated by the extrapolation. The fields of primary (Mg) are very small in the ternaries with Mn in contrast to the subsystems of the Mg-Al-Ca-Sr system.

The combination of the isothermal sections at 700 $^\circ$C is presented in Fig. 4.6 . The Mg-Al-Ca-Sr system is present in the center of the diagram showing large liquid regions. Most of the additional phase equilibria are either towards the pure αMn or towards the binary Al-Mn phases, which also have high melting points. In application to melting technology of Mg alloys it is evident that for complete melting at 700 $^\circ$C large composition ranges are available for alloying elements Al, Ca and Sr, but not for Mn.

At 500 $^\circ$C (Fig. 4.7) the phase relations are more tricky. The (Mg) solid solution range essentially exists along the Mg-Al binary with minute amounts of Ca, Sr and Mn. Most of the binary intermetallic phases are already stable forming various equilibria. The liquid phases exist only in smaller regions and in the subsystems containing Mn only in very narrow areas close to the binary edges. Most important is the Mg-Al rich liquid range.

Fig. 4.8 displays the combination of the ternary isothermal sections at 400 $^\circ$C. Only two liquid areas exist, one in the Mg-Ca-Sr system and one in the Al-Ca-Sr system close to the Ca-Sr binary edge. The (Mg) solid solution is not in equilibrium with any liquid phase. The C36 phase found in the center of the Mg-Al-Ca system at 500 $^\circ$C is no longer stable. In contrast the τ-AlMgSr phase is present in the Mg-Al-Sr system close to the Mg-Al binary edge. In the Mg-Ca-Mn system two predominant three phase areas exist: αMn + C14 + (Mg) and αMn + C14 + αCa. No phase boundary is visible in the Ca-Sr-Mn system: Due to the mutual solubility between Ca and Sr at 400 $^\circ$C as presented in Fig. 3.5 , we have a two phase regionαMn $+\alpha$(Ca,Sr) in the entire range of the phase diagram.

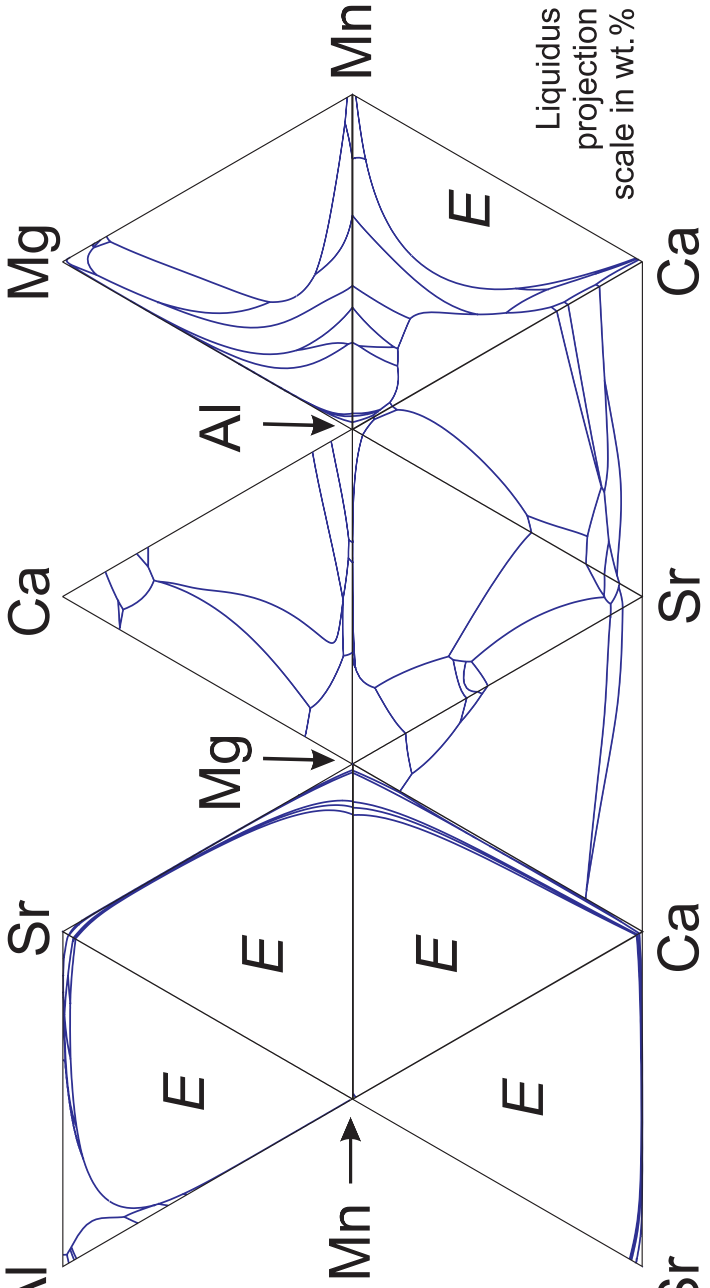

Fig. 4.5: Combination of the calculated ternary liquidus projections for all ten subsystems of the Mg-Al-Ca-Sr-Mn quinary system. The five systems denoted by *'E'* are calculated as extrapolation from the binary data, all other systems are assessed.

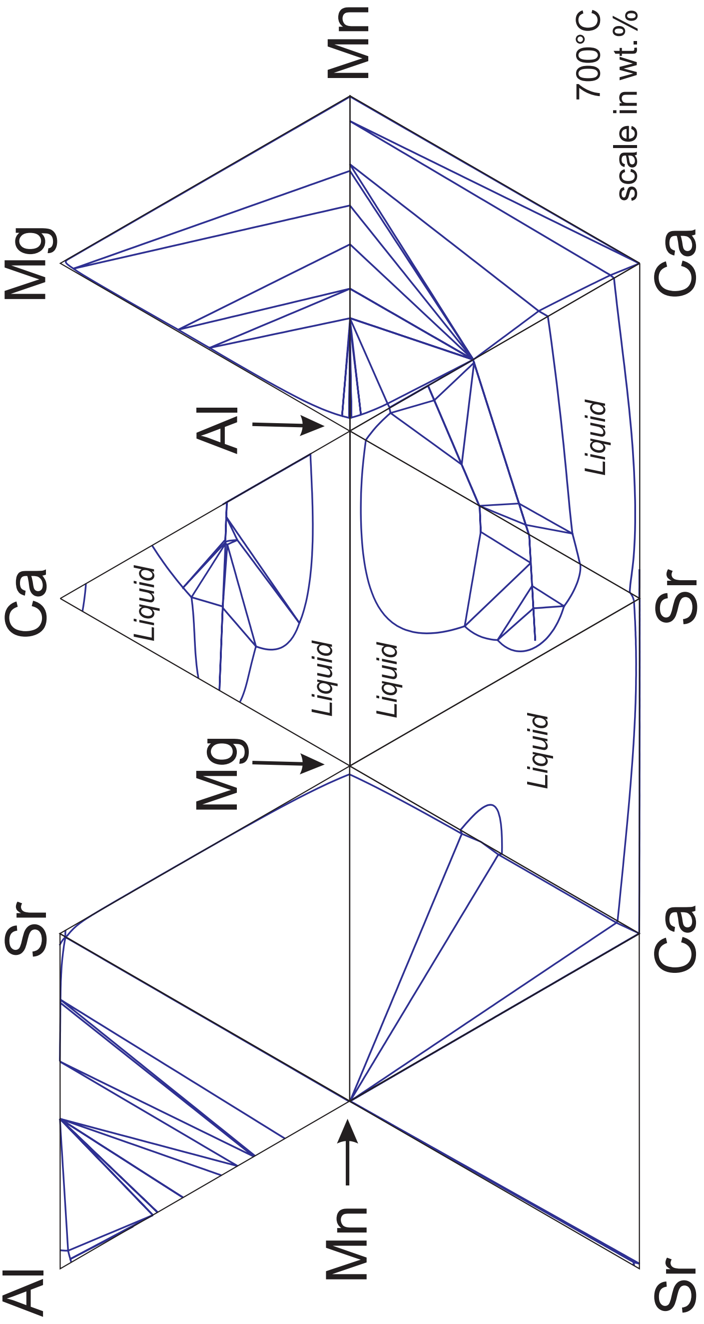

Fig. 4.6: Combination of the calculated ternary isothermal sections at 700 °C from the subsystems of the Mg-Al-Ca-Sr-Mn quinary system.

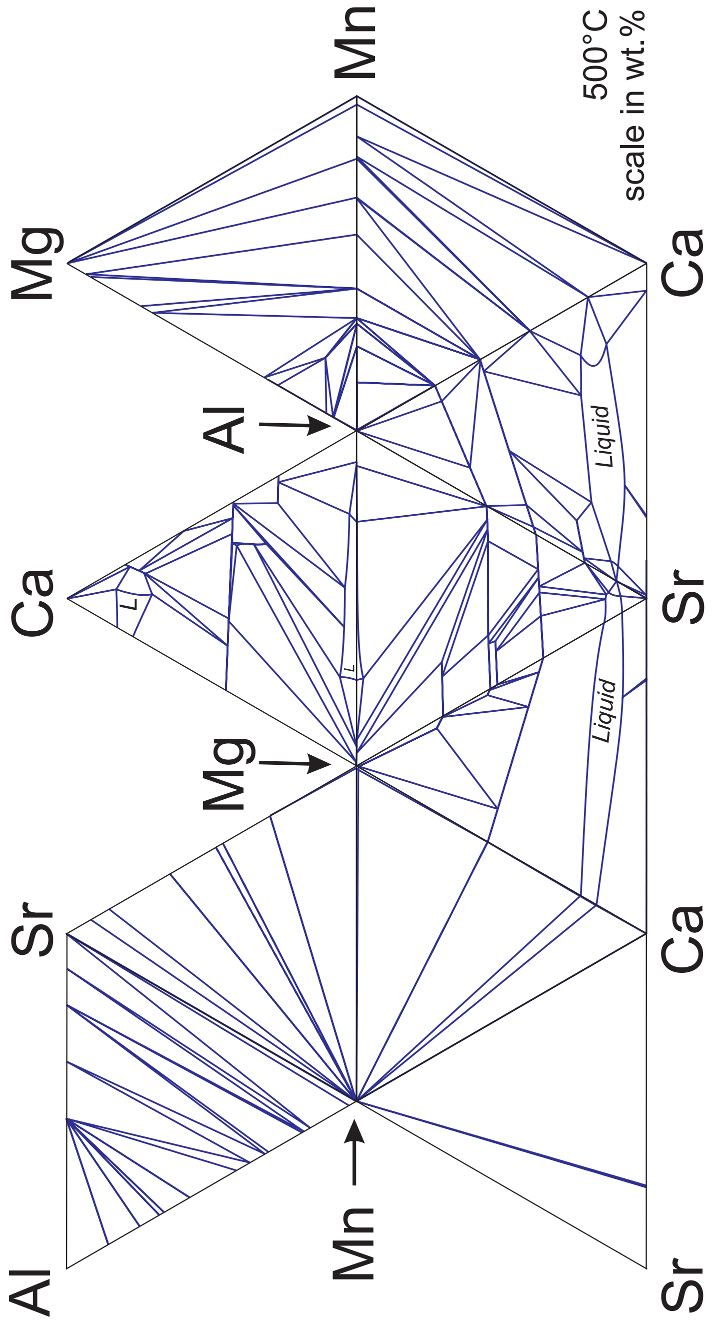

Fig. 4.7: Combination of the calculated ternary isothermal sections at 500 ° C from the subsystems of the Mg-Al-Ca-Sr-Mn quinary system.

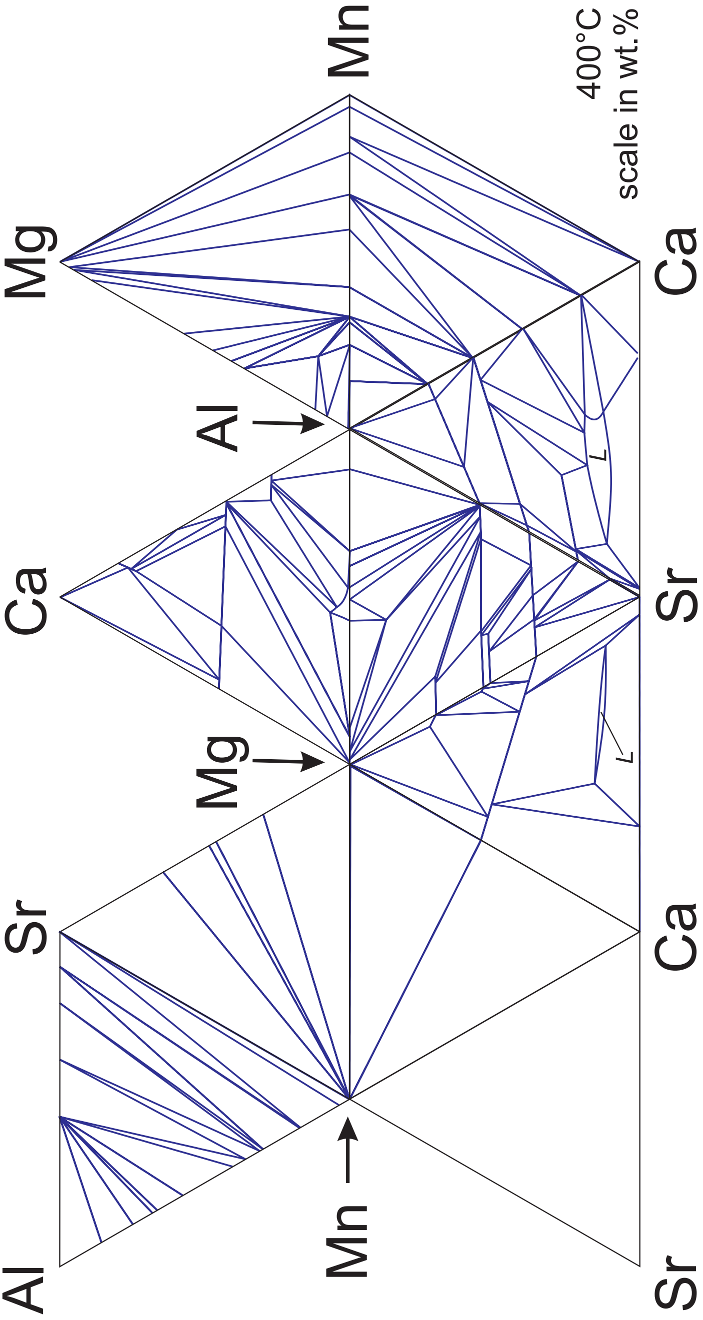

Fig. 4.8: Combination of the calculated ternary isothermal sections at 400 ° C from the subsystems of the Mg-Al-Ca-Sr-Mn quinary system.

4.3.2 Comparison between experimental data and thermodynamic calculations

The thermal signals obtained for the various five-component samples by DTA are compared with the calculated equilibrium solidification phase boundaries of each sample in Table 4.1 . It is obvious, that a number of experimental signals are missing compared to the calculation. The appearance is anyhow reasonable, which is demonstrated in the following.

The primary precipitation of the Al-Mn phases, especially of Al_8Mn_5, is usually not detected by DTA in Mg-alloys as discussed by Ohno et al. in [2006Ohn], because the evolved phase amount of these phases is too small. Also many other reactions in the calculated solidification paths produce only small additional phase amounts. This is well shown for sample MRI135 in Fig. 4.9 , comparing the results of the solidification under equilibrium conditions (Fig. 4.9(a)) to those of the solidification under Scheil conditions (Fig. 4.9(b)). Note that a logarithmic scale was selected to resolve the minority phase amounts.

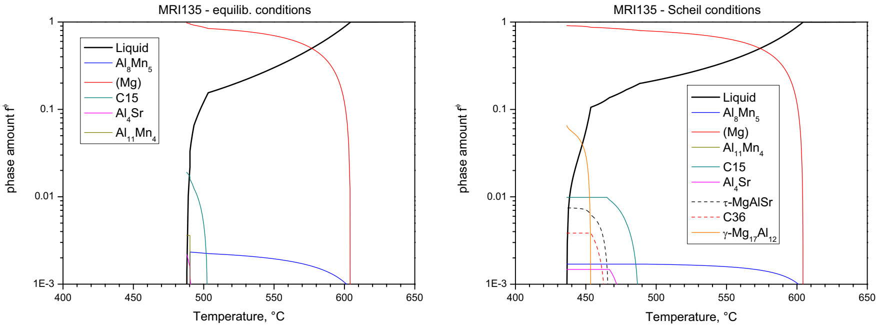

(a) Equilibrium conditions

(b) Scheil conditions

Fig. 4.9: Calculated solidification under different cooling conditions for the composition of sample MRI135.

The solidification of Mg alloys acts generally somewhere in between these two models as discussed in [2006Ohn]. We can see the γ-$Mg_{17}Al_{12}$ phase forming a substantial amount of nearly 7 % below 454 °C under Scheil conditions in contrast to the equilibrium solidification. This phase was in fact detected in small amounts with EDX.

It is possible to select a reasonable vertical phase diagram section representing both MRI samples, presented in Fig. 4.10 . Both the Mn and Sr content are fixed for the whole diagram range while Al and Ca are varied to meet the samples' composition. Mg was selected as balance. We can see that the thermal signals from DTA for both samples are represented by the calculation and correlate with the start of the precipitation of the two majority phases in each sample, (Mg) and C15 / C36. This is also in excellent agreement with the f^{ϕ}-calculation of Figs. 4.9(a) and 4.9(b). The primary phase Al_8Mn_5 is showing only trace amounts at the calculated start of the solidification, even below the cut off limit of $f^{\phi} = 0.001$ in these diagrams.

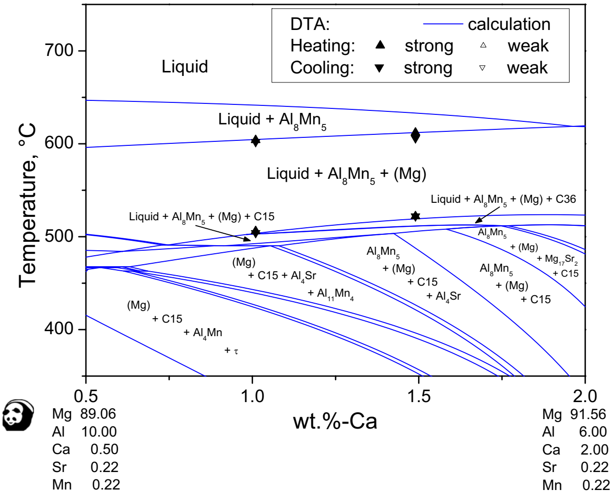

Fig. 4.10: Calculated vertical phase diagram section in the Mg-Al-Ca-Sr-Mn quinary system compared with experimental data from DTA for samples MRI135 and MRI230.

Fig. 4.11 shows the vertical phase diagram section constructed to meet the composition of both quinary key samples. The composition of this section is therefore running almost from the ternary Mg-Ca-Sr to the ternary Mg-Al-Mn. The first investigated synthetic alloy, MACSM#1, was selected to evaluate the key invariant reaction U20 at 490 ° C, the range of this reaction is highlighted in Fig. 4.11 with the red line. The predicted temperature of this reaction is exactly confirmed by this sample. In contrast sample MRI135 should also pass this reaction, but no signal was detected since the phase exchange of this reaction was too small in this sample. Remembering Fig. 2.6 on page 19 , the composition of sample MRI135 is within the area of the reaction but somewhere far from the center, while the composition of sample MACSM#1 is almost at the position ①, where the complete reaction occurs. This proof was only possible with a key sample composition far from the Mg-corner, selected with the algorithm presented in section 2.6 . The composition is therefore very unusual with less than 50 wt.% Mg but more than 30 wt.% Al and almost 16 wt.% Mn. As expected from the calculated equilibrium solidification (Fig. 4.12), substantial amounts of Al-Mn phases were detected in the microstructure (Fig. 4.3 on page 106). The primary phase in the experiment was $Al_{11}Mn_4$, followed

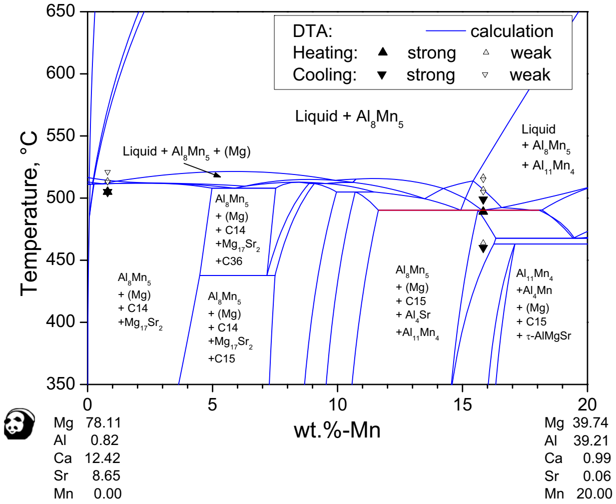

Fig. 4.11: Calculated vertical phase diagram section in the Mg-Al-Ca-Sr-Mn quinary system compared with experimental data from DTA for samples MACSM#1 and #2. The red line indicates the invariant reaction U20.

by Al_4Mn. $Al_{11}Mn_4$ was expected to form after the Al_8Mn_5 - this might indicate either some problem in the description of the Mg-Al-Mn phase equilibria or some kinetic barrier which shifted the phase sequence. It is also possible that solid transition reactions of these phases have happened. The small amounts of γ-$Mg_{17}Al_{12}$ detected in the microstructure start to form under Scheil conditions at 454 °C which is close to the temperature detected with DTA but not assigned in Table 4.1 .

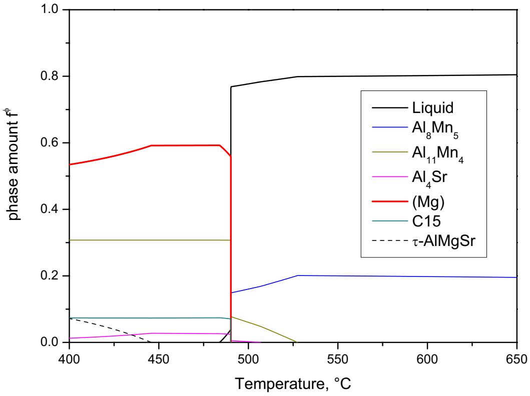

Fig. 4.12: Calculated solidification of sample MACSM#1 under equilibrium cooling conditions.

The microstructure of sample MACSM#2 (Fig. 4.4) is in reasonable agreement with the calculation. Al_8Mn_5 particles were found in the sample, they contain the increased Mn content (0.8 wt.%) compared to the MRI alloys. Several thermal signals were detected within a narrow temperature range, which made a proper separation almost impossible, even at 1 K/min heating/cooling rate. The calculated temperatures of the precipitation of $Mg_{17}Sr_2$ fit exactly the thermal signals. The following three calculated reactions appear very close to each other within a temperature interval of only 0.6 K. Although the final reaction during the solidification of this sample is not calculated as "invariant", the remaining 90% of the liquid phase are expected to solidify within a temperature interval of only 0.05 K, see Fig. 4.13 . These concentrated reactions can explain both the ultrafine microstructure and the very strong thermal signal. No invariant reaction is predicted by the calculation for this sample composition, due to the two different Mg-Al-Mn ternary datasets used for the key samples' selection and the later interpretation.

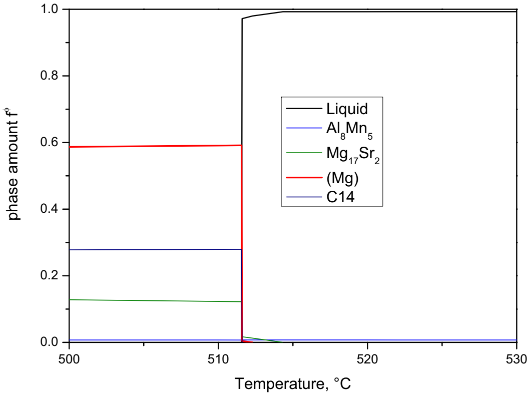

Fig. 4.13: Calculated solidification of sample MACSM#2 under equilibrium cooling conditions.

4.4 Conclusion

- The consistent thermodynamic dataset for the Mg-Al-Ca-Sr system presented in chapter 3 has been extended with the datasets for the binary Mn-X systems and the assessed description for the Mg-Al-Mn system.
- The calculations based on this extrapolation have reproduced the results of the experiments satisfyingly, even for the unusual sample with more than 15 wt.% Mn, which is a key sample defining the most crucial invariant reaction involving (Mg).
- The existence of quaternary and quinary phases was checked but none was found. The thesis, that a proper description of the ternary systems will give a reasonable database for the calculation of alloys of higher order, is confirmed for the Mg-Al-Ca-Sr-Mn system.

Chapter 5

Summary

The technological and ecological background of this work is the development of a tool for focused development of advanced magnesium alloys, which are relevant for weight savings in the automotive industry or other applications. The scientific aspect of the present work is the development of a consistent thermodynamic description for the quinary Mg-Al-Ca-Sr-Mn system. This alloy system is the backbone for understanding the phase equilibria and the solidification in the commercial AM, AX, AJ and AXJ magnesium alloy groups. This work will also help to understand the important grain refining application of AZ alloys with Ca and Sr.

Within the field of thermodynamic calculations it is widely accepted to perform calculations for higher order systems by an extrapolation on the basis of assessed binary and ternary subsystems. The quality of such multicomponent calculations is fundamentally based on the quality of these subsystems. Therefore, the goal of this work is to generate reliable thermodynamic descriptions of the pertinent ternaries and, furthermore, to validate the results of multicomponent calculations by selected key experiments. A quantitative selection criterion for such most important experimental conditions is proposed. The quality and reliability of such thermodynamic extrapolation calculations is thus validated on these real examples of quaternary and quinary alloy systems.

The emphasis of this work is on the phase equilibria of the Mg-Al-Ca-Sr system which is extended to the quinary Mg-Al-Ca-Sr-Mn system. The phase equilibria of the ternary subsystems in the quaternary Mg-Al-Ca-Sr system were investigated using the Calphad technique. Based on critical evaluations of experimental data in the literature, preliminary datasets were established as a basis for first calculations in the subsystems Mg-Al-Ca, Mg-Al-Sr, Mg-Ca-Sr and Mg-Al-Sr. Key experiments were selected on the basis of these calculations and performed using Differential Scanning Calorimetry (DSC) and Differential Thermal Analysis (DTA) as well as Scanning Electron Microscopy (SEM) and Electron Probe X-Ray Microanalysis (EPMA) to evaluate ternary solubilities of binary phases and to identify true ternary compounds. The results were used to optimize the thermodynamic parameters for each phase in the corresponding system.

It was shown that true ternary compounds exist only in the Mg-Al-Ca system (C36) and in the Mg-Al-Sr system (τ-MgAlSr). In contrast ternary (and by combination even quaternary) solubilities exist for most of the binary solid phases, sometimes in surprisingly large ranges. In order to reproduce these complex phase equilibria in the ternary systems, the thermodynamic parameters were adjusted to reproduce the experimental findings with the calculations. The extrapolation from the pertinent ternary subsystems to the quaternary Mg-Al-Ca-Sr system was validated with key experiments to assure the reliability of calculations with this dataset. The results (DTA, SEM/BSE and EDX) of the quaternary key samples, carefully selected on the basis of a newly developed algorithm, proved the high quality of this thermodynamic description. No true quaternary compound was identified in these experiments.

Finally, an extension was performed to comprise the impact of manganese, which is often present in commercial Mg alloys. The phase equilibria in the quinary system Mg-Al-Ca-Sr-Mn were checked with the same thorough procedures used for the quaternary system. For this extended extrapolation, the thermodynamic parameter set of the recently assessed ternary Mg-Al-Mn subsystem was included. Two key samples were selected based on the algorithm proposed in this work, in accord with the calculated invariant six-phase reactions. In addition, two commercial Mg alloys with a chemical composition situated in the Mg-Al-Ca-Sr-Mn system were investigated. The experimental results of these four samples are compared with the intricate multicomponent calculations and are well reproduced.

Bibliography

[1942Sch] E. Scheil: Bemerkungen zur Schichtkristallbildung; *Z. Metallkd* **34** (1942), 70

[1970Hil] M. Hillert and L.-I. Staffansson: Regular-Solution Model for Stochiometric Phases and Ionic Liquids; *Acta Chem. Scand.* **24** (1970), 3618-3626

[1980Hil] M. Hillert: Empirical methods of predicting and representing thermodynamic properties of ternary solution phases; *Calphad* **4** (1980), 1-12

[1980Mak] M.M. Makhmudov, A.V. Vakhobov, T.D. Dzhuraev, I.N. Ganiev: Combined Solubility of Components of a Magnesium-Aluminum- Strontium System in Aluminum- and Magnesium-Rich Regions; *Dokl. Akad. Nauk Tadzh. SSR*, **23(1)** (1980), 25-28

[1981Mak1] M.M. Makhmudov, A.V. Vakhobov, T.D. Dzhuraev: Liquidus Surface of Aluminum and Magnesium Phases of the Magnesium-Aluminum-Strontium Diagram; *Dokl. Akad. Nauk Tadzh. SSR,* **24(7)** (1981), 435-438

[1981Mak2] M.M. Makhmudov, O.J. Bodak, A.V. Vakhobov, T.D. Dzhurayev: Phase Equilibria in the Mg-Al-Sr System; *Izv. Akad. Nauk SSSR, Met.*, **(6)** (1981), 209-212

[1982Mak1] M.M. Makhmudov, A.V. Vakhobov, T.D. Dzhuraev: Examination of Quasi-binary Sections of the Mg-Al-Sr System; *Russ. Metall.*, **(1)** (1982), 122-124

[1982Mak2] M.M. Makhmudov, A.V. Vakhobov, I.N. Ganiev: Study of the Liquidus Surface of the Sr/SrMg (SrMg(2))/Sr- Al (SrAl(4)) System Using Simplex Experimental Planning; *Zavods. Lab.*, **48** (1982), 61-62

[1986And] J.O. Andersson, A. Fernandez Guillermet, M. Hillert, B. Jansson, B. Sundman: A Compound-Energy Model of Ordering in a Phase With Sites of Different Coordination Numbers; *Acta metall.* **34** 437-445 (1986)

[1989Hem] W. F. Hemminger und H. K. Cammenga: Binary Alloy Phase Diagrams, 2^{nd} edition; ASM International, Metals Park, Ohio (1990)

[1990Ell] M. Ellner: The structure of the high-temperature phase MnAl(h) and the displacive transformation from MnAl(h) into Mn_5Al_8; *Met Trans A* **21 (6)** (1990), 1669-1672

[1990Mas] T.B. Massalski, H. Okamoto, P.R. Subramanian, L. Kacprzak (Eds.): Methoden der Thermischen Analyse; Springer Verlag, Berlin (1989)

[1991Din] A.T. Dinsdale: SGTE data for pure elements; *Calphad* **15** (1991), 317-425

[1991Vil] P. Villars, L.D. Calvert: Pearson's Handbook of Crystallographic Data for Intermetallic Phases, 2^{nd} edition; ASM International, Metals Park, Ohio, USA (1991)

[1992Ger] Ch. Gerthsen, H.O. Kneser, H. Vogel: Physik: ein Lehrbuch zum Gebrauch neben Vorlesungen, 16. Auflage; Springer-Verlag, Berlin, Heidelberg, Germany ISBN 3-540-51196-2 (1992)

[1994Ang] C. Anglezio, I. Ansara: Contribution to the experimental and thermodynamic assessment of the Al-Ca-Fe-Si system—I. Al-Ca-Fe, Al-Ca-Si, Al-Fe-Si and Ca-Fe-Si systems; *Calphad* **18** (1994), 273-309

[1994Cha] P. Chartrand and A.D. Pelton: Critical Evaluation and Optimization the Thermodynamic Properties and Phase Diagrams of the Al-Mg, Al-Sr, Mg-Sr, and Al-Mg-Sr Systems; *J. Phase Equilibria* **15 (6)** (1994), 591-605

[1995Aga] R. Agarwal, J. Lee, H. Lukas and F. Sommer: Calorimetric Measurements and Thermodynamic Optimization of the Ca-Mg System; *Z. Metallkd.* **86 (2)** 103-108 (1995)

[1995Pre] F. Press and R. Siever: Allgemeine Geologie; Spektrum Akademischer Verlag, Heidelberg, Germany (1995)

[1996Hoe] G.W.H. Höhne, W. Hemminger and H.-J. Flammersheim: Differential scanning calorimetry: an introduction for practitioners; Springer-Verlag, Berlin, Heidelberg, Germany (1996)

[1997Ans] I. Ansara, T.G. Chart, A. Fernandez Guillermet, F.H. Hayes, U.R. Kattner, D.G. Pettifor, N. Saunders, K. Zeng: Thermodynamic Modelling of Solutions and Alloys; *Calphad* **21** (1997), 171-218

[1997Kat] U. Kattner: Thermodynamic Modeling of Multicomponent Phase Equilibria; *JOM* **49** (1997), 14-19

[1997Kre] G. Kreiner and H. F. Franzen: The crystal structure of λ-Al_4Mn; *J. Alloys Compounds* **261** (1997), 83-104

[1997Su] H.-L. Su, M. Harmelin, P. Donnadieu, C. Baetzner, H.J. Seifert, H.L. Lukas, G. Effenberg and F. Aldinger: Experimental Investigation of the Mg-Al Phase Diagram from 47-63 at.% Al; *J. Alloys Compounds* **247** (1997), 57-65

[1998Hua] B. Huang and J.D. Corbett: Two New Binary Calcium-Aluminum Compounds: $Ca_{13}Al_{14}$, with a Novel Two-Dimensional Aluminum Network, and Ca_8Al_3, an Fe_3Al-Type Analogue; *Inorg. Chem.* **37 (22)** (1998) 5827-5833

[1998Lia] P. Liang, T. Tarfa, J.A. Robinson, S. Wagner, P. Ochin, M.G. Harmelin, HJ. Seifert, HL. Lukas, F. Aldinger: Experimental investigation and thermodynamic calculation of the Al-Mg-Zn system; *Thermochimica Acta* **314 (1-2)** (1998), 87-110

[2001Che] S.-L. Chen, S. Daniel, F. Zhang, Y. A. Chang, W. A. Oates, R. Schmid-Fetzer: On the Calculation of Multicomponent Stable Phase Diagrams; *J. Phase Equilibria* **22** (2001), 373-378

[2001Hil] M. Hillert: The compound energy formalism; *J. Alloys Compounds* **320** (2001), 161-176

[2001Kev1] D. Kevorkov and R. Schmid-Fetzer: The Al-Ca system, Part 1: Experimental Investigation of Phase Equilibria and Crystal Structures; *Z.Metallkde.* **92** (2001), 946-952

[2001Kev2] D. Kevorkov, R. Schmid-Fetzer, A. Pisch, F. Hodaj, C. Colinet: The Al-Ca system, Part 2: Calorimetric measurements and Thermodynamic Assessment; *Z.Metallkde.* **92** (2001), 953-958

[2001Sch] R. Schmid-Fetzer, J. Gröbner: Focused Development of Magnesium Alloys using the Calphad Approach; *Adv. Eng. Mater.* **3** (2001), 947-961

[2001Zha] Q.A. Zhang, H. Enoki and E. Akiba: Phase relations and hydrogenation behavior of $Sr_{1-x}Ca_xAl_2$ ($0\leq x \leq 1$); *J. Alloys Compounds* **322** (2001), 257-264

[2002Che] S.-L. Chen, S. Daniel, F. Zhang, Y. A. Chang, X.-Y. Yan, F.-Y. Xie, R. Schmid-Fetzer, W. A. Oates: The Pandat Software Package and its Applications; *Calphad* **26** (2002), 175-188

[2003Ame] S. Amerioun, S.I. Simak, U. Häussermann: Laves-Phase Structural Changes in the System $CaAl_{2-x}Mg_x$; *Inorg. Chem.* **42 (5)** (2003), 1467 -1474

[2003Bar] E. Baril, P. Labelle, M.O. Pekguleryuz: Elevated Temperature Mg-Al-Sr: Creep Resistance, Mechanical Properties, and Microstructure; *JOM* **55** (2003), 34-39

[2003Gro] J. Gröbner, D. Kevorkov, I. Chumak, R. Schmid-Fetzer: Experimental Investigation and Thermodynamic Calculation of Ternary Al-Ca-Mg Phase Equilibria; *Z. Metallkde.* **94** (2003), 976-982

[2003Ozt] L. Ozturk, Y. Zhong, A.A. Luo, Z.-K. Liu: Creep Resistant Mg-Al-Ca Alloys: Computational Thermodynamics and Experimetnal Investigation; *JOM* **55 (11)** (2003), 40-44

[2003Pek] M.O. Pekguleryuz, A.A. Kaya: Creep Resistant Magnesium Alloys for Powertrain Applications; *Adv. Eng. Materials* **5 (12)** (2003), 866-878

[2003Tka] V.G. Tkachenko, V.G. Khoruzhaya, K.A. Meleshevich, M.V. Karpets, V.V. Frizel: Phase equilibria in the Mg-Al-Ca system (region 50-100 mass% Mg); *Powder Metallurgy and Metal Ceramics* **42** (2003), 268-273

[2003Zho] Y. Zhong, K. Ozturk and Z-K. Liu: Thermodynamic Modeling of the Ca-Sr-Zn Ternary System; *J. Phase Equilibria*, **24** (2003), 340-346

[2004Luo] A.A. Luo: Recent magnesium alloy development for elevated temperature applications; *International Materials Reviews* **49** (2004), 13-30

[2004Suz] A. Suzuki, N.D. Saddock, J.W. Jones, T.M. Pollock: Structure and transition of eutectic $(Mg,Al)_2Ca$ Laves phase in a die-cast Mg-Al-Ca base alloy; *Scripta Materialia* **51 (10)** (2004), 1005-1010

[2004Wan] X. Wang, M.A. Parvez, E. Essadiqi, M. Medraj: A differential scanning calorimeter study of Mg-Al-Ca ternary system; *CSME 2004 Forum* (2004), 819-928

[2004Zho] Y. Zhong, C. Wolverton, Y. Austin Chang, Z.-K. Liu: A combined CALPHAD/first-principles remodeling of the thermodynamics of Al–Sr: unsuspected ground state energies by "rounding up the (un)usual suspects"; *Acta Materialia* **52** (2004), 2739-2754

[2005Cze] F. Czerwinski, A. Zielinska-Lipiec: The microstructure evolution during semisolid molding of a creep-resistant Mg–5Al–2Sr alloy; *Acta Materialia* **53** (2005), 3433-3444

[2005Gro] J. Gröbner, D. Mirkovic, M. Ohno and R. Schmid-Fetzer: Experimental investigation and thermodynamic calculation of binary Mg-Mn phase equilibria. *J. Phase Equilibria & Diffusion* **26** (2005), 234-239

[2005Isl] F. Islam, M. Medraj: Thermodynamic Modelling of the Mg-Al-Ca system; *Canadian Metallurgical Quarterly* **44** (2005), 523-536

[2005Ohn] M. Ohno and R. Schmid-Fetzer: Thermodynamic assessment of Mg-Al-Mn phase equilibria, focusing Mg-rich alloys; *Z. Metallkde.* **96** (2005), 857-869

[2005Par] M.A. Parvez, M. Medraj, E. Essadiqi, G. Dénès: Experimental study of the ternary magnesium–aluminium–strontium system; *J. Alloys Compounds* **402** (2005), 170–185

[2005Suz] A. Suzuki, ND. Saddock, JW. Jones, TM. Pollock: Solidification paths and eutectic intermetallic phases in Mg-Al-Ca ternary alloys; *Acta Materialia* **53 (9)** (2005), 2823-2834

[2005Zha] Q.A. Zhang, W.M. Yang, E. Akiba: Synthesis and crystal structure of a new ternary compound Ca_4Al_3Mg; *J. Alloys Comp.* **398** (2005), 123-126

[2005Zho] Y. Zhong, A.A. Luo, J.O. Sofo, Z.-K. Liu: First-Principles Investigation of Laves Phases in Mg-Al-Ca System; *Materials Science Forum* **488-489** (2005), 169-176

[2006Boe] W.J. Boettinger, U.R. Kattner, K.-W. Moon, J.H. Perepezko: DTA and Heat-flux DSC Measurements of Alloy Melting and Freezing; NIST, Washington, USA (2006)

[2006Cao] H. Cao, J. Zhu, C. Zhang, K. Wu, N.D. Saddock, J.W. Jones, T.M. Pollock, R. Schmid-Fetzer and Y. A. Chang: Experimental Investigation and Thermodynamic modeling of the Mg-Al rich region of Mg-Al-Sr System; *Z. Metallkunde* **97** (2006), 422-428

[2006Mir] D. Mirkovic and R. Schmid-Fetzer: Solidification curves for commercial Mg alloys; *Z.Metallkde.* **97** (2006), 119-129

[2006Ohn] M. Ohno, D. Mirkovic and R. Schmid-Fetzer: Liquidus and Solidus Temperatures of Mg-rich Mg-Al-Mn-Zn Alloys; *Acta Materialia* **54** (2006), 3883-3891

[2006Rok] L. L. Rokhlin, N. I. Nikitina, V. A. Volchenkova: Magnesium-Rich Mg–Al_2Ca Alloys; *Russian Metallurgy* **(2)** (2006), 185-188

[2006Suz] A. Suzuki, N.D. Saddock, J.W. Jones, T.M. Pollock: Phase Equilibria in the Mg-Al-Ca Ternary System at 773 and 673 K; *Metall. Mater. Trans.* **37A (3)** (2006), 975-983

[2006Zho] Y. Zhong, J.O. Sofo, A.A. Luo, and Z.-K. Liu: Thermodynamics modeling of the Mg–Sr and Ca–Mg–Sr systems, *J. Alloys Compounds* **421** (2006), 172-178

[2006Zho3] Yu Zhong, J. Liu, R.A. Witt, Y. Sohn, Z.K. Liu: Al_2(Mg,Ca) phases in Mg–Al–Ca ternary system: First-principles prediction and experimental identification; *Scripta Materialia* **55** (2006), 573-576

[2007Alj] M. Aljarrah, M. Medraj, X. Wang, E. Essadiqi, A. Muntasar, G. Dénès: Experimental investigation of the Mg Al Ca system; *Journal of Alloys Compd.* **36** (2007), 131-141

[2007Cao] H-B. Cao, C. Zhang, J. Zhu, G-P. Cao, S. Kou, R. Schmid-Fetzer, Y.A. Chang: Experiments Coupled with Modeling to Establish the Mg-rich Phase Equilibria of Mg-Al-Ca; *Acta Materialia*, in press (2007)

[2007Du] Y. Du, J. Wang, J. Zhao, J.C. Schuster, F. Weitzer, R. Schmid-Fetzer, M. Ohno, H. Xu, Z.-K. Liu, S. Shang, W. Zhang: Reassessment of the Al–Mn system and a thermodynamic description of the Al–Mg–Mn system; *Int. J. Mat. Res.* **98 (9)** (2007), 855-871

[2007Luk] H.L. Lukas, S.G.Friers, B. Sundman: Computational Thermodynamics: The Calphad Method; Cambridge University Press, Cambridge, United Kingdom (2007)

[2007Koz] A. Kozlov, M. Ohno, R. Arroyave, Z.K. Liu and R. Schmid-Fetzer: Phase Equilibria, Thermodynamics and Solidification Microstructures of Mg-Sn-Ca Alloys - Part 1. Experimental investigation and thermodynamic modeling of the ternary Mg–Sn–Ca system; *Intermetallics*, accepted (2007)

[2007Sch] R. Schmid-Fetzer, D. Andersson, P.Y. Chevalier, L. Eleno, O. Fabrichnaya, U.R. Kattner, B. Sundman, C. Wang, A. Watson, L. Zabdyr and M. Zinkevich: Assessment techniques, database design and software facilities for thermodynamics and diffusion; *Calphad* **31 (1)** (2007), 38-52

[2007Suz] A. Suzuki, ND. Saddock, L. Riester, E. Lara-Curzio, JW. Jones, TM. Pollock: Effect of Sr Additions on the Microstructure and Strength of a Mg-Al-Ca Ternary Alloy; *Met Trans A* **38 (2)** (2007), 420-427

[2008Alj1] M. Aljarrah and M. Medraj: Thermodynamic modelling of the Mg–Ca, Mg–Sr, Ca–Sr and Mg–Ca–Sr systems using the modified quasichemical model; Calphad (accepted)(2008) doi:10.1016/j.calphad.2007.09.001

[2008Alj2] M. Aljarrah and M. Medraj: Thermodynamic assessment of the phase equilibria in the Al–Ca–Sr system using the modified quasichemical model; Journal Chem. Therm (accepted)(2008) doi:10.1016/j.jct.2007.10.003

[2008Cao] H-B. Cao, C. Zhang, J. Zhu, G-P. Cao, S. Kou, R. Schmid-Fetzer, Y.A. Chang: A computational/directional solidification method to establish saddle point on the Mg-Al-Ca liquidus; *Scripta Materialia*, in press (2008)

[IMA] International Magnesium Association; Wauconda, IL, USA http://www.intlmag.org/

[PowderCell] W. Kraus and G. Nolze: PowderCell for Windows version 2.4; Federal Institute for Materials Research and Testing, Berlin, Germany, http://www.bam.de/service/publikationen/powder_cell.htm

Appendix A

Additional tables

Table A.1: All solid phases of the Mg-Al-Ca-Sr-Mn system.

Phase/ Temperature range, ° C	**Pearson symbol/ Space group/ Prototype**	**Lattice parameters (pm)**	**Model/ Comments/ References**
(Al) < 660	cF4 $Fm\bar{3}m$ Cu	$a = 404.96$	[1990Mas]
(Mg) < 650	hP2 $P6_3/mmc$ Mg	$a = 320.94$ $c = 521.07$	max 12.7 wt.% Al [this work] [1990Mas]
(δMn) 1246-1138	cI2 $Im\bar{3}m$ W	a = 308.1	[1991Vil]
(γMn) 1138-1087	cF4 $Fm\bar{3}m$ Cu	a = 386.2	[1991Vil]
(βMn) (707) − 1087	cP20 $P4_132$ βMn	a = 631.5	[1991Vil]
(αMn) < 707	cI58 $I\bar{4}3m$ αMn	a = 891.39	[1991Vil]
α(Ca,Sr)	cF4 $Fm\bar{3}m$ Cu		complete solubility
αCa < 443		a = 560.1	pure αCa [1991Vil]
αSr < 547		a = 608.4	pure αSr at 25 ° C [1990Mas]
β(Ca,Sr)	cF4 $Fm\bar{3}m$ Cu		complete solubility
βCa 443 − 842		a = 448.9	pure βCa [1991Vil]
βSr 547 − 776		a = 608.4	pure βSr at 614 ° C [1990Mas]
$Al_{12}Mn$ < 512	cI26 $Im3$ $Al_{12}W$	a = 750.7	[1991Vil]

Continued on next page

Table A.1 – continued from previous page

Phase/ Temperature range, °C	Pearson symbol/ Space group/ Prototype	Lattice parameters (pm)	Model/ Comments/ References
Al_6Mn < 703	oC28 *Cmcm* Al_6Mn	a = 754.5(2) b = 649.0(3) c = 868.1(2)	[1991Vil]
$\lambda-Al_4Mn$ < 721	hP586 $P6_3/m$	a = 2838.2 c = 1238.9	[1997Kre]
$\mu-Al_4Mn$ < 922	hP574 $P6_3/mmc$ Al_4Mn	a = 1998(1) c = 2467.3(3)	[1997Kre]
$HTAl_{11}Mn_4$ (Al_3Mn) 1002-905	oP156 $Pn2_1a$ Al_3Mn	a = 1485.4 b = 1242.2 c = 1254.0	[1997Kre]
$LTAl_{11}Mn_4$ ≤ 914	aP15 $P\bar{1}$ $Al_{11}Mn_4$	a = 509.5(4) b = 887.9(8) c = 505.1(4) $\alpha = 89.35^o$ $\beta = 1004.47^o$ $\gamma = 105.08^o$	[1991Vil]
Al_8Mn_5 < 1046	hR26 R3m Al_8Cr_5	a = 1266.7(3) c = 794.2(2) a = 1259.8(2) c = 792.1(2)	at 38.5 at.% Mn [1990Ell] at 46.5 at.% Mn [1990Ell]
$\gamma-AlMn$ 1185-849	cI2 $Im\bar{3}m$ W	a = 306.3(3)	[1990Ell]
$\varepsilon-AlMn$ 1281-823	hP2 $P6_3/mmc$ Mg	a = 269.8 c = 437.0	[1991Vil]
$\tau-Al_{18}Mg_3Mn_2$	cF184 $Fd\bar{3}m$ $Al_{18}Mg_3Cr_2$	a=1452.9	[1991Vil]
$\pi-Al_4Mn$	oC152 *Cmcm*	a = 770 b = 1360 c = 1240	metastable [1997Kre]
i-AlMn	$Pm\overline{35}$ icosahedral	a = 650.5	metastable [1997Kre] formed from the metastable liquid by a first order transition
T-AlMn	$P10_2/mmc$ decagonal	$a_1 = 391.2$ $a_2 = 1240$	metastable [1997Kre] fromed in melt-spun ribbons
$Al_{10}Mn_3$	hP26 $P6_3/mmc$ Al_5Co_2	a = 754.3 c = 789.8	metastable [1991Vil] formed from the liquid during cooling and probably also during decomposiont of super-saturated (Al)
$\tau-AlMn$	tP2 $P4/mmm$ AuCu	a = 277 c = 354	metastable [1997Kre] formed from the high-temperature phase ε-AlMn region during cooling at rates of about $10^{\circ}Cs^{-1}$ or retained ε-AlMn at low temperature
$Mg_{17}Sr_2$ < 605	hP38 $P6_3/mmc$ Th_2Ni_{17}	a = 1053.0 to 1031.0 c = 1040.8 to 1019.0	$(Al,\mathbf{Mg})_{17}(Ca,\mathbf{Sr})_2$ max 13.8 wt.% Al [this work] max 1.8 wt.% Ca [this work] [1981Mak2]

Continued on next page

Table A.1 – continued from previous page

Phase/ Temperature range, °C	**Pearson symbol/ Space group/ Prototype**	**Lattice parameters (pm)**	**Model/ Comments/ References**
$Mg_{38}Sr_9$ < 601	hP94 $P6_3/mmc$ Sr_9Mg_{38}	a = 1050.0 c = 2825.1	$(\mathrm{Al},\mathbf{Mg})_{38}(\mathrm{Ca},\mathbf{Sr})_9$ max 18.0 wt.% Al [this work] max 1.5 wt.% Ca [this work] [1994Cha]
$Mg_{23}Sr_6$ < 614	cF116 $Fm\bar{3}m$ Th_6Mn_{23}	a = 1503 to 1463.5	$(\mathrm{Al},\mathbf{Mg})_{23}(\mathrm{Ca},\mathbf{Sr})_6$ max 15.9 wt.% Al [this work] [1981Mak2]
Al_2Sr < 922	oI12 $Imma$ $CeCu_2$	a = 480.2 to 480.9 b = 791.2 to 794.3 c = 796.5 to 804.0	$(\mathbf{Al},\mathrm{Mg})_2(\mathrm{Ca},\mathbf{Sr})$ max 17.9 wt.% Mg [this work] max 3.2 wt.% Ca [this work] [1981Mak2]
Al_7Sr_8 < 668	cP64 $P2_13$ Sr_8Al_7	a = 1275.3	max 11.5 wt.% Ca [this work] [1994Cha]
Al_3Sr_8 342-605	aP22 $P\bar{1}$ Ca_8In_3		[2004Zho]
β, Al_3Mg_2 < 451	cF1832 $Fd\bar{3}m$ Mg_2Al3	a = 2823.9	[1997Su]
ε, $Al_{30}Mg_{23}$ 250-410	hR53 $R\bar{3}$ $Mg_{23}Al_{30}$	a = 1282.54 c = 2174.78	[1991Vil]
γ-$Mg_{17}Al_{12}$ < 464	cI58 $I\bar{4}3m$ αMn	a = 1054.38	$(\mathrm{Mg})_{10}(\mathrm{Al},\mathrm{Ca},\mathbf{Mg})_{24}(\mathbf{Al},\mathrm{Mg})_{24}$ max 6 at.% Ca at 400 °C [2005Suz] max 4.4 at.% Ca [2006Suz] max 4.3 at.% Ca [this work] [1991Vil]
C15-Al_2Ca < 1089	cF24 $P6_3/mmc$ $MgCu_2$	a = 803.8 to 807.6	$(\mathbf{Al},\mathrm{Mg})_2(\mathbf{Ca},\mathrm{Sr})$ max 4.8 wt.% Mg [this work] max 51.8 wt.% Sr [2001Zha] max 49.2 wt.% Sr [this work] [1991Vil, 2003Gro]
Al_3Ca_8 < 579	aP22 $P\bar{1}$ Ca_8In_3	a = 0.94950(8) b = 0.95922(8) c = 0.96704(7) α = 99.057(6) ° β = 101.152(7) ° γ = 119.613(8) °	$(\mathrm{Al})_3(\mathbf{Ca},\mathrm{Mg})_8$ max 13.8 wt.% Al [this work] [2001Kev1]
AlCa < 633	mC54	a = 1555.1 b = 987.3 c = 972.6±2 β = 108.09±2 °	(Al)(Ca) $Ca_{13}Al_{14}$ [1998Hua]
Al_4Ca ≤ 700	tI10 $I4/mmm$ $BaAl_4$	a = 435.3 c = 1107	$(\mathbf{Al},\mathrm{Mg})_4(\mathbf{Ca},\mathrm{Sr})$ max 8.4 wt.% Mg [this work] max 6.1 wt.% Sr [this work] [1991Vil]

Continued on next page

Table A.1 – continued from previous page

Phase/ Temperature range, °C	Pearson symbol/ Space group/ Prototype	Lattice parameters (pm)	Model/ Comments/ References
Al_4Sr	tI10		$(\mathbf{Al},Mg)_4(Ca,\mathbf{Sr})$
< 1021	$I4/mmm$		max 9.8 wt.% Mg [this work]
	$BaAl_4$		max 2.9 wt.% Ca [this work]
		a = 446.3 to 448.5	[1981Mak2]
		c = 1107.0 to 1131.0	
C14	hP12		$(Al,\mathbf{Mg})_2(Ca,Sr)$
	$P6_3/mmc$		complete solubity Ca-Sr
	$MgZn_2$		Mg_2Ca dissolves max 22.2 wt.% Al [this work]
			Mg_2Sr dissolves max 12.9 wt.% Al [this work]
Mg_2Ca		a = 622.5	pure Mg_2Ca [1991Vil]
< 713		c = 1018	
Mg_2Sr		a = 647.5 to 635.2	pure Mg_2Sr [1981Mak2]
< 676		c = 1043.0 to 1034.5	
C36	hP24		$(Al)_{36}(Al,\mathbf{Mg})_{14}(\mathbf{Ca},Mg)_{25}$
401-833	$P6_3/mmc$		
	Mg_2Ni		
		a = 584	as cast [2004Suz]
		c = 1979	
		a = 596	after 100 days at 400 °C [2004Suz]
		c = 1897	
τ, $Al_{38}Mg_{58}Sr_4$			$Al_{38}Mg_{58}Sr_4$
< 477	Not certain		[this work]

List of symbols

a	Activity
c_p	Specific heat capacity
E	Eutectic reaction
f^{ϕ}	Phase fraction of phase ϕ
Δf	Phase fraction increment
G	Gibbs energy
H	Enthalpy
i	Element
L	Interaction parameter
P	Peritectic reaction
ϕ	Phase
R	Ideal gas constant ($8.314472\ \frac{\mathrm{J}}{\mathrm{mol \cdot K}}$)
S	Entropy
T	Temperature
U	Transition-type reaction
x_i	Atomic fraction
y_i	Site fraction

List of abbreviations

ASTM	American Society for Testing and Materials
BSE	Back scattered electrons
CALPHAD	Calculation of phase diagrams
CEF	Compound energy formalism
DSC	Differential scanning calorimetry
DTA	Differential thermal analysis
EDX	Energy dispersive X-ray spectroscopy
EPMA	Electron probe (X-ray) microanalysis
LOM	Light optical microscopy
MQM	Modified quasichemical model
SAD	Small angle diffraction
SEM	Scanning electron microscopy
SER	Stable element reference
TA	Thermal analysis
TEM	Transmission electron microscopy
WDX	Wavelength dispersive X-ray spectroscopy
XRD	X-ray diffraction

List of Figures

List of Tables

Curriculum vitae

Personal data

Name: Andreas Janz
Date of birth: February 28th 1978
Place of birth: Clausthal-Zellerfeld
Nationality: german
Marital status: unmarried, no children

Current position

since 2003-11-01	Research assistant, Institute of Metallurgy, Clausthal University of Technology

Educational career

10/1998 - 10/2003	Study of ‘Metallurgy’ Clausthal University of Technology Degree: Diplom-Ingenieur
1997 - 1998	*Military service*
1990 - 1997	Gymnasium Achim, final degree: Abitur
1988 - 1990	Orientierungsstufe Oyten
1986 - 1988	Grundschule Bassen
1984 - 1986	Grundschule Budberg